

Journal Pre-proof

How many subductions in the Variscan orogeny? Insights from numerical models

Regorda Alessandro, Jean-Marc Lardeaux, Manuel Roda, Anna Maria Marotta, Maria Iole Spalla



PII: S1674-9871(19)30200-2

DOI: <https://doi.org/10.1016/j.gsf.2019.10.005>

Reference: GSF 900

To appear in: *Geoscience Frontiers*

Received Date: 24 January 2019

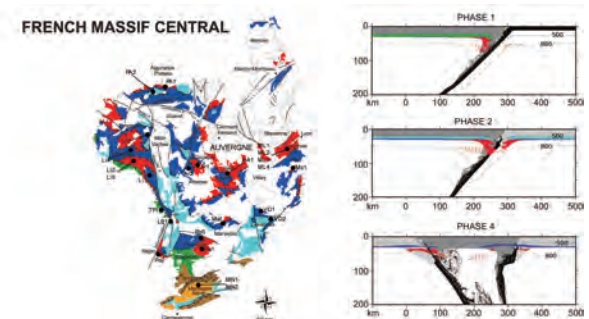
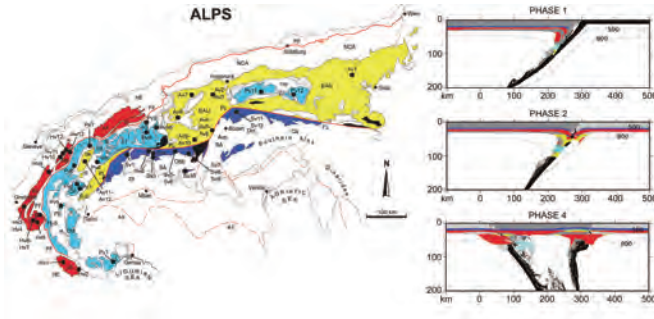
Revised Date: 26 August 2019

Accepted Date: 8 October 2019

Please cite this article as: Alessandro, R., Lardeaux, J.-M., Roda, M., Marotta, A.M., Spalla, M.I., How many subductions in the Variscan orogeny? Insights from numerical models, *Geoscience Frontiers*, <https://doi.org/10.1016/j.gsf.2019.10.005>.

This is a PDF file of an article that has undergone enhancements after acceptance, such as the addition of a cover page and metadata, and formatting for readability, but it is not yet the definitive version of record. This version will undergo additional copyediting, typesetting and review before it is published in its final form, but we are providing this version to give early visibility of the article. Please note that, during the production process, errors may be discovered which could affect the content, and all legal disclaimers that apply to the journal pertain.

© 2019 China University of Geosciences (Beijing) and Peking University. Production and hosting by Elsevier B.V. All rights reserved.



Journal Pre-proof

1 **How many subductions in the Variscan orogeny? Insights from** 2 **numerical models**

3

4 Regorda Alessandro^{a,*}, Jean-Marc Lardeaux^b, Manuel Roda^a, Anna Maria Marotta^a, Maria Iole
5 Spalla^a

6

7 ^a *Università degli Studi di Milano, Dipartimento di Scienze della Terra 'A. Desio', via Mangiagalli*
8 *34, I-20133 Milano, Italy*

9

10 ^b *Université Nice Sophia-Antipolis, UMR Geoazur, 250 Rue A. Einstein, Sophia-Antipolis, 06560,*
11 *Valbonne, France*

12

13 * Corresponding author. E-mail address: alessandro.regorda@unimi.it

14

15 **Abstract**

16

17 We developed a 2D numerical model to simulate the evolution of two superposed ocean-continent-
18 ocean subduction cycles with opposite vergence, both followed by continental collision, aiming to
19 better understand the evolution of the Variscan belt. Three models with different velocities of the
20 first oceanic subduction have been implemented. Striking differences in the thermo-mechanical
21 evolution between the first subduction, which activates in an unperturbed system, and the second
22 subduction, characterised by an opposite vergence, have been enlighten, in particular regarding the
23 temperature in the mantle wedge and in the interior of the slab. Pressure and temperature (P-T)
24 conditions predicted by one cycle and two cycles models have been compared with natural P-T
25 estimates of the Variscan metamorphism from the Alps and from the French Massif Central (FMC).
26 The comparative analysis supports that a slow and hot subduction well reproduces the P-T

27 conditions compatible with data from the FMC, while P-T conditions compatible with data of
28 Variscan metamorphism from the Alps can be reproduced by either a cold or hot oceanic
29 subduction models. Analysing the agreement of both double and single subduction models with
30 natural P-T estimates, we observed that polycyclic models better describe the evolution of the
31 Variscan orogeny.

32

33 **Key words:** Alps; Double subduction; French Massif Central; Numerical modelling; Variscan
34 orogeny

35

36 **1 Introduction**

37

38 The Variscan belt is the result of the Pangea accretion that most marks the European continental
39 lithosphere from Iberian Peninsula to Poland (von Raumer et al., 2003; Lardeaux et al., 2014) and,
40 as in all collisional belts, the debate on the number of oceans and subduction systems that have been
41 active during the orogen formation is open (Pin, 1990; Faure et al., 1997; Franke et al., 2017). It is
42 part of a 1000 km broad and 8000 km long Paleozoic mountain system (Matte, 2001) and results
43 from the successive collision of Gondwana and Gondwana-derived microcontinents, such as
44 Avalonia, Mid-German Crystalline Rise (MGCR) and Armorica, against Laurussia during
45 Devonian–Carboniferous times (e.g. Giorgis et al., 1999; Matte, 2001; von Raumer et al., 2003;
46 Marotta and Spalla, 2007; Compagnoni and Ferrando, 2010; Cocks and Torsvik, 2011; Edel et al.,
47 2013; Lardeaux et al., 2014). The final convergence between the supercontinents of Laurussia, to
48 the north, and Gondwana, to the south, was associated with an intensive deformation of the
49 assembled Avalonia and Armorican terranes (Edel et al., 2013, 2018).

50 Avalonia comprises the northern foreland of the Variscan belt and is geologically well defined
51 because it lies between major sutures: the Iapetus and the Tornquist Caledonian sutures to the north
52 separating Avalonia from North America and from Baltica, respectively, and the Rheic Variscan

53 suture to the south (Fig. 1). Avalonia drifted northward independently from Armorica during the
54 Early Palaeozoic (Trench and Torsvik, 1991; Cocks and Torsvik, 2011), detaching from Gondwana
55 during Ordovician times originating the Rheic Ocean, while the Iapetus closed southward and then
56 northward by subduction beneath the Taconic arc of Newfoundland (Pickering, 1989). Armorica is
57 not defined precisely on the basis of palaeomagnetic data, but it has been interpreted as a small
58 continental plate between the northern Rheic suture and the southern Galicia-southern Brittany
59 suture (Eo-Variscan suture, e.g. Faure et al., 2005; Fig. 1).

60 Two scenarios concerning the geodynamic evolution of the Variscan orogeny have been proposed:

61 (1) Monocyclic scenario: for some authors (e.g. Torsvik, 1998) Armorica remained more or
62 less closed to Gondwana during its northward drift, from Ordovician to Devonian times, in
63 agreement with the lack of biostratigraphic and paleomagnetic data that suggest a short-
64 lived narrow oceanic domain, smaller than 500–1000 km (Matte, 2001; Faure et al., 2009;
65 Lardeaux, 2014a). This type of geodynamic reconstruction assumes a single long-lasting
66 south-dipping subduction of a large oceanic domain, as proposed for the Bohemian Massif
67 (e.g. Schulmann et al., 2009, 2014; Lardeaux et al., 2014);

68 (2) Polycyclic scenario: this geodynamic scenario envisages two main oceanic basins
69 opened by the successive northward drifting of two Armorican microcontinent (Pin, 1990;
70 Faure et al., 1997; Franke et al., 2017) and closed by opposite subductions (Lardeaux,
71 2014a; Lardeaux et al., 2014; Franke et al., 2017), as suggested by the occurrence of
72 HP/UHP metamorphism (approximately at 400 and 360 Ma) on both sides of the Variscan
73 belt. The northern oceanic basin is identified as the Saxothuringian ocean, while the
74 southern basin can be identified as the Medio-European (Lardeaux, 2014a; Lardeaux et al.,
75 2014) or Galicia-Moldanubian (Franke et al., 2017) ocean. The width and the duration of
76 the Medio-European oceanic domain are debated, due to discrepancies between
77 metamorphic and paleo-geographic data. However, the duration of the southern ocean is
78 testified by the records of low temperature (LT) and high to ultrahigh pressure (HP/UHP)

79 metamorphism produced under a low-thermal regime that last for at least 30 Myr, which
80 implies the subduction of a significant amount of oceanic lithosphere. For the French
81 Massif Central (FMC) many authors (e.g. Faure et al., 2005, 2008, 2009; Lardeaux, 2014a)
82 proposed a Silurian north-dipping subduction of Medio-European ocean and the northern
83 margin of Gondwana underneath a magmatic arc developed on continental crust of either
84 the southern margin of Armorica or an unknown and lost microcontinent (e.g. the Ligerian
85 arc; Faure et al., 2008), followed by a late Devonian south-dipping subduction of the
86 Saxothuringian ocean. The evolution inferred from the pre-Alpine basement of the External
87 Crystalline Massifs of the Western Alps has been interpreted as compatible with the one
88 proposed for the FMC (Guillot et al., 2009).

89 Recently, Baes and Sobolev (2017) have demonstrated the possibility that a continental collision
90 following the closure of an oceanic domain on a continental side can induce external compressional
91 forces on the passive margin on the other continental side, with a consequent spontaneous initiation
92 of a new subduction with opposite vergence. Numerical models characterised by multiple
93 subductions have been widely studied (e.g., Mishin et al., 2008; Cizkova and Bina, 2015; Dai et al.,
94 2018) to better understand geodynamics processes characterising complex subduction systems, such
95 as the western Dabie orogen (Dai et al., 2018) and the Mariana-Izu-Bonin arc (Cizkova and Bina,
96 2015). On the other hand, there are few studies regarding the interaction of two opposite verging
97 subductions and only for systems characterised by very distant subductions (Holt et al., 2017),
98 without a focus on the thermo-mechanical processes of the mantle wedge. Numerical models
99 characterised by two opposite verging ocean/continent subduction systems at short distance, have
100 been developed for the first time and here proposed to verify if such a scenario better fit with
101 Variscan P-T evolutions. Our discussion focuses at first on the main features characterising a first
102 oceanic subduction; then we enlighten the effects of the velocity of this first subduction on the
103 thermal state and on the dynamics of the system during a second oceanic subduction and the
104 following continental collision.

105 P-T conditions inferred from Variscan metamorphic rocks of the Alps and the FMC have been
106 compared with those predicted for different lithospheric markers by the different models of double
107 subductions. For the comparison we used P_{\max} - $T_{P_{\max}}$ estimates because they are the most
108 representative to investigate the interaction between two active oceanic subductions. Differences in
109 the agreement with one subduction model are then discussed, to shed light on the more reliable
110 scenario on the basis of the best fit with natural data from these two portions of the European
111 Variscan belt.

112

113 **2 Variscan geological outline of the ALPS and of the FMC**

114

115 The main sections of the Variscan belt show opposite vergences of nappes and recumbent folds
116 migrating toward external Carboniferous basins. Three sutures have been described on both sides of
117 the belt (Fig. 1) and they consist of discontinuous ophiolitic massifs and/or HP/UHP metamorphic
118 relics, mainly eclogitized metabasalts (Matte, 2001):

119 (1) On the southern side of the belt, the Galicia-Southern Brittany suture is located between
120 the north Gondwana margin and the Gondwana-derived microcontinents runs from the
121 Coimbra-Cordoba Shear Zone in central Iberia (CCSZ) to southern Brittany, northern FMC
122 and further east to the southern Bohemian nappes. The CCSZ is considered as the root zone
123 of the western Iberian nappes. In Southern Brittany, the South Armorican Shear Suture Zone
124 (SASZ) partly superimposes on the Eo-Variscan suture that crops out in the Armorican
125 massif as the Nort-sur-Erdre fault. Ophiolitic rocks are dated between 500 and 470 Ma and
126 the HP/UHP metamorphism between 430 and 360 Ma (Matte, 2001). This suture may be
127 related to a N-S suture, running from the French external Alps to Sardinia and interpreted as
128 the root of W-verging pre-Permian nappes. The translation toward SW of the French
129 external Alps from Northern Europe, in prolongation with the Bohemian Massif, is related
130 to the dextral wrenching from Carboniferous to Permian times along a N030° strike-slip

131 fault, in response to oblique collision between Laurussia and Gondwana (Matte, 2001;
132 Guillot et al., 2009; Edel et al., 2013);

133 (2) On the northern side of the belt, two sutures are relatively well defined from southern
134 England, through Germany to Poland: the Teplà suture, located between the Saxothuringian
135 domain and the southern Gondwana-derived fragments, and the Rheic suture, located
136 between Avalonia and Armorica (Franke, 2000; Matte, 2001; Schulmann et al., 2009, 2014;
137 Edel et al., 2013). They are interpreted as the roots of NW-transported nappes, showing
138 HP/UHP metamorphism in the ophiolitic rocks of the Teplà suture and its continental foot-
139 wall (Konopásek and Schulmann, 2005). The oceanic rocks are dated at around 450–500 Ma
140 and the HP metamorphism took place between 380 and 330 Ma (Schulmann et al., 2005;
141 Skrzypek et al., 2014; Will et al., 2018). The Rheic suture is considered as corresponding to
142 a younger oceanic basin, which opened during Lower Devonian and closed during the Late
143 Viséan (Franke, 2000; Matte, 2001; Edel et al., 2013).

144

145 **2.1. Variscan tectono-metamorphic evolution in the Alps**

146

147 The Alps (Fig. 2) are the product of the Tertiary continental collision between the Adriatic
148 promontory of the African plate and the southern continental margin of the European-Iberian plate
149 and extends from the Gulf of Genoa to the Vienna basin. South of Genoa the Alpine range stops,
150 because it has been fragmented during the opening of the Neogene Ligurian-Provencal-Algero basin
151 and Late Neogene Tyrrhenian basin (e.g. Cavazza and Wezel, 2003; Dal Piaz et al., 2003; Dal Piaz,
152 2010; Gosso et al., in press).

153 Most of the pre-Alpine continental lithosphere recycled during the Alpine subduction shows a pre-
154 Mesozoic metamorphic evolution compatible with the evolution of the European Variscan belt (von
155 Raumer et al., 2003; Spalla and Marotta, 2007; Spiess et al., 2010; Spalla et al., 2014; Roda et al.,
156 2018a). von Raumer et al. (2003) suggested that the present day Alpine domains (Helvetic, Penninic,

157 Austroalpine and Southalpine) were probably located along the northern margin of Gondwana. In
158 many Alpine basement areas, polymetamorphic assemblages comparable to those of the
159 contemporaneous European geological framework prevail, testifying a polyphase metamorphic
160 evolution accompanied by nappe stacking during different periods (Stampfli et al., 2002; von
161 Raumer et al., 2013; Roda et al., 2018b).

162 Pre-Alpine HP metaophiolite remnants described in Helvetic to Austroalpine domains (e.g. Miller
163 and Thöni, 1995; Guillot et al., 1998; Nussbaum et al., 1998; Spalla et al., 2014; Roda et al., 2018a)
164 indicate that segments of the Variscan suture zone, incorporating the records of oceanic lithosphere
165 subduction, were included in the Alpine belt. Oldest ages of Variscan HP metamorphic imprints
166 range from Silurian to Middle-Devonian (437–387 Ma) and HP-UHP rocks display ages up to
167 Upper Mississippian (~330 Ma) (e.g. Ligeois and Duchesne, 1981; Latouche and Bogdanoff, 1987;
168 Vivier et al., 1987; Paquette et al., 1989; Messiga et al., 1992; Guillot et al., 1998; von Raumer et al.,
169 1999; Spalla and Marotta, 2007; Liati et al., 2009; Spalla et al., 2014) accounting for a long period
170 characterised by transformation of metabasites into eclogites during oceanic subduction. The
171 preserved witness of the oceanic crust is represented by the Chamrousse ophiolite, that escaped the
172 HP conditions (Fréville et al., 2018 and refs. therein). In some portions of this pre-Alpine basement
173 a subsequent recrystallisation under granulite facies conditions took place at about 340 Ma
174 (Ferrando et al., 2008; Liati et al., 2009; Rubatto et al., 2010). P-T estimates of the Variscan
175 metamorphism in the Alps are presented in Table 1. More details concerning the Variscan
176 metamorphism in the different domains of the Alps are synthesised in Appendix A (Table A1).

177

178 **2.2. Variscan tectono-metamorphic evolution in the FMC**

179

180 The European basement of the Variscan Belt experienced a long-lasting evolution from Cambrian–
181 Ordovician rifting to Carboniferous collision and post-orogenic thinning (Bard et al., 1980; Matte,
182 2001; Faure et al., 2005, 2008). In France, the Variscan Belt is well exposed in the FMC and

183 Armorican Massif, where two contrasted paleogeographic and tectonic domains are recognized. The
184 Nord-sur-Erdre Fault in the Armorican Massif corresponds to the main tectonic contact separating
185 the Armorican domain to the north and the Gondwana margin to the south (Eo-Variscan or Galicia-
186 Southern Brittany suture) (Matte, 2001; Faure et al., 2008; Ballèvre et al., 2009). The FMC (Fig. 3)
187 belongs to the western part of the Variscan chain and it is the largest area where Variscan
188 metamorphic and plutonic rocks are exposed, with the entire massif attributed to the northern
189 Gondwanian margin (Burg and Matte, 1978; Matte, 1986; Mercier et al., 1991; Faure et al., 2005,
190 2009). P-T estimates of the Variscan metamorphism in the FMC are presented in Table 2.

191 The FMC is a stack of metamorphic nappes, in which six main units are recognized, from the
192 bottom to the top and from the south to the north (Ledru et al., 1989; Faure et al., 2009; Lardeaux et
193 al., 2014; Lardeaux, 2014a): (1) the southernmost turbidites fore-land basin (middle to late
194 Mississippian); (2) the Palaeozoic fold-and-thrust belt of the Montagne Noire area, composed of
195 weakly metamorphosed sediments (early Cambrian to early Carboniferous); (3) the Para-
196 autochthonous unit (PAU) over-thrusting the southern fold-and-thrust belt and metamorphosed
197 under greenschist to epidote-amphibolite facies conditions; (4) the Lower Gneiss Unit (LGU),
198 metamorphosed under amphibolite facies conditions; (5) the Upper Gneiss Unit (UGU), which
199 experienced upper Silurian/lower Devonian to middle Devonian HP to UHP metamorphism, and
200 characterised by the occurrence, in the lowermost part, of a bimodal association called ‘Leptyno-
201 Amphibolitic Complex’ (LAC) that is interpreted as a subducted and exhumed Cambro–Ordovician
202 ocean-continent transition (OCT); (6) the uppermost units are identified by the Brévenne and
203 Morvan units in the eastern FMC and by the Thiviers-Payzac unit (TPU) in the western FMC. The
204 tectonic architecture of the FMC can be well illustrated by three mainly NS-orientated cross-
205 sections over the eastern, the central and western parts, through which the main metamorphic and
206 tectonic stages can be reconstructed. A detailed description of the main units in the cross-sections of
207 the FMC is in Appendix A (Table A2).

208 The stack of nappes recognised in the FMC is the result of successive tectonic and metamorphic
209 stages. Considering the period from Silurian to Visean, which is the time span covered by our
210 models, four stages can be distinguished:

211 (1) The D0 event is coeval with a Silurian–Early Devonian HP to UHP metamorphism
212 recorded in the whole FMC in the eclogites of the LAC at pressures higher than 2 GPa and
213 temperatures of 700–800 °C, as in the eclogites of Mont du Lyonnais (Lardeaux et al., 2001);

214 (2) The D1 event is coeval with a Middle Devonian metamorphism recorded in both the
215 UGU and the LGU and associated to isothermal decompression in the western FMC and
216 decompression with an increase of temperature in the eastern FMC, up to pressure of 0.7–1
217 GPa and temperatures of 650–750 °C, such as in the UGU of Mont du Lyonnais (Lardeaux
218 et al., 2001) and in the LGU of southern Limousine (Faure et al., 2008);

219 (3) The D2 is a Late Devonian–Early Carboniferous event is coeval with the emplacement in
220 the northeastern FMC of volcanic rocks (Morvan magmatic arc) and Brévenne-Beaujolais
221 ophiolite. The relative position of the Morvan arc to the north and the Brévenne-Beaujolais
222 back-arc to the south argues for a south-dipping subduction;

223 (4) The D3 event is coeval to low- and very low-grade Visean metamorphism and the
224 progressive exhumation of the tectonic units previously involved in the nappe stack, with the
225 exception of high temperatures recorded in the southern and southeastern FMC.

226

227 **3 Model setup**

228

229 The proposed models of two opposite subductions (now on “models DS”) simulate the thermo-
230 mechanical evolution of an ocean/continent/ocean/continent subduction complex during four
231 tectonic phases over a period of 130 Myr (Fig. 4):

- 232 (1) a first active oceanic subduction (phase 1) that lasts 51.5 Myr (from 425 to 373.5 Ma),
233 until the continental collision, and characterised by three different velocities of plate
234 subduction O1: 1, 2.5 and 5 cm/yr;
- 235 (2) a post-collisional phase (phase 2), which lasts 10 Myr (from 373.5 to 363.5 Ma) and is
236 controlled by sole gravitational forces;
- 237 (3) a second opposite active oceanic subduction (phase 3) that lasts 26.5 Myr (from 363.5 to
238 337 Ma), until the second continental collision, with a prescribed velocity of 5 cm/yr of
239 plate O2;
- 240 (4) a final post-collisional phase (phase 4) that lasts 42 Myr (from 337 to 295 Ma) and, as
241 phase 2, is controlled by sole gravitational forces.

242 The time span covered by the four phases covers the same time span of one cycle model (now on
243 “models SS”) after Regorda et al. (2017), which is characterised by two tectonic phases: (1) an
244 initial oceanic subduction (phase 1) lasting 51.5 Myr (from 425 to 373.5 Ma), with a prescribed
245 velocity of 5 cm/yr; (2) a post-collisional phase (phase 2) lasting 78.5 Myr (from 425 to 295 Ma).

246

247 For what concerns phase 1 of models DS, the width of the oceanic domain involved in the first
248 north verging subduction (plate O1), representing here the Medio-European ocean, is different for
249 the three models. The oceanic domain is assumed to be 500, 1250 and 2500 km wide for velocities
250 of 1, 2.5 and 5 cm/yr, respectively. The dimensions of the ocean for velocities of subduction of 1
251 and 2.5 cm/yr are compatible with the paleo-geographic reconstructions proposed for the FMC. The
252 first subduction collision cycle consists of phases 1 and 2. The oceanic domain involved in the
253 second subduction (plate O2 during phase 3), representing here the Saxothuringian ocean, is 1250
254 km wide in all models, according to a duration of the oceanic subduction of approximately 25 Myr
255 (Lardeaux, 2014a; Lardeaux et al., 2014). The second subduction collision cycle consists of phases
256 3 and 4. The continent between the two oceanic domains (C3) is 400 km wide, in agreement with
257 the dimension of Armorica inferred balancing the cross-sections through the Variscan belt in France

258 (Matte, 2001). The assumed time lag of 10 Myr between the first continental collision and the
 259 initiation of the second oceanic subduction (phase 2) is compatible with the results obtained by
 260 Baes and Sobolev (2017) concerning the spontaneous oceanic subduction initiation close to a
 261 continental collision.

262 For what concerns phase 1 of model SS, the oceanic domain involved in the long-lasting south-
 263 dipping subduction represents the Rheic ocean. Mono-cyclic scenarios of the Variscan orogeny
 264 suggest that a ~2500 km-wide ocean closed in approximately 50 Myr (Malavieille, 1993; Tait et al.,
 265 1997; Torsvik, 1998; von Raumer et al., 2003; Marotta and Spalla, 2007). Accordingly, we assumed
 266 a velocity of subduction of 5 cm/yr.

267 The list of acronyms and setup of the models are summarised in the insets in Fig. 4.

268 The physics of the crust-mantle system is described by the equations of continuity, of conservation
 269 of momentum and of conservation of energy, which include the extended Boussinesq
 270 approximation (e.g., Christensen and Yuen, 1985) for incompressible fluids. These equations are
 271 expressed as follows:

$$272 \quad \nabla \cdot \mathbf{u} = 0 \quad (1)$$

$$273 \quad -\nabla P + \nabla \cdot \boldsymbol{\tau} + \rho \mathbf{g} = 0 \quad (2)$$

$$274 \quad \rho c_p \left(\frac{\partial T}{\partial t} + \mathbf{u} \cdot \nabla T \right) = \nabla \cdot (K \nabla T) + H_r + H_s + H_a \quad (3)$$

275 where \mathbf{u} is the velocity, P is the pressure, $\boldsymbol{\tau}$ is the deviatoric stress, ρ is the density, \mathbf{g} is
 276 gravity acceleration, c_p is the specific heat at a constant pressure, T is the temperature, K is the
 277 thermal conductivity, H_r is the radiogenic heating, $H_s = \boldsymbol{\tau}_{ij} \dot{\epsilon}_{ij}$ is the heating due to viscous
 278 dissipation, $H_a = T \alpha \frac{DP}{Dt} \approx -\alpha T \rho g v_y$ is the adiabatic heating and α is the volumetric thermal
 279 expansion coefficient. Specific heat has been fixed to $1250 \text{ J kg}^{-1} \text{ K}^{-1}$ and the thermal expansion
 280 coefficient has been fixed to $3 \cdot 10^{-5} \text{ K}^{-1}$.

281 Equations 1, 2 and 3 are numerically integrated via the 2D finite element (FE) thermo-mechanical
 282 code SubMar (Marotta et al., 2006), which uses the penalty function formulation to integrate the

283 conservation of momentum equation and the Petrov-Galerkin method to integrate the conservation
 284 of energy equation. The numerical integration has been performed in a rectangular domain, 1400
 285 km wide and 700 km deep (Fig. 4), discretized by a non-deforming irregular grid composed of 4438
 286 quadratic triangular elements and 9037 nodes, with a denser nodal distribution near the contact
 287 region between the plates, where the most significant gradients in temperature and velocity fields
 288 are expected. The size of the elements varies horizontally from 10 to 80 km and vertically from 5 to
 289 20 km, and smaller elements are located close to the active margin regions. To differentiate the
 290 crust from the mantle, we use the Lagrangian particle technique (e.g., Christensen, 1992) as
 291 implemented in Marotta and Spalla (2007), Meda et al. (2010) and Roda et al. (2010, 2012). At the
 292 beginning of the evolution, 288,061 markers identified by different indexes are spatially distributed
 293 at a density of 1 marker per 0.25 km^2 to define the upper oceanic crust, the lower oceanic crust and
 294 the continental crust. Material properties and rheological parameters are summarised in Table 3.
 295 During the evolution of the system, each particle is advected using a 4th-order Runge-Kutta scheme.
 296 Being $C_i^e = N_i^e / N_0^e$, with N_i^e the number of particles of type i inside the element e and N_0^e the
 297 maximum number of particles that element e can contain, the density of each element may be
 298 expressed as:

$$299 \quad \rho^e(C^e, T) = \rho_0 [1 - \alpha(T - T_0)] - \sum_i \Delta \rho_i^e C_i^e \quad (4)$$

300 where the index i identifies the particle type, ρ_0 is the reference density of the mantle at the
 301 reference temperature T_0 , and $\Delta \rho_i^e$ is the differences between ρ_0 and the density of the upper
 302 oceanic crust, $(\Delta \rho_i^e = \rho_{oc_u} - \rho_0)$, of the lower oceanic crust, $(\Delta \rho_i^e = \rho_{oc_l} - \rho_0)$, and of the continental
 303 crust, $(\Delta \rho_i^e = \rho_{cc} - \rho_0)$.

304 Similarly, the viscosity of each element may be expressed as:

$$305 \quad \mu^e(C^e, T) = \mu_m \left[1 - \sum_i C_i^e \right] + \sum_i \mu_i C_i^e \quad (5)$$

306 with

$$\mu_i = \mu_{0,i} e^{\left[\frac{E_i}{R} \left(\frac{1}{T} - \frac{1}{T_0} \right) \right]} \quad (6)$$

where $\mu_{0,i}$ is the reference viscosity at the reference temperature T_0 , and E_i and n_i are the activation energy and the exponent, respectively, of the power law for the mantle, upper oceanic crust, lower oceanic crust and continental crust.

Free slip conditions have been assumed along the upper boundary of the 2D domain and no-slip conditions have been assumed along the other boundaries (Fig. 4). In addition, a velocity is prescribed along the bottom of the oceanic crust during the active subduction phase (O1 during phase 1 and O2 during phase 3). The same velocity is also prescribed along a 45° dipping plane that extends from the trench to a depth of 100 km to facilitate the subduction of the oceanic lithosphere. Differently, no velocities are prescribed during the two post-collisional phases (phases 2 and 4) and the system undergoes a pure gravitational evolution.

Fixed temperatures have been assumed at the top (300 K) and at the bottom (1600 K) of the model. Zero thermal flux is imposed at the vertical side-wall facing the subduction and fixed temperature along the opposite vertical side. The initial thermal structure corresponds to a conductive thermal gradient throughout the lithosphere, with temperatures that vary from 300 K at the surface to 1600 K at its base and a uniform temperature of 1600 K below the lithosphere. The base of the lithosphere is located at a depth of 80 km under both the oceanic and continental domains. This thermal configuration corresponds to either an oceanic lithosphere of approximately 40 Myr (based on the cooling of a semi-infinite half space model, Turcotte and Schubert, 2002) and a thinned continental passive margin based on a medium to slow spreading rate of 2–3 cm/yr (e.g., Marotta et al., 2016). The 1600 K isotherm defines the base of the lithosphere throughout the evolution of the system.

Models also account for mantle hydration associated to the dehydration of H₂O-saturated MORB basalt, which transport water in their hydrous phases up to 300 km deep, as implemented in Regorda et al. (2017). The maximum depth at which dehydration takes place is identifiable by the

332 depth of the deepest oceanic marker in the stability field of lawsonite. The progressive hydration of
333 the mantle wedge is defined by the stability field of the serpentine (Schmidt and Poli, 1998). In the
334 hydrated domains we assume a viscosity of 10^{19} Pa·s and a density of 3000 kg/m^3 (Schmidt and Poli,
335 1998; Honda and Saito, 2003; Arcay et al., 2005; Gerya and Stockhert, 2006; Roda et al., 2010).

336

337 **4 Model predictions**

338

339 Below, the presentation will focus initially on the first cycle of oceanic subduction and continental
340 collision (phases 1 and 2, Chapter 4.1) and afterwards on the thermo-mechanics evolution
341 characterising the second cycle of oceanic subduction and continental collision (phases 3 and 4,
342 Chapter 4.2). Being the thermo-mechanic evolution of systems characterised by a single subduction
343 activated in an unperturbed environment, widely described and discussed in a previous work of the
344 same authors (e.g., Regorda et al., 2017), for phases 1 and 2 we will enlighten only the main
345 features. For phases 3 and 4 we will enlighten differences in the dynamics and in the thermal state
346 predicted by models characterised by different prescribed velocities of the first subduction. The
347 thermal states predicted by models DS during phases 2, 3 and 4 will be then compared to the post-
348 collisional phase of Regorda et al. (2017)'s model (SS.5 model).

349

350 **4.1. First subduction-collision cycle (phases 1 and 2)**

351

352 Results will be discussed in relation to three values of subduction velocities: 1, 2.5 and 5 cm/yr
353 (models DS.1, DS.2.5 and DS.5, respectively). One major effect that deserves to be enlighten here
354 is that the higher the velocity of subduction, the lower the temperature in the slab and in the mantle
355 wedge (see isotherms 800 and 1100 K in Fig. 5), since cold material is buried more rapidly than it
356 can be warmed by heat conduction, mantle convection, viscous heating or other heat sources. The
357 consequence of the higher temperatures for lower velocities is that the area in which the P-T

358 conditions are compatible with the stability field of the serpentine is smaller (blue areas in Fig. 5a–c)
359 and the convective cells in the mantle wedge are less efficient for recycling subducted oceanic and
360 continental crustal material. In particular, the slab of the first subduction of model DS.1 is
361 characterised by temperatures too high to promote hydration in large domains of the mantle wedge
362 and, therefore, recycling of subducted crust (see streamlines in Fig. 5a).

363 During phase 2, models evolve in a similar way regardless of the prescribed subduction velocity
364 during phase 1 because their dynamics is controlled only by gravitational forces. Briefly, the large-
365 scale convective flow gradually expands laterally towards the overriding plate, reducing the slab
366 dip. At the same time, the convective flow underneath the upper continental plate disappears
367 provoking a thermal re-equilibration in the entire system, with a warming of the subducted
368 lithosphere and a cooling of the mantle wedge. The general dynamics is characterised by a rising of
369 all the subducted material because of the lower density with respect to the surrounding mantle,
370 which determines the doubling of the crust at the end of the phase 2.

371

372 **4.2. Second subduction-collision cycle (phases 3 and 4)**

373

374 The sinking of slab 2 determines a gradual backward bending of slab 1 (Fig. 6), associated to a
375 thinning below a depth of approximately 150 km. The mantle flow above the slab is very weak,
376 with the exception of model DS.5 in which it intensifies at about 15.5 Myr (Fig. 6b₃). The lack of an
377 intense large-scale mantle flow in models DS.1 and DS.2.5 can be related to the presence of the slab
378 1 that prevents its activation. Differently, the mantle flow enhancing in model DS.5 after 15.5 Myr
379 is ascribable to the higher dip angle of the slab with a consequent wider area available above it. In
380 addition, the presence of the short-lived convective flow in the model DS.5 (Fig. 6b₃) determines an
381 increase of temperature at the bottom of the slab 1 with respect to models DS.1 and DS.2.5 (Fig. 6b₁
382 and b₂, respectively) and a decrease of its dip. However, since large-scale mantle flow is limited
383 above slab 2 and below slab 1, the area between the two subduction complexes is not thermally

384 affected by the large-scale mantle flow, as occurs during phase 1. Differently, the large-scale
385 convective cell below the second slab is of the same order of magnitude for all models and
386 comparable with the flow activated during phase 1 below the slab 1 (Fig. 6).

387 Fig. 7 shows that at the beginning of the second active oceanic subduction (phase 3) the upper plate
388 is still thermally perturbed. In particular, slab 1 is not yet thermally re-equilibrated, as shown by the
389 depression of isotherms 1100 K (dashed lines in Fig. 7a). Comparing the isotherm 1100 K predicted
390 by models DS.1, DS.2.5 and DS.5 during phase 3 inside slab 1 (dashed black, red and blue lines,
391 respectively, in Fig. 7a and b) is evident that during the early stages model DS.5 is the coldest,
392 while model DS.1 is the warmest. This is the consequence of the colder thermal state for higher
393 velocities at the end of phase 1. During the early stages of phase 3, isotherms 800 K predicted by
394 models DS.1, DS.2.5 and DS.5 in the micro-continent C3 show no differences (continuous black,
395 red and blue lines in Fig. 7a and b, respectively) and they are shallower than in an unperturbed
396 system (phase 1 of model SS.5, continuous green line in Fig. 7c and d). This because the geotherm
397 at the beginning of phase 1 is colder than the geotherm at the beginning of phase 3 (Fig. 7a).
398 Consequently, the difference between DS and SS models diminishes during the evolution (Fig. 7b)
399 and it disappears in the latter stages of phase 3 (Fig. 7c and d). Further from the second subduction
400 ($x > 250$ km in Fig. 7), model DS.1 shows the lowest temperatures while model DS.5 is the warmest.
401 This is due to the amount of continental material of the lower plate subducted during the collision
402 (Fig. 6). In fact, for higher velocities of subduction (i.e. models DS.2.5 and DS.5) the larger amount
403 of continental material subducted determined the thickening of the crust and the consequent higher
404 temperatures due to higher radiogenic energy (see also Regorda et al., 2017).

405 For what concerns slab 2, the isotherm 800 K shows only a slight difference after 5.5 Myr, when it
406 is slightly deeper in model DS.1 (continuous black line in Fig. 7b) with respect to models DS.2.5
407 and DS.5 (continuous red and blue lines in Fig. 7b, respectively). The thermal state begins to clearly
408 differentiate after 15.5 Myr from the beginning of phase 3 (Fig. 7c), when isotherm 800 K is the
409 deepest in model DS.1 and it is the shallowest in model DS.5. Further differences can be observed

410 at the continental collision at the end of phase 3 (continuous lines in Fig. 7d), when model DS.5
411 (continuous blue line) is warmer than models DS.1 and DS.2.5 (continuous black and red lines) but
412 is colder than model SS.5 (continuous green line). In the same way, 1100 K isotherm begins to
413 show differences in the portion of the wedge close to the second subduction after approximately
414 15.5 Myr (dashed lines in Fig. 7c), with a colder thermal state for models DS.1, DS.2.5 and DS.5
415 (dashed black, red and blue lines, respectively) with respect to the phase 1 of model SS.5 (dashed
416 green line). The colder thermal state in the wedge predicted during phase 3 could be related to the
417 lack of heat supply due to the mantle flow that, in case of double subduction, does not reach the
418 portion of the wedge close to slab 2. In correspondence of the doubled crust related to the first
419 continental collision, isotherms 1100 K (dashed black, red and blue lines, respectively, in Fig. 7c
420 and d) are shallower than the isotherm in a non-thickened crust (dashed green line in Fig. 7c and d),
421 because of the higher energy supplied by radioactive decay.

422 Focusing on the wedge area (Fig. 8a, b and c for models DS.1, DS.2.5 and DS.5, respectively) we
423 can observe that the local dynamics is comparable to that characterising phase 1, with slight
424 differences due to the lower temperatures predicted during phase 3 inside slab 2. In fact, the
425 hydrated area is more extended in models DS.1 and in DS.2.5 (blue areas in Fig. 8a₁ and b₁,
426 respectively) with respect to model DS.5 (blue area in Fig. 8c₁), because of the colder thermal state
427 and the consequent larger portion of mantle wedge in which the serpentine is stable. Differences in
428 the extension of the hydrated area are more evident at the end of the subduction, when differences
429 of the thermal conditions in the slab are more pronounced (blue areas in Fig. 8a₂, b₂ and c₂ for
430 models DS.1, DS.2.5 and DS.5, respectively).

431 After the second continental collision, for all models the large-scale convective flow shows a
432 decrease in the intensity below slab 2 of approximately two orders of magnitude (streamlines in Fig.
433 9). On the other hand, above slab 2 the activation of a feeble convective cell of the same order of
434 magnitude occurs and it decreases its intensity at the end of phase 4 (streamlines in Fig. 9b₁, b₂ and
435 b₃ for models DS.1, DS.2.5 and DS.5, respectively). The combined action of these two large-scale

436 convective cells determines the increase of the dip angle of the deep portion of both subducted slabs.
437 At the same time, both the subducted portion of the continental crust of the lower plate and the
438 recycled material in the wedge rise to shallower depths, because of their lower densities with
439 respect to the mantle.

440 The portion of the slab characterised by temperatures below 800 K thermally re-equilibrates by the
441 first 10 Myr of phase 4, as shown by the isotherm 800 K (continuous black, red and blue lines in
442 Fig. 7e and f) that does not show differences with respect to isotherm 800 K predicted by model
443 SS.5 during phase 2 (green continuous line in Fig. 7e and f). Differently, isotherms 1100 K have
444 different maximum depths for the models until the last stages of the evolution. In particular,
445 isotherm 1100 K reach a depth of approximately 150 km in DS.1 model (black dashed line in Fig.
446 7f), more than 150 km in DS.2.5 model (red dashed line in Fig. 7f), of approximately 100 km in
447 DS.5 model (blue dashed line in Fig. 7f) and of less than 100 km during phase 2 of SS.5 model
448 (green dashed line in Fig. 7f). The slower thermal re-equilibration and the final colder thermal states
449 of model DS.2.5 and, to a lesser extent, of models DS.1 and DS.5 with respect to model SS.5 are
450 related to the lower temperatures predicted at the end of phase 3.

451 Fig. 10 shows differences in temperature, in terms of isotherms 800 (continuous lines) and 1100 K
452 (dashed lines), between models DS.1, DS.2.5 and DS.5 (black, red and blue lines, respectively) and
453 model SS.5 (green lines) after the first continental collision. Model SS.5 remains warmer than
454 models DS.1, DS.2.5 and DS.5 during the whole evolution, due to the constant warming that
455 characterises the post-collisional phase (phase 2) of model SS.5 (green lines in Fig. 10). Differently,
456 phase 3 of models DS is characterised by a cooling of the subduction complex because of the
457 activation of the second oceanic subduction (black, red and blue lines in Fig. 10a), followed by a
458 thermal re-equilibration during phase 4 (black, red and blue lines in Fig. 10b).

459

460 **5 Comparisons with natural P-T-t estimates**

461

462 The P-T conditions estimated for rocks of the Variscan crust from the Alps and the FMC are
463 compared with predictions of double subductions models, for the first subduction-collision cycle
464 (phases 1 and 2, Chapter 5.1) and for the second subduction-collision cycle (phases 3 and 4, Section
465 5.2). We also enlighten the differences in the agreement with respect to model with a single
466 subduction (Section 5.3) to infer the best fitting geodynamic scenario responsible for the building of
467 the Variscan chain.

468 The French Massif Central is an example of a Silurian metamorphic evolution in relation with
469 hotter subduction system (Lardeaux, 2014). The high thermal state inferred by natural data during
470 the first Silurian–early Devonian subduction is in agreement with the thermal states predicted
471 during phase 1 by models DS.1, DS.2.5 and DS.5, which is higher than that predicted during phase
472 3. However, model DS.1 does not show recycling of subducted crust during the first subduction and
473 model DS.5 has a wider oceanic domain than that proposed by paleo-geographic reconstructions
474 that consider two successive oceanic subductions. Therefore, assuming a geodynamic
475 reconstruction for the Variscan orogeny characterised by two opposite subductions during Silurian–
476 early Devonian and late Devonian–Carboniferous, model DS.2.5 appears as the most adequate to
477 make a comparison with natural P-T estimates of the Variscan metamorphism recorded in the Alps
478 and in the FMC.

479 The P-T conditions recorded by the markers of the models DS.2.5 and SS.5 have been compared
480 with P_{\max} - $T_{P_{\max}}$ estimates related to the Variscan metamorphism inferred from both continental
481 basement rocks of the Alpine domain (Table 1) and of the FMC (Table 2). The distribution of the
482 data is represented in Figs. 2 and 3, respectively.

483 We assume that there could be a complete agreement between geological data and model
484 predictions only if the following three conditions are satisfied contemporaneously:

- 485 (1) coincident lithological affinity with oceanic crust, continental crust and mantle;
- 486 (2) comparable P_{\max} - $T_{P_{\max}}$ estimates and P-T conditions predicted by the model. P-T
487 estimates have different precisions; for example, the minimum pressure only has been

488 estimated for datum Pv1 from the Savona massif in the Penninic domain and datum Av9
489 from the Languard-Campo nappe in the Austroalpine domain, or the minimal pressure only
490 has been estimated for datum ML1 from Mont du Lyonnais, while all data from the
491 Southalpine domain in the Alps and from Rouergue in the FMC have more precise P-T
492 estimates, including both minimal and maximal values;

493 (3) same ages of the P_{\max} - $T_{P_{\max}}$ estimates and the P-T conditions predicted by the model.
494 Data in red in Fig. 11 have an estimated geological age, such as data Sv11 and Sv12 from
495 the Eisecktal in the Southalpine domain and data Ar1 and Ar2 from Artense in the FMC;
496 data in black have a radiometric well-constrained age, such as data Pv8 and Pv9 from the
497 Adula nappe in the Penninic domain and data Li3, Li4 and Li5 from Limousin in the FMC.
498 The latter more precise proposed ages make their fitting with model predictions more
499 significant.

500 Data from the Alps will be discussed considering their distribution in the present domains (Helvetic,
501 Penninic, Austroalpine and Southalpine domains) as in Fig. 2, while data from the FMC will be
502 discussed considering their belonging to the main units recognised in the FMC (Upper Gneiss Unit,
503 Lower Gneiss Unit, Para-autochthonous Unit, Thiviers-Payzac Unit and Montagne Noire) as
504 showed in Fig. 3.

505

506 **5.1. First subduction-collision cycle (phases 1 and 2)**

507

508 The first subduction-collision cycle consists of phase 1, corresponding to a north verging oceanic
509 subduction and lasting between 425 and 373.5 Ma (i.e. upper Silurian to Frasnian), and of the
510 successive phase 2, controlled by sole gravitational forces and lasting between 373.5 and 363.5 Ma.
511 These two phases can be related to deformation events D0 and D1 observed in the FMC.

512

513 *5.1.1. Alps*

514 *Helvetic domain* – Data Hv3 and Hv4 from Belledonne and data from Pelvoux (data Hv6 and Hv7)
515 and Aiguilles Rouges (data Hv11 and Hv12) in the Helvetic domain that fit with the model
516 predictions during phase 1 (Fig. 11a) recorded pressures over 0.8 GPa in a wide range of
517 temperatures (between 530 and 930 °C) and have lithological affinities only with continental
518 markers (brown and red points in Fig. 12a). During the early stages of phase 1, P_{\max} - $T_{P_{\max}}$ estimates
519 fit with both subducted markers eroded by the upper plate, as samples Hv6 and Hv7 from Pelvoux
520 and samples Hv11 and Hv12 from Aiguilles Rouges (Fig. 13a) and markers at the bottom of the
521 crust of the upper plate, as sample Hv12 from Aiguilles Rouges (Fig. 13a), depending on their
522 estimated pressure. Differently, no agreement with the oceanic markers occurs, because their
523 predicted temperatures are too low (below 530 °C) for all the estimated P-T conditions in rocks
524 from the Helvetic domain. Proceeding with the evolution, the upper plate warms up and markers in
525 the deep portion of the crust start fitting with sample Hv4 from Belledonne (Fig. 13b–d), while
526 sample Hv12 from Aiguilles Rouges fits only in the colder, internal and shallow portion of the
527 wedge (Fig. 13b–d). During the last stages of phase 1 P-T values estimated from samples from
528 Belledonne (Hv3 and Hv4), Pelvoux (Hv6) and Aiguilles Rouges (Hv11 and Hv12) agree also with
529 the subducted portion of the lower continental plate (Fig. 13d).

530 *Penninic domain* – In the early stage of phase 1 there is correspondence between P-T values
531 inferred from rocks of the Gran Paradiso massif (Pv3), Suretta (Pv10) and the Tauern window
532 (Pv11 and Pv12) and model predictions (Fig. 11a). Pv3 estimated conditions from the Gran
533 Paradiso massif are characterised by intermediate P/T ratio (Fig. 12b) and show the agreement with
534 markers in the external and shallow portion of the wedge. Differently, data from Suretta (Pv10) and
535 the Tauern window (Pv11 and Pv12) are characterised by high P/T ratio (Fig. 12b) and fit with
536 markers either in the internal and shallow portion of the wedge, as estimates Pv11 from Suretta, or
537 in the deeper portion, as estimates Pv10 and Pv12 from the Tauern window (Fig. 13a and b). In the
538 second part of phase 1, data that fit with the model can be divided in two groups: the first group is
539 composed by rocks with re-equilibrations characterised by intermediate P/T ratio, pressures below

540 0.8 GPa and temperatures between 530 and 630 °C (Fig. 12b), from the Gran Paradiso massif (Pv2,
541 Pv3), Monte Rosa (Pv4) and the Grand St. Bernard nappe (Pv7); the second group is, instead,
542 characterised by high P/T ratio, pressures above 1.8 GPa and temperature over 630 °C (Fig. 12b),
543 from the Savona massif (Pv1), the Central Adula nappe (Pv8) and Suretta (Pv10). P-T values
544 estimated from rocks of the first group show correspondences with continental markers in the
545 shallow and external portion of the wedge, as Pv3 from the Orco valley in the Gran Paradiso massif
546 (Fig. 13c and d) or at the bottom of the crust of the upper plate, as Pv2 from Gran Paradiso, Pv4
547 from Monte Rosa and Pv7 from the Grand St. Bernard nappe (Fig. 13c and d). Differently, P-T
548 conditions inferred from rocks of the second group show an agreement with recycled oceanic and
549 continental markers on the deep and external portion of the wedge, as in samples Pv1 from the
550 Savona massif, Pv8 from the Central part of the Adula nappe and Pv10 from Suretta (Fig. 13c and
551 d).

552 *Austroalpine domain* – Rocks from the Hochgrossen massif (Av1), the Silvretta nappe (Av7) and
553 the Languard-Campo nappe (Av9) of the Austroalpine domain have recorded the peak of the
554 Variscan metamorphism between 375 and 425 Ma (Fig. 11a) and they are characterised by high P/T
555 ratios (Fig. 12c). All these data fit during phase 1 with deeply subducted oceanic and continental
556 markers. In particular, data from the Hochgrossen and the Silvretta nappe (Av1 and Av7,
557 respectively) have correspondences with oceanic and continental markers in the external portion of
558 the wedge, during their recycling (Fig. 13b and c). In addition, at the end of phase 1, Av4 from the
559 Tonale Zone fits both with the subducted portion of the lower plate and with recycled markers in
560 the external portion of the wedge (Fig. 13d).

561 *Southalpine domain* – P-T conditions recorded in rocks from the Domaso-Cortafò Zone and the
562 Eisecktal (Sv2 and Sv12, respectively) of the Southalpine domain were recorded under intermediate
563 P/T ratios while those from Tre Valli Bresciane (Sv10) are characterised by high P/T ratio (Fig.
564 12d). Among these metamorphic records, the one from the Eisecktal (Sv12) has the lowest P/T ratio
565 and it fits with markers in the deep portion of the crust of the upper plate (Fig. 13b–d) during phase

566 1. Differently, those from Sv10 of Tre Valli Bresciane have the highest P/T ratio and are in
567 agreement with the model predictions characterising the external portion of the wedge, at a depth of
568 about 45 km (Fig. 13d). Peak-conditions estimated from rocks of the Domaso-Cortafò Zone (Sv2)
569 developed under a intermediate P/T ratio between those deriving from Tre Valli Bresciane and the
570 Eisecktal estimates and find correspondences with markers at the bottom of the crust of the upper
571 plate (deeper than Sv12 from the Eisecktal) and in the wedge, in a shallower area with respect to
572 Sv10 from Tre Valli Bresciane (Fig. 13c and d). All of these estimated P-T values show an
573 agreement also with the lower plate: metamorphic conditions available for the Domaso-Cortafò
574 Zone and the Eisecktal fit with those predicted for continental markers in the deep portion of the
575 non-subducted plate, while Sv10 from Tre Valli Bresciane fit with the thermal state predicted for
576 continental markers in the subducted portion of the lower plate (Fig. 13d).

577 Given the short duration of the phase 2, the subduction complex is not completely thermally re-
578 equilibrated and the thermal state is similar to that recorded at the end of phase 1. Then, all data
579 from the Alps show the same agreement with the model with respect to phase 1 (Figs. 11a and 13e).

580

581 *5.1.2 French Massif Central*

582 *Upper Gneiss Unit* – In the early stage of phase 1, the model predictions show agreement only with
583 data from the UGU (red dots in Fig. 14), in particular from Limousin (Li2), Mont du Lyonnais
584 (ML1), Rouergue (Ro3), Artense (Ar1) and Maclas (Mc1, Fig. 11b). All of them are characterised
585 by high P/T ratios, with pressures above 1.2 GPa and temperatures over 700 °C (Fig. 12e). With the
586 exception of ML1 from Mont du Lyonnais, which consist of a garnet-bearing peridotite, therefore
587 with mantle affinity, all the data fit both with continental subducted markers eroded from the base
588 of the crust of the upper plate and with recycled oceanic markers (Fig. 14a). Proceeding with the
589 evolution, both data from the UGU characterised by high P/T ratios, such as those from Limousin
590 (Li2), La Bessenoits (LB1), Mont du Lyonnais (ML2), Rouergue (Ro2), Artense (Ar1) and Maclas
591 (Mc1), and data from the UGU with intermediate P/T ratios, such as those from Limousin (Li5) and

592 from Mont du Lyonnais (ML4), agree with the predicted thermal state (Fig. 11b). In particular,
593 values characterised by intermediate P/T ratios find correspondences with continental markers at the
594 bottom of the upper plate, while those characterised by high P/T ratios fit with both subducted and
595 recycled markers (Fig. 14b–d). LB1 from La Bessenoits fits with subducted continental markers in
596 the external portion of the slab (Fig. 14b), while Ma1 does not fit with predictions of the model
597 even though is characterised by similar P-T conditions, because rocks in Maclas area have an
598 oceanic affinity and in the model predictions no oceanic markers are located in the PT-field
599 compatible with the natural data. On the other hand, datum Ro2 from Rouergue fit also with oceanic
600 markers in the internal portion of the slab (Fig. 14c), characterised by a lower estimated temperature
601 with respect to datum Ma1. Data from Limousin (Li2), Haut Allier (HA1), Artense (Ar1), Maclas
602 (Ma1) and Mont du Lyonnais (ML2) have a high P/T ratio and temperatures higher than data LB1,
603 Ma1 and Ro3. Consequently, they begin to fit with continuity after 25–30 Myr from the beginning
604 (Fig. 14c–e), when there is an increase of crustal material in the external and warmer portion of the
605 hydrated wedge. All data with intermediate-to-high and intermediate P/T ratios, such as PA1 from
606 Plateau d’Aigurande, Ro3 from Rouergue, ML4 from Mont du Lyonnais and Li5 from Limousin,
607 show a good fit at the bottom of the upper plate and in the external and shallower portions of the
608 wedge during the second half of phase 1 (Fig. 14c). During phase 2, re-equilibration conditions of
609 rocks from Artense (Ar1), Maclas (Mc1) and Rouergue (Ro1), characterised by high P/T ratios,
610 continue to fit also with markers in the wedge, while P-T values characterised by intermediate P/T
611 ratios, such as data ML4 and Ro3, fit at the bottom of the crust of both the upper and the lower plate
612 (Fig. 14d and e).

613 *Lower Gneiss Unit* – Data from the LGU (blue dots in Fig. 14) with estimated geological ages
614 compatible with phases 1 and 2 are only Li1 and Li4 from Limousin and Ar2 from Artense. Data
615 Li1 and Ar2 are characterised by intermediate P/T ratios and fit with continuity during the entire
616 phase 1 with continental markers at the bottom of the upper plate, up to the most internal and
617 shallowest portion of the wedge (Fig. 14a–c). After the collision and during phase 2, datum Ar2 fits

618 also with continental markers of the bottom of the lower plate (Fig. 14d and e). Datum Li4 is one of
619 the two data characterised by high P/T ratio not in the UGU (the other is MN1 from Montagne
620 Noire). It is also characterised by the highest P/T ratio and shows a very good fit with oceanic
621 markers in the internal portion of the slab (Fig. 14b).

622 *Para-autochthonous Unit* – Only datum PA2 belonging to PAU from Plateau d'Aigurande has
623 proposed ages compatible with phases 1 and 2 and it is characterised by intermediate P/T ratios. It
624 has estimated ages compatible with the last stages of phase 1, fitting very well at the bottom of the
625 upper plate, up to the most internal and shallowest portion of the wedge (Fig. 14). Moreover, PA2
626 continues to fit during the entire phase 2 at the bottom of the continental crust of both plates (Fig.
627 14d and e). Its fitting during D0 and D1 events is due both to uncertainty of age and to the PT
628 conditions at the bottom of the upper plate that do not change significantly during the evolution of
629 the model. In fact, it shows a fit also during phase 3 (D2 event).

630

631 **5.2. Second subduction-collision cycle (phases 3 and 4)**

632

633 The second subduction-collision cycle consists of phase 3, corresponding to a south verging oceanic
634 subduction and lasting between 363.5 and 337 Ma (i.e. Famennian to lower Carboniferous), and the
635 successive post-collisional phase 4, lasting between 337 and 295 Ma. These phases can be related to
636 deformation events D2 and D3 observed in the FMC.

637

638 *5.2.1. Alps*

639 *Helvetic domain* – Estimated P-T values characterised by high P/T ratios (Fig. 12a), as Hv11 in
640 Aiguilles Rouge, shows a good agreement both with continental markers scraped from the upper
641 plate and subducted at the beginning of phase 3 (Figs. 11a and 15a) and with subducted continental
642 markers of the lower plate after the continental collision (Figs. 11a and 15c). At the end of phase 3,
643 the same fitting is shown also by Hv2, from Lake Frisson in Argentera, which is characterised by

Journal Pre-proof

644 similar P-T conditions. However, neither Hv11 nor Hv2 fits only with markers involved in the
645 second oceanic subduction. Similarly, data Hv3 from Belledonne and Hv12 from Aiguilles Rouge,
646 that are characterised by intermediate-to-high P/T ratios, show a continuous fitting from the
647 beginning of phase 3 (compatibly with their estimated ages, in Fig. 11a) with continental markers in
648 the shallow portion of the wedge of the second active oceanic subduction (Fig. 15a–c). Differently,
649 Hv6 from Pelvoux is characterised by a re-equilibration under an intermediate-to-high P/T ratio and
650 temperature above 730 °C (Fig. 12a): at the beginning of phase 3 thermal conditions and lithologic
651 affinities allow the fitting both with subducted markers in the shallow portion of the wedge related
652 to slab 2 and with markers at a depth of approximately 50 km belonging to slab 1 (Fig. 15a).
653 Successively, the temperature in the slab 2 decreases while it gradually increases in the slab 1;
654 consequently, Hv6 from Pelvoux does not fit anymore with markers of slab 2 while it fits with
655 shallower markers in slab 1 (Fig. 15b). Proceeding with the evolution of phase 3 and during phase 4,
656 Hv6 fits gradually with a larger amount of markers (Fig. 11a) belonging to markers nearby the
657 doubled crust in correspondence of both slabs (Fig. 15c–e). Moreover, Hv4 from Belledonne has
658 intermediate P/T ratio and fits with markers at the bottom of the continental crust of all plates for
659 the all duration of phase 3 and 4 (Figs. 11a and 15a–e). Data Hv3b, Hv4b and Hv4c from
660 Belledonne are characterised by intermediate P/T ratios and fit with the model at the end of phase 3
661 and at the beginning of phase 4, therefore during the early phases of the continental collision, with
662 continental markers in the proximity of the subduction complex. This is in agreement with the
663 geodynamics reconstruction proposed by Fréville et al. (2018). Lastly, data Hv5 and Hv8 from
664 Pelvoux have low-to-intermediate P/T ratios (Fig. 12a), therefore, they only fit in correspondence of
665 the doubled crust related to the first subduction that, at the end of phase 4, is completely thermally
666 re-equilibrated (Fig. 14d and e).

667

668 *Penninic domain* – Rocks from Gran Paradiso (Pv2 and Pv3), Monte Rosa (Pv4) and Grand St.
669 Bernard (Pv5, Pv6 and Pv7) reveal conditions indicating intermediate P/T ratios, with temperatures

670 below 730 °C, and their fit with the model predictions is uninterrupted during both phase 3 and 4,
671 coherently with their estimated ages (Fig. 11a). In particular, during the first half of phase 3 they
672 show fit with continental markers at the bottom of both plates and in the shallowest portion of the
673 wedge related to the second subduction (Fig. 15a and b), while during the last stages of phase 3 and
674 whole phase 4, they show fit with markers from the continental crust of all the three plates (Fig. 15d
675 and e). Datum Pv8 from the Adula nappe is the only one characterised by a high P/T ratio (Fig. 12b)
676 that finds correspondences with subducted markers of both slabs at the beginning of phase 3, when
677 the system is not still completely thermally re-equilibrated (Fig. 15a). Proceeding with the evolution
678 the first slab warms up and metamorphic conditions characterised by high P/T ratios, such as those
679 of Adula and Suretta (Pv8 and Pv10) are in agreement only with those predicted for subducted and
680 recycled markers in the second slab (Fig. 15b). At the collision, P-T values from rocks re-
681 equilibrated under high P/T ratio (Pv9 and Pv10 from Adula and Suretta) accomplish the agreement
682 only with markers belonging to the deeper portion of the subducted lower plate (Fig. 15c), while
683 during last stages of phase 4 the agreement is with the thermal state of the recycled continental
684 markers in the shallower portion of the wedge, after the thermal re-equilibration (Fig. 15d and e).

685
686 *Austroalpine domain* – Datum Av10 from Mortirolo is characterised by intermediate P/T ratio (Fig.
687 12c) and at the beginning of phase 3 fits only with shallow continental markers in the warmer
688 portion of the hydrated wedge related to the second subduction (Fig. 15a). Proceeding with the
689 evolution, the temperature in the wedge decreases while it increases in correspondence of the
690 doubled crust of the first slab; consequently, Av10 cease to fit with continental markers nearby the
691 second slab and begins to fit with thermally re-equilibrated markers of the first subduction (Fig. 15c
692 and d). Variscan metamorphic rocks from the Dent Blanche nappe in the Austroalpine domain (data
693 Av11 and Av12) reveal conditions marked by an intermediate P/T ratio (Fig. 12c) with an estimated
694 age that correspond to the last stages of evolution of phase 4 (Fig. 11a) and they show fit with
695 continental markers of the upper plate nearby slab 1 and slab 2, respectively (Fig. 15e). Data Av2

696 and Av3 from the Oetztal and Av4 from the Tonale Zone are characterised by high P/T ratios (Fig.
697 12c). Av4 is in good agreement with conditions predicted for markers in the external portion of the
698 second slab at the beginning of phase 3 (Fig. 15a) and in the deep portion of the doubled crust
699 during the first half of phase 3 (Fig. 15a and b). Differently, data Av2 and Av3 fit only with
700 subducted markers of the second slab during the first half of phase 3, compatibly with their
701 pressures (Fig. 15b).

702

703 *Southalpine domain* – All rocks from the Southalpine domain, with the exception of Sv10 (Fig.
704 12d), reveal conditions indicating intermediate P/T ratios, with temperatures below 730 °C. Their fit
705 with the model predictions is continuous during both phase 3 and 4, compatibly with their estimated
706 ages (Fig. 11a). In particular, during the first half of phase 3 they fit with continental markers at the
707 bottom of both plates (Fig. 15a and b), while during the last stages of phase 3 and whole phase 4,
708 they show fit with markers at the bottom of the continental crust of all the three plates (Fig. 15c–e).
709 Datum Sv10 from Tre Valli Bresciane is characterised by high P/T ratio (Fig. 12d) and an estimated
710 age compatible with the first half of phase 3 (Fig. 11a), showing compatibility only with subducted
711 and recycled markers in the second slab (Fig. 15b).

712

713 5.2.2 French Massif Central

714 *Upper Gneiss Unit* – Rocks from Artense (Ar1), Maclas (Mc1), Rouergue (Ro1 and Ro3) are
715 characterised by P-T conditions that reveal intermediate-to-high and high P/T ratios (Fig. 12e) and
716 they fit with subducted and recycled crustal markers in the course of the second subduction only
717 during the early stages of phase 3 (Figs. 11b and 16a, b). Moreover, Ro3 fits also both in
718 correspondence of the deep portion of the doubled crust related to the first subduction during phases
719 3 and 4 (Fig. 16a–e), and in the subducted portion of the continental crust of the lower plate during
720 phase 4 (Fig. 16c–e). Going on with the subduction, the temperature in the slab and in the wedge
721 decreases and no rocks show fit with recycled markers in the mantle wedge related to slab 2. This is

722 due to the higher temperatures characterising estimated P-T conditions from rocks of the FMC with
723 respect to those from the Alps. On the other hand, the temperature in the doubled crust of the first
724 slab increases gradually and data characterised by intermediate P/T ratios Mont du Lyonnais (ML3)
725 fits at the bottom of the continental crust of the upper plate and in correspondence of the doubled
726 crust related to the first slab (Fig. 16b).

727

728 *Lower Gneiss Unit* – Ar2 from Artense is characterised by an intermediate P/T ratio (Fig. 12e) and
729 finds fitting at the bottom of the continental crust of the upper plate during phase 3 before the
730 beginning of the continental collision (Fig. 16a and b), while after the collision (Fig. 16c–e) it
731 shows fit at the bottom of the crust of the lower plate in correspondence of the second subduction
732 and with the doubled thermally re-equilibrated crust related to the first subduction. Differently, data
733 Li3 from Limousin and VD1 from the Velay Dome are characterised by low-to-intermediate P/T
734 ratios (Fig. 12e) and do not show any fitting with the predictions of the model (Fig. 11b). This is
735 because the model does not predict a sufficient increase of the temperatures at shallow depths
736 following the continental collision.

737

738 *Para-autochthonous Unit, Montagne Noire and Thiviers-Payzac Unit* - Estimates with intermediate
739 P/T ratios, such as TP1 from the Thiviers-Payzac unit, PA2 from Plateau d'Aigurande, VD2 from
740 the Velay Dome and MN2 from Montagne Noire (Fig. 12e), show correspondences with the
741 thermal state predicted for continental markers of the upper plate during phase 3 (Fig. 16a and b).
742 Moreover, VD2 fits with continuity in the continental crust of all the three plates for the entire
743 duration of phases 3 and 4 (Fig. 16a–e). MN1 from the Montagne Noire is characterised by a high
744 P/T ratio (Fig. 12e) and does not find thermal and lithologic correspondences with the model.

745

746 **5.3. Single subduction model**

747

748 5.3.1. Alps

749 *Helvetic domain* – Data of the Helvetic domain show a worsening of the agreement with P-T
750 predictions of model SS.5 with respect to model DS.2.5. In particular, data with estimated ages
751 compatible with phase 1, continental affinities and temperatures above 650 °C, such as Pv6 and Pv7
752 from Pelvoux and Pv11 from Aiguilles Rouges (Fig. 17a), worsen their fit, because of the lower
753 temperatures predicted in the slab and in the wedge by faster models. During the phase 2 of model
754 SS.5, at approximately 350–365 Ma (beginning of phase 3 of model DS.2.5), data characterised by
755 intermediate-to-high P/T ratios and continental affinities (Fig. 12a), such as Hv3 from Belledonne
756 and Hv11 from Aiguilles Rouges, worsen their agreement (Fig. 17a). This because of the higher
757 thermal state predicted by model SS.5, due to the post-collisional re-equilibration, with respect to
758 the lower thermal state predicted in model DS.2.5, associated to the beginning of the second
759 subduction. In fact, Hv3 and Hv11 show a fitting with DS.2.5 model only in correspondence of slab
760 2 but they do not show agreement with continental markers of slab 1 (Fig. 15a and b). In addition, at
761 approximately 330–340 Ma (end of phase 3 of model DS.2.5) also Hv2 and Hv11 from the
762 Argentera massif and Aiguilles Rouges, respectively, worsen their agreement with respect to model
763 DS.2.5 (Fig. 17a). This occurs because both data are characterised by intermediate-to-high P/T
764 ratios (Fig. 12a) but model SS.5 is almost completely thermally re-equilibrated and markers nearby
765 the subduction complex are characterised by intermediate P/T ratios.

766 Hv8 from Pelvoux is the sole datum that improves its agreement with model predictions during the
767 latest stages of evolution (phase 4 of model DS.2.5) because it is characterised by low P/T ratio, and
768 the longer post-collisional thermal re-equilibration of model SS.5 with respect to model DS.2.5
769 determines higher temperatures in the subduction complex.

770

771 *Penninic domain* – During phase 1, Pv8, from the central part of the Adula nappe, and Pv10, from
772 Suretta, worsen their agreement with P-T predictions of model SS.5 with respect to model DS.2.5
773 (Fig. 17a). Both of them are characterised by high P/T ratios (Fig. 12b), fitting with predictions of

774 model DS.2.5 for continental subducted markers at different depths in the external portion of the
775 hydrated wedge (Fig. 15–d); then the worsening of the agreement is due to the cooling for the
776 higher velocities of subduction. Between 365 and 350 Ma and from 340 Ma to the end of the
777 evolution (beginning and end of phase 3 in model DS.2.5, respectively) Pv9 and Pv10 from the
778 northern part of the Adula nappe and from Suretta, respectively, do not show fit with predictions of
779 model SS.5 (Fig. 17a), differently than model DS.2.5. It occurs because of lack of high P/T ratios
780 predicted by SS.5 model during the last part of the post-collisional phase.

781

782 *Austroalpine domain* – The lower thermal state characterising model SS.5 with respect of model
783 DS.2.5 during phase 1 determines a worsening of the agreement of Av9 from the Languard-Campo
784 nappe (Fig. 17a) that has a high P/T ratio and is characterised by high temperature (Fig. 12c). On
785 the other hand, Av8 from Silvretta improves its agreement, being characterised by high P/T ratio
786 but low temperature (Fig. 12c), so more compatible with the thermal state predicted for higher
787 velocities of subduction. Between 365 and 350 Ma, Av2 and Av3 from Oetztal and Av5 from the
788 Tonale Zone have a worse agreement with respect to model DS.2.5 (Fig. 17a), because they are
789 characterised by high P/T ratios (Fig. 12c), which are not predicted by model SS.5 during the post-
790 collisional phase. Av10 from the Languard-Campo nappe, characterised by intermediate P/T ratio,
791 also worsen its agreement with predictions of model SS.5 (Fig. 17a) approximately 5–10 Myr from
792 the beginning of phase 2. This occurs because its fit with predictions of model DS.2.5 occurs in
793 correspondence of slab 1, which, in the early stage of phase 2, is warmer than for model SS.5.

794

795 *Southalpine domain* – The only PT value that shows differences in the agreement with predictions
796 of model SS.5 and those of model DS.2.5 is Sv10, from Tre Valli Bresciane. Sv10 is characterised
797 by high P/T ratio (Fig. 12d) and its fit worsen at beginning of phase 3 of model DS.2.5, between
798 365 and 350 Ma (Fig. 17a), when the initiation of the second subduction determines a cooling of the
799 subduction system.

800

801 *5.3.2 French Massif Central*

802 *Upper Gneiss Unit* – As for P-T conditions estimated in the different present-day domains of the
803 Alps, those from the FMC show a general worsening in the agreement with predictions of model
804 SS.5 with respect to model DS.2.5. During phase 1, all data characterised by intermediate-to-high
805 and high P/T ratios and temperatures above 650 °C, such as HA1 from Haut Allier, Li2 from
806 Limousin, ML2 from Mont du Lyonnais, Ar1 from Artense, Ro3 from Rouergue and Mc1 from
807 Maclas (Fig. 12e), worsen their agreement with model predictions (Fig. 17b with respect to Fig.
808 11b), because of the lower thermal state characterising slab 1 of model SS.5 with respect to model
809 DS.2.5. In addition, rocks from Maclas (Mc1) and Artense (Ar1) worsen their agreement with
810 model predictions also during the last stages of phase 2 with respect to phase 4 of model DS.2.5. In
811 fact, during phase 4 of model DS.2.5 they fit with continental subducted markers of slab 2 in a
812 portion of the wedge not completely thermally re-equilibrated, while the wedge during last stages of
813 phase 2 of model SS.5 is completely re-equilibrated and only intermediate P/T ratios are predicted.
814 Moreover, Ro3 decreases the number of markers with which has a compatibility (Fig. 17b with
815 respect to Fig. 11b), because in model DS.2.5 it fitted both with continental markers in doubled
816 crust of the first slab (as in model SS.5) and with subducted continental markers of the lower plate
817 related to the second oceanic subduction. Lastly, data ML3 and ML4 from Mont du Lyonnais and
818 Li5 from Limousin, characterised by intermediate P/T ratios, show the same fitting than in model
819 DS.2.5 (Fig. 17b with respect to Fig. 11b), having compatibilities with continental markers at the
820 bottom of the plates, where P-T conditions are not strongly affected by the second active oceanic
821 subduction or by the velocity of subduction.

822

823 *Lower Gneiss Unit, Para-autochthonous Unit, Montagne Noire and Thiviers-Payzac Unit* – All data,
824 with exception for Li4, show intermediate P/T ratios and show the same fitting with respect to
825 model DS.2.5 (Fig. 17b with respect to Fig.11b). All of them, as for data ML3, ML4 and Li5 of the

826 UGU, fit with continuity at the bottom of the continental crust of all plates, as shown for example
827 by the continuous fitting of PA2 from the PAU in the Plateau d'Aigurande throughout phases 1, 2
828 and 3 and of Ar2 from the LGU in the Limousin (Fig. 17b). Datum, Li4 from the LGU in the
829 Limousin has a high P/T ratio but, as seen for data of the UGU, worsens its fit with respect to model
830 DS.2.5 (Fig. 17b with respect to Fig.11b). This behaviour is the same observed for data Av7 of the
831 Austroalpine domain in the Alps and is due to the high estimated temperature for Li4 (650 °C) that
832 is in contrast with the lower thermal state predicted in model SS.5 with respect to model DS.2.5.

833

834 **6 Discussion**

835 Three models of double subduction, identified by a first subduction phase (phase 1) with different
836 prescribed velocities, have been developed to test if a model characterised by two opposite verging
837 subductions may better represent the evolution of the Variscan orogeny with respect to a single
838 subduction. Such approach allowed the analysis of the activation and the evolution of an oceanic
839 subduction in a geodynamic scenario previously perturbed by an early subduction/collision history.

840 A main result is that, during phase 1 of double subduction models, differences in the thermal state
841 inside the slab are influenced by differences in subduction velocities. In particular, a velocity
842 decrease determines a temperature increase due to the lower amount of cold material subducted
843 during the same time span. Then, the temperatures predicted by model DS.1 in the slab and in the
844 mantle wedge result too high to have P-T conditions compatible with the stability field of serpentine.
845 The consequence is that there is no hydration of the mantle wedge and therefore no activation of
846 small-scale convective cells allowing the recycling of subducted material. On the contrary, the
847 subduction velocity does not influence the thermal state of the upper plate.

848 In all models, large scale mantle flows activate during both oceanic subduction phases (phases 1
849 and 3), but during phase 3 it is less intense, due to the occurrence of the first slab constituting a
850 barrier that prevents the large-scale mantle flow to reach the area between the two subducted slabs.

851 The lack of the mantle flow up to the external boundaries of the hydrated area, and the consequent

852 absence of its heat supply, determines a temperature decrease in the mantle wedge and in the slab
853 interior. In particular, in all models slab 2 is colder than slab 1 of model DS.5, in which the first
854 subduction has the same velocity as the second. During the second post-collisional phase there is an
855 increase of the dip angle of both slabs.

856 Considering the polycyclic scenario proposed for the geodynamic evolution generating the Variscan
857 chain, the most appropriate model to compare the predicted thermal evolutions with P-T conditions
858 inferred for Variscan rocks from the Alps and the FMC appears to be model DS.2.5, taking both
859 paleo-geographic and metamorphic evidences into account. In fact, model DS.5 is characterised by
860 a wide ocean involved in the first subduction (2500 km), in contrast with paleo-geographic
861 reconstructions suggesting a maximum oceanic width of 1000 km (e.g., Lardeaux, 2014a). On the
862 other hand, DS.1 model is not accompanied by the hydration of mantle wedge and therefore does
863 not show recycling of subducted material associated with the first subduction. Monocyclic scenarios
864 account for a wide ocean (~2500 km) closing in ~50 Myr (Malavieille, 1993; Tait et al., 1997;
865 Torsvik, 1998; von Raumer et al., 2003; Marotta and Spalla, 2007), so for the comparison with
866 natural P-T estimates we used model SS.5.

867 The comparison with natural data shows a different agreement for rocks from the Alps and from the
868 French Massif Central (Fig. 18). Metamorphic conditions recorded by the rocks with high P/T ratios
869 from the Alps show a good agreement with P-T predicted in both hot and cold subductions, being
870 characterised by both different metamorphic gradients and different estimated ages; some of them,
871 such as Pv12, from the Penninic domain of the Tauern Window, and Av7, from the Silvretta nappe
872 in the Austroalpine domain (see light blue and yellow dots in panels a2 and b2 of Fig. 18), have
873 better correspondences with a hot subduction, such as phase 1 of model DS.2.5, while others, such
874 as Pv8 and Pv10 from the central Adula and the Suretta nappes in the Penninic domain and Av2
875 from the Oetztal in the Austroalpine domain, with a cold subduction, such as phase 1 of model SS.5
876 and phase 3 of model DS.2.5 (see light blue and yellow dots in panels d2, e2 and f2 of Fig. 18).
877 However, the present day distribution of Variscan records in the Alps is affected by Permian-

878 Triassic rifting, Jurassic oceanisation and a successive Alpine subduction and collision events that
879 inhibits the reconstruction of a coherent geographic distribution of data.

880 Differently, data from the French Massif Central with high P/T ratios fit better with P-T predicted in
881 hot subductions. In particular, data Mc1 and Ar1 from the UGU in Maclas and in Artense,
882 respectively, worsen their agreement during both phase 3 of model DS.2.5 and phase 1 of model
883 SS.5, with respect to phase 1 of model DS.2.5 (see red dots in panels a1 and b1 of Fig. 18).
884 Moreover, data HA1, Li2, PA1, LB1, Ro3 and ML2 from the UGU and Li4 from the LGU worsen
885 their agreement during phase 1 of model SS.5 with respect to model DS.2.5. This suggests that
886 either a hotter subduction is necessary to develop P-T conditions compatible with these data or that
887 the amount and accuracy of the available radiometric data are insufficient to propose a comparison
888 between natural geological data and model predictions. In addition, we must say that some P-T
889 estimates of the FMC of the early works should be refined with new methods of petrologic
890 modeling to be more significant in the comparison with the models. On the other hand, it would be
891 beneficial to determine the uncertainty of the models in order to reduce the ambiguity between
892 different geodynamics settings (e.g. following the procedure proposed by Barzaghi et al., 2014;
893 Marotta et al. 2015; Splendore et al., 2015).

894 The agreement of data characterised by intermediate P/T ratios is slightly influenced by the
895 activation of the second subduction. This because they are compatible with P-T conditions predicted
896 by the models at the bottom of the continental crust of the plates, where the second subduction does
897 not have a significant impact on the thermal state. Therefore, only data characterised by high P/T
898 ratios that have estimated ages compatible with phases 3 and 4 of model DS.2.5 are valid to
899 discriminate between mono- and polycyclic scenarios.

900 Data with high P/T ratios from the Alps show a general improvement in their agreement with
901 phases 3 and 4 of model DS.2.5 with respect to phase 2 of model SS.5. In particular, data Hv3 from
902 Belledonne and Hv11 from Aiguilles Rouge in the Helvetic domain are characterised by
903 intermediate-to-high P/T ratios and fit with continental markers in the shallow portion of the wedge

904 related to the second subduction (see red dots in panels d2, e2 and f2 of Fig. 18); in addition, Pv10
905 from the Suretta nappe in the Penninic domain has a high P/T ratio and improve its agreement
906 fitting with subducted markers in the deep portion of the second slab (see light blue dots in panels
907 d2, e2 and f2 of Fig. 18). However, all these data have not precise geological ages, fitting with
908 model D.2.5 from phase 1 to phase 4, and, consequently, they are not significant for the
909 discrimination among the possible geodynamic scenarios. Similarly, datum Av3 from Oetztal in the
910 Austroalpine domain is characterised by a high P/T ratio and improve its agreement during phase 3
911 of model DS.2.5 fitting in the shallow portion of the wedge of the second subduction (see yellow
912 dots in panels d2 and e2 of Fig. 18). This datum has an estimated age with a narrower range and,
913 therefore, is more significant than the previous data, even if it is a geological and not a radiometric
914 age. Data Pv9 from the Adula nappe in the Penninic domain and Sv10 from Tre Valli Bresciane in
915 the Southalpine domain have high P/T ratios and show a good improvement in model DS.2.5 during
916 phases 3 and 4, fitting with subducted markers related to the second subduction (see blue dots in
917 panels d2, e2 and f2 of Fig. 18). Their radiometric-measured ages make them more significant than
918 the previous, suggesting that a polycyclic scenario is more appropriate for the geodynamic
919 reconstruction of the Variscan orogeny. In general, the fitting improvement between predictions of
920 model DS.2.5 and data from the Alps with an estimated age compatible with the beginning of phase
921 2 of model SS.5 and phases 3 and 4 of model DS.2.5 is related to the activation of the second
922 subduction that produces a lower thermal state, more compatible with data characterised by
923 intermediate-to-high and high P/T ratios. On the other hand, data Hv8 from Pelvoux in the Helvetic
924 domain and Av10 from Mortirolo in the Austroalpine domain worsen the agreement in model
925 DS.2.5, because a completely thermally re-equilibrated model better fit with data characterised by
926 low-to-intermediate P/T ratios, such is the case in model SS.5 at the end of the evolution.

927 Few data from the FMC can help to discriminate among mono- and polycyclic scenarios. In
928 particular, data Mc1 and Ar1 from the UGU in Maclas and in Artense are characterised by high P/T
929 ratios and are the unique to show differences in the fit during phases 3 and 4 of model DS.2.5 with

930 respect to phase 2 of model SS.5, having ages compatible with recycled markers in the wedge
931 related to the second subduction (see red dots in panels d1, e1 and f1 of Fig. 18). However, both of
932 them have not precise geological estimated ages, ranging between 295 and 425 Ma, and, therefore,
933 they are not significant for geodynamic reconstructions of the Variscan orogeny. On the other hand,
934 data with more accurate calculated ages compatible with phases 3 and 4 of model DS.2.5 neither fit
935 nor show differences in the fit with the models. In particular, data with a complete agreement with
936 both models (ML3 from the UGU in Mont du Lyonnais and VD2 and PA2 from the PAU in the
937 Velay Dome and in the Plateau d'Aigurande, respectively) are characterised by intermediate P/T
938 ratios and are compatible with P-T conditions at the bottom of the whole continental crust. The lack
939 of data with high P/T ratios from the FMC in continuous agreement with the slab of the second
940 subduction during phase 3 is in contrast with the good agreement during phase 1. In particular, data
941 from the UGU, such as HA1 from Haut Allier, Li2 from Limousin, PA1 from Plateau d'Aigurande,
942 LB1 from La Bessenois and ML2 from Mont du Lyonnais, and from the LGU, such as Li4 from
943 Limousin, have precise estimated ages and have a good fit during phase 1 with subducted and
944 recycled markers of the first slab (see red dots in panels a1 and b1 of Fig. 18). This behaviour is in
945 agreement with the geographic distribution of the data, because evidences of HP metamorphism
946 related to the second subduction should be located further north than the FMC (see the Eo-Variscan
947 suture in Fig. 18). In particular the suture lies either in the NW part of the Armorican Massif (Léon
948 block) or in the Channel (Faure et al., 2005; Ballèvre et al., 2009; Faure et al., 2010), and, to the
949 east, between North Vosges and Ardennes (Faure et al., 2010; Edel et al., 2018). Data from
950 Montagne Noire must be discussed separately. Datum MN2 from Montagne Noire has an
951 intermediate P/T ratio and fits well during phase 4 with continental markers of upper plate (see
952 orange dots in panel f1 of Fig. 18), then it could be related to D3 event developed in an
953 intracontinental post-collisional setting. On the other hand datum MN1 is characterised by a high
954 P/T ratio and it does not fit with our model. However, it can not be considered indicative because
955 the discussion regarding the interpretation of the HP imprint is still open. Our results clearly

956 highlight the fact that, nowadays, our understanding of Variscan orogeny is limited by a crucial lack
957 of chronologic constraints on FMC metamorphic P-T paths.

958 Although the ocean-continent margins in our model do not include an OCT, data belonging to the
959 UGU with accurate proposed ages compatible with the first subduction (HA1 from Haut Allier,
960 ML2 from Mont du Lyonnais, Ro2 from Rouergue and PA1 from Plateau d'Aigurande; see red dots
961 in panels a1, b1 and c1 of Fig. 18) show very good fitting with both continental markers eroded
962 from the upper plate, representing here a magmatic arc developed on continental crust of either the
963 southern margin of Armorica or an unknown and lost microcontinent (Faure et al., 2008; Lardeaux,
964 2014a), and oceanic markers of the lower plate, coupled at the trench and successively subducted
965 and exhumed in the mantle wedge. Consequently, our model shows the possibility that rocks from
966 the UGU could have an origin different from an OCT. This result opens a new perspective on the
967 understanding of the pre-orogenic, Cambro-Ordovician, structural restoration of the FMC. Indeed,
968 taking into account the consequences of thermal modelling presented above, in the FMC, as it is the
969 case for more than two decades in the Alps (see discussions in Platt, 1986; Polino et al., 1990;
970 Spalla et al., 1996; Schmid et al., 2004; Rosenbaum and Lister, 2005; Stöckhert and Gerya, 2005;
971 Beltrando et al., 2010; Roda et al., 2012; Lardeaux, 2014b), the origin of high-pressure
972 metamorphic rocks can be described in the framework of two significantly contrasted conceptual
973 geodynamic models: (i) these rocks derive from a subducted OCT, thus from the lower plate, or (ii)
974 they derive, at least in part, from the upper plate as the result of mass-transfers during ablative
975 subduction.

976

977 **7 Conclusions**

978

979 We have investigated the thermo-mechanics of an oceanic subduction complex in a system
980 perturbed by a previous ocean-continent subduction. Results from models of double subduction
981 indicate that:

982 (1) there is a correlation between the thermal state of both the slab and the mantle wedge
983 and the velocity of subduction; in particular lower temperatures can be observed for higher
984 velocities of subduction. On the other hand, the velocity of subduction does not have a
985 significant impact on the thermal state of the upper plate;

986 (2) high temperatures observed in the slowest model prevent the hydration of the mantle
987 wedge, with a consequent lack of recycling of subducted material deriving both from the
988 lower plate and from the continental margin of the upper plate;

989 (3) for same subduction velocities, the second subduction complex is colder than the first,
990 due to the lack of large-scale mantle flow with the consequent heat supply.

991 From the successive comparison between thermal model predictions and natural Variscan P-T-t
992 estimates from the Alps and the FMC results that:

993 (1) data from the Alps with high P/T ratios fit well with both hot and cold subductions,
994 while data from the FMC with high P/T ratios have a better compatibility with hot
995 subductions;

996 (2) some data from the Alps with high P/T ratios and accurate radiometric ages, compatible
997 with a younger (Famennian to lower Carboniferous) subduction event, show a better fit
998 with the double subduction model, suggesting that a polycyclic scenario is more suitable for
999 the Variscan orogeny;

1000 (3) the data of the FMC with high P/T ratios that show different fit in single and double
1001 subduction models have poorly constrained geological ages and, therefore, are not suitable
1002 to discriminate between mono- and polycyclic scenarios. This reflects also the fact that the
1003 high-pressure metamorphic rocks compatible with a Famennian to lower Carboniferous
1004 subduction event are located north of the FMC (e.g. in the NW part of the Armorican
1005 Massif Léon or even more likely in the Channel);

1006 (4) considering the FMC, the compatibility of the model with data from the UGU open to
1007 the possibility that rocks of this unit could derive from tectonic erosion of the upper plate
1008 and not only from a lower plate OCT.

1009

1010 **Acknowledgements**

1011 This work was partially supported by the MIUR-PRIN 2011 project (2010AZR98L) ‘Birth and
1012 death of oceanic basins: geodynamic processes from rifting to continental collision in
1013 Mediterranean and Circum-Mediterranean orogens’ and by the SISMA-Pilot Project ‘SISMA-
1014 Information System for Monitoring and Alert’ (ASI contract No. I/093/06/0). All of the figures
1015 were created using the Generic Mapping Tool (GMT) plotting software (Wessel and Smith, 1998).
1016 We thank the Editor Yoshida Masaki, Michel Faure and an anonymous reviewer for providing
1017 useful suggestions.

1018

1019 **References**

- 1020 Afonso, J. C., Ranalli, G., 2004. Crustal and mantle strengths in continental lithosphere: is the jelly
1021 sandwich model obsolete? *Tectonophysics* 394, 221–232.
- 1022 Arcay, D., Tric, E., Doin, M. P., 2005. Numerical simulation of subduction zones. Effect of slab
1023 dehydration on the mantle wedge dynamics. *Physics of the Earth and Planetary Interiors* 149,
1024 133–153.
- 1025 Baes, M., Sobolev, S. V., 2017. Mantle flow as a trigger for subduction initiation: a missing
1026 element of the Wilson Cycle concept. *Geochemistry, Geophysics, Geosystems*, DOI
1027 10.1002/2017GC006962.
- 1028 Ballèvre, M., Bosse, V., Ducassou, C., Pitra, P., 2009. Palaeozoic history of the Armorican Massif:
1029 Models for the tectonic evolution of the suture zones. *Tectonics* 341, 174-201.

- Journal Pre-proof
- 1030 Barbey, P., Villaros, A., Marignac, C., Montel, J.-M., 2015. Multiphase melting, magma
1031 emplacement and P-T-time path in late-collisional context: the Velay example (Massif Central,
1032 France). *Bulletin de la Societe Géologique de France* 186(2-3), 93–116.
- 1033 Bard, J.-P., Burg, J.-P., Matte, P., Ribeiro, A., 1980. La chaîne hercynienne d'Europe occidentale en
1034 termes de tectonique des plaques. *Mem. B.R.G.M.* 108, 233–246.
- 1035 Barzagli, R., Marotta, A.M., Splendore, R., De Gaetani, C., Borghi, A., 2014. Statistical assessment
1036 of predictive modelling uncertainty: a geophysical case study. *Geophysical Journal*
1037 *International* 127, 22-32.
- 1038 Bellot, J. P., Roig, J. Y., 2007. Episodic exhumation of HP rocks inferred from structural data and
1039 P-T paths from the southwestern Massif Central (Variscan belt, France). *Journal of Structural*
1040 *Geology* 29(9), 1538–1557.
- 1041 Beltrando, M., Compagnoni, R., Lombardo, B., 2010. (Ultra-) High-pressure metamorphism and
1042 orogenesis: An Alpine perspective. *Gondwana Research* 18, 147-166.
- 1043 Benciolini, L., Poli, M. M. E., Visonà, D., Zanferrari, A., 2006. Looking inside late Variscan
1044 tectonics: structural and metamorphic heterogeneity of the Eastern Southalpine basement (NE
1045 Italy). *Geodinamica Acta* 19(1), 17–32.
- 1046 Berger, J., Féménias, O., Mercier, J.-C. C., Demaiffe, D. 2005. Ocean-floor hydrothermal
1047 metamorphism in the Limousin ophiolites (western French Massif Central): evidence of a rare
1048 preserved Variscan oceanic marker. *Journal of Metamorphic Geology* 23, 795–812.
- 1049 Berger, A., Féménias, O., Ohnenstetter, D., Bruguier, O., Plissart, G., Mercier, J.-C. C., Demaiffe,
1050 D., 2010. New occurrence of UHP eclogites in Limousin (French Massif Central): Age,
1051 tectonic setting and fluid–rock interactions. *Lithos* 118, 365-382.
- 1052 Bergomi, M. A., Dal Piaz, G. V., Malusà, M. G., Monopoli, B., Tunesi, A., 2017. The Grand St
1053 Bernard - Briançonnais nappe system and the Paleozoic inheritance of the Western Alps
1054 unravelled by zircon U-Pb dating. *Tectonics* 36, 2950-2972.

- Journal Pre-proof
- 1055 Bertotti, G., Siletto, G. B., Spalla, M. I., 1993. Deformation and metamorphism associated with
1056 crustal rifting: Permian to Liassic evolution of the Lake Lugano-Lake Como area (southern
1057 Alps). *Tectonophysics* 226, 271–284.
- 1058 Best, M. G., Christiansen, E. H., 2001. *Igneous Petrology*, Blackwell Science, Oxford, 455 pp.
- 1059 Bogdanoff, S., Ménot, R., Vivier, G., 1991. Les massif cristallins externes des Alpes occidentales
1060 françaises, un fragment de la zone interne varisque. *Science Géologique Bulletin* 44, 237–
1061 285.
- 1062 Bonin, B., Brändlein, P., Bussy, F., Desmons, J., Eggenberger, U., Finger, F., Graf, K., Marro, C.,
1063 Mercolli, I., Oberhänsli, R., Ploquin, A., von Quadt, A., von Raumer, J., Schaltegger, U.,
1064 Steyrer, H. P., Visonà, D., Vivier, G., 1993. Late Variscan magmatic evolution of the Alpine
1065 basement. In: Von Rumer, J. F., Neubauer, F. (eds.), *Pre-Alpine Basement in the Alps*.
1066 Springer-Verlag, Heidelberg, pp. 171-201.
- 1067 Borghi, A., 1989. L'evoluzione metamorfico-strutturale del settore nord-orientale della Serie dei
1068 Laghi (Alpi Meridionali). PhD thesis, Università di Torino.
- 1069 Borghi, A. 1991. Structural evolution of the north-eastern sector of the Serie dei Laghi (Southern
1070 Alps). *Bollettino della Società Geologica Italiana* 110, 639– 647.
- 1071 Borghi, A., Gattiglio, M., Mondino, F., Zaccone, G., 1999. Structural and metamorphic evidence of
1072 pre-Alpine basement in the Ambin nappe (Cottian Alps, Italy). *Memorie della Società*
1073 *Geologica Italiana* 51(1), 205–220.
- 1074 Boriani, A., Burlini, L., Sacchi, R. 1990. The Cossato-Mergozzo-Brissago line and the Pogallo line
1075 (Southern Alps, Northern Italy) and their relationships with late-Hercynian magmatic and
1076 metamorphic events. *Tectonophysics* 140, 193–212.
- 1077 Boriani, A., Villa, I., 1997. Geochronology of regional metamorphism in the Ivrea-Verbano zone
1078 and Serie dei Laghi, Italian Alps. *Schweizerische Mineralogische Und Petrographische*
1079 *Mitteilungen* 77, 381–401.

- Journal Pre-proof
- 1080 Boutin, R., Montigny, R., 1993. Datation $^{39}\text{Ar}/^{40}\text{Ar}$ des amphibolites du complexe leptyno-
1081 amphibolique du plateau d'Aigurande: collision varisque à 390 Ma dans le Nord-Ouest du
1082 Massif central français. *Compte Rendu Academie des Sciences de Paris* 316, 1391–1398.
- 1083 Brodie, K. H., Rex, D., Rutter, E. H., 1989. On the age of deep crustal extensional faulting in the
1084 Ivrea zone, Northern Italy. In: Coward, M. P., Dietrich, D., Park, R. G. (eds.), *Alpine*
1085 *Tectonics*. Geological Society, London, Special Publications, vol. 45, pp. 203-210.
- 1086 Burg, J. P., Delor, C., Leyreloup, A., 1986. Le massif du Lévézou et les séries adjacentes du
1087 Rouergue Oriental. Nouvelles données pétrographiques et structurales. *Bulletin du Bureau de*
1088 *Recherche Géologiques et Minières Série 2: Geologie de la France* 3, 229-272.
- 1089 Burg, J. P., Delor, C. P., Leyreloup, A. F., Romney, F., 1989. Inverted metamorphic zonation and
1090 Variscan thrust tectonics in the Rouergue area (Massif Central, France): P-T-t record from
1091 mineral to regional scale. In: Daly, J. S., Cliff, R. A., Yardley, B. W. D. (eds.), *Evolution of*
1092 *Metamorphic Belts*. Geological Society, London, Special Publication, vol. 43, pp. 423-439.
- 1093 Burg, J.-P., Matte, P., 1978. A cross-section through the french Massif central and the scope of its
1094 Variscan geodynamic evolution. *Z. Dtsch. Geol. Ges.* 129, 429–460.
- 1095 Bussy, F., Sartori, M., Thélin, P., 1996. U-Pb zircon dating in the middle Penninic basement of the
1096 Western Alps (Valais, Switzerland). *Schweizerische Mineralogische Und Petrographische*
1097 *Mitteilungen* 76, 81–84.
- 1098 Carminati, E., Siletto, G. B., Battaglia, D., 1997. Thrust kinematics and internal deformation in
1099 basement-involved fold and thrust belts: The eastern Orobic Alps case (Central Southern Alps,
1100 northern Italy). *Tectonics* 16(2), 259-271.
- 1101 Cassinis, G., Massari, F., Neri, C., Venturini, C., 1988. The continental Permian in the southern alps
1102 (Italy) - a review. *Zeitschrift fur geologische Wissenschaften* 16, 1117-1126.
- 1103 Catalàn, J. R. M., 2011. Are the oroclines of the Variscan belt related to late Variscan strike-slip
1104 tectonics? *Terra Nova* 23, 241-247.

- Journal Pre-proof
- 1105 Cavazza, W., Wezel, F. C., 2003. The Mediterranean region - a geological primer. *Episodes* 26(3),
1106 160-168.
- 1107 Chenevoy, M., 1970. Carte Géologique de la France à 1/50.000, feuille de St Etienne. BRGM,
1108 Orléans.
- 1109 Chopra, P. N., Peterson, M. S., 1981. The experimental deformation of dunite. *Tectonophysics* 78,
1110 453–473.
- 1111 Christensen, U. R., 1992. An Eulerian technique for thermo-mechanical model of lithospheric
1112 extension. *Journal of Geophysical Research* 97, 2015-2036.
- 1113 Christensen, U. R., Yuen, D. A., 1985. Layered Convection Induced by Phase Transitions. *Journal*
1114 *of Geophysical Research* 90(B12), 10291-10300.
- 1115 Cizkova, H, Bina, C.R., 2015. Geodynamics of trench advance: Insights from a Philippine-Sea-style
1116 geometry. *Earth and Planetary Science Letters* 430, 408–415.
- 1117 Cocks, L. R. M., Torsvik, T. H., 2011. The Palaeozoic geography of Laurentia and western
1118 Laurussia: A stable craton with mobile margins. *Earth-Science Reviews* 106, 1-51.
- 1119 Compagnoni, R., Ferrando, S., 2010. Paleo-European crust of the Italian western Alps: Geological
1120 history of the Argentera Massif and comparison with Mont Blanc–Aiguilles Rouges and
1121 Maures. *Journal of the Virtual Explorer Electronic Edition* 36(3), 1-32.
- 1122 Costa, S., 1990. De la collision continentale à l'extension tardiorogénique: 100 millions d'années
1123 d'histoire varisque dans le Massif Central Français: Une étude chronologique par la méthode
1124 $^{40}\text{Ar}/^{39}\text{Ar}$. Ph.D. Thesis, Univ. Montpellier, 441 p.
- 1125 Costa, S., Maluski, H., Lardeaux, J.-M., 1993. $^{40}\text{Ar}/^{39}\text{Ar}$ chronology of Variscan tectono-
1126 metamorphic events in an exhumed crustal nappe: the Monts du Lyonnais complex (Massif
1127 Central, France). *Chemical Geology* 105(4), 339–359.
- 1128 Dai, L., Li, S., Li, Z.-H., Somerville, I., Suo, Y., Liu, X., Gerya, T.V., Santosh, M., 2018. Dynamics
1129 of exhumation and deformation of HP-UHP orogens in double subduction-collision systems:

- Journal Pre-proof
- 1130 Numerical modeling and implications for the Western Dabie Orogen. *Earth-Science Reviews*
1131 182, 68–84.
- 1132 Dal Piaz, G. V., 2010. Geological outline of the Alps, focusing on the Italian north-western side. In:
1133 Beltrando, M., Peccerillo, A., Mattei, M., Conticelli, S., Doglioni, C. (eds.), *The Geology of*
1134 *Italy: tectonics and life along plate margins. Journal of the Virtual Explorer Electronic Edition,*
1135 *vol. 36(8), pp. 1-28.*
- 1136 Dal Piaz, G. V., Bistacchi, A., Massironi, M., 2003. Geological outline of the Alps. *Episodes* 26(3),
1137 175-180.
- 1138 Dale, J., Holland, T. J. B., 2003. Geothermobarometry, P-T paths and metamorphic field gradients
1139 of high-pressure rocks from the Adula Nappe, Central Alps. *Journal of Metamorphic Geology*
1140 21(8), 813–829.
- 1141 Delleani, F., Rebay, G., Zucali, M., Tiepolo, M., Spalla, M. I., 2018. Insights on Variscan
1142 geodynamics from the structural and geochemical characterization of a Devonian-
1143 Carboniferous gabbro from the Austroalpine domain (Western Alps). *Ofioliti* 43(1), 23-39.
- 1144 Delor, C., Burg, J.P., Guiraud, M., Leyreloup, A., 1987. Les métapélites à phengite-chloritoïde-
1145 grenat-staurotide-disthène de la klippe de Najac-Carmaux: nouveaux marqueurs d'un
1146 métamorphisme de haute pression varisque en Rouergue occidentale. *Comptes Rendus de*
1147 *l'Académie des Sciences* 305, 589–595.
- 1148 Demange, M., 1985. The eclogite-facies rocks of the Montagne Noire, France. *Chemical Geology*
1149 50(1-3), 173-188.
- 1150 Desmons, J., Compagnoni, R., Cortesogno, L., Frey, M., Gaggero, L., 1999. Pre-Alpine
1151 metamorphism of the Internal zones of the Western Alps. *Schweizerische Mineralogische*
1152 *Und Petrographische Mitteilungen* 79, 23-39.
- 1153 Desmons, J., and D. Mercier, 1993. Passing Through the Briançon Zone. In: von Raumer, J. F.,
1154 Neubauer, F. (eds.), *Pre-Mesozoic Geology in the Alps. Springer-Verlag, Heidelberg, pp.*
1155 *279–296.*

- 1156 di Paola, S., 2001. Eredità litostratigrafica, strutturale e metamorfica paleozoica nel margine interno
1157 Europeo (Grandes Rousses e Argentera), ristrutturato durante l'orogenesi Alpina. Ph.D.
1158 Thesis, Università degli Studi di Milano and Université Claude Bernard Lyon.
- 1159 di Paola, S., Spalla, M. I., 2000. Contrasting tectonic records in pre-Alpine metabasites of the
1160 Southern Alps (lake Como, Italy). *Journal of Geodynamics* 30(1-2), 167–189.
- 1161 di Paola, S., Spalla, M. I., Gosso, G. 2001. New structural mapping and metamorphic evolution of
1162 the Domaso-Cortafò Zone (Southern Alps - Lake Como). *Memorie di Scienze Geologiche* 53,
1163 1– 14.
- 1164 Diella, V., Spalla, M. I., Tunesi, A., 1992. Contrasted thermo-mechanical evolutions in the South-
1165 alpine metamorphic basement of the Orobic Alps (Central Alps, Italy). *Journal of*
1166 *Metamorphic Geology* 10, 203–219.
- 1167 Droop, G. T. R., 1983. Pre-Alpine eclogites in the Pennine Basement Complex of the Eastern Alps.
1168 *Journal of Metamorphic Geology* 1(1), 3–12.
- 1169 Droop, G. T. R., Lombardo, B., Pognante, U., 1990. Formation and distribution of eclogite facies
1170 rocks in the Alps. In: Carswell, D. A. (ed.), *Eclogite Facies Rocks*. Blackie and Son Ltd,
1171 London, pp. 225-256.
- 1172 Dubois, J., Diament, M., 1997. *Géophysique*, Masson, Paris, 205 pp.
- 1173 Dubuisson, G., Mercier, J.-C. C., Girardeau, J., Frison, J.-Y., 1989. Evidence for a lost ocean in
1174 Variscan terranes of the Western Massif Central, France. *Nature* 337, 729-732.
- 1175 Ducrot, J., Lancelot, J. R., Marchand, J., 1983. Datation U-Pb sur zircons de l'éclogite de La Borie
1176 (Haut-Allier, France) et conséquences sur l'évolution ante-hercynienne de l'Europe
1177 occidentale. *Earth and Planetary Science Letters* 62(3), 385–394.
- 1178 Dufour, E., 1982. *Pétrologie et géochimie des formations ortho-métamorphiques acides des monts*
1179 *du lyonnais (Massif Central français)*. Ph.D. Thesis, Univ. Lyon 1, 241 pp.

- Journal Pre-proof
- 1180 Dufour, E., Lardeaux, J.-M., Coffrant, D., 1985. Eclogites et granulites dans les Monts du
1181 Lyonnais: une évolution métamorphique plurifaciale éohercynienne. *Compte Rendu*
1182 *Academie des Sciences de Paris* 300(4), 141–144.
- 1183 Duguet, M., Le Breton, N., Faure, M., 2007. P–T paths reconstruction of a collisional event: The
1184 example of the Thiviers-Payzac Unit in the Variscan French Massif Central. *Lithos* 98, 210-
1185 232.
- 1186 Duthou, J.L., Chenevoy, M., Gay, M., 1994. Age Rb/Sr Dévonien moyen des migmatites à
1187 cordiérite du Lyonnais (Massif Central français). *Compte Rendu Academie des Sciences de*
1188 *Paris* 319, 791-796.
- 1189 Edel, J. B., Maurer, V., Dalmais, E., Genter, A., Richard, A., Letourneau, O., Hehn, R., 2018.
1190 Structure and nature of the Palaeozoic basement based on magnetic, gravimetric and seismic
1191 investigations in the central Upper Rhinegraben. *Geotherm Energy* 6:13, 1-25.
- 1192 Edel, J. B., Schulmann, K., Skrzypek, E., Cocherie, A., 2013. Tectonic evolution of the European
1193 Variscan belt constrained by palaeomagnetic, structural and anisotropy of magnetic
1194 susceptibility data from the Northern Vosges magmatic arc (eastern France). *Journal of the*
1195 *Geological Society* 170(5), 785-804.
- 1196 Faryad, S. W., Melcher, F., Hoinkes, G., Puhl, J., Meisel, T., Frank, W., 2002. Relics of eclogite
1197 facies metamorphism in the Austroalpine basement, Hochgroessen (Speik complex), Austria.
1198 *Mineralogy and Petrology* 74, 49–73.
- 1199 Faure, M., Bé Mézème, E., Cocherie, A., Rossi, P., Chemenda, A., Boutelier, D., 2008. Devonian
1200 geodynamic evolution of the Variscan Belt, insights from the French Massif Central and
1201 Massif Armoricaïn. *Tectonics* 27, TC2005, 1-19.
- 1202 Faure, M., Bé Mézème, E., Duguet, M., Cartier, C., Talbot, J. Y., 2005. Paleozoic tectonic evolution
1203 of medio-Europa from the example of the French Massif Central and Massif Armoricaïn.
1204 *Journal of the Virtual Explorer* 19(5), 1-26.

- Journal Pre-proof
- 1205 Faure, M., Cocherie, A., Bé Mézème, E., Charles, N., Rossi, P., 2010. Middle Carboniferous crustal
1206 melting in the Variscan Belt: New insights from U–Th–Pb_{tot.} monazite and U–Pb zircon ages
1207 of the Montagne Noire Axial Zone (southern French Massif Central). *Gondwana Research* 18,
1208 653–673.
- 1209 Faure, M., Cocherie, A., Gaché, J., Esnault, C., Guerrot, C., Rossi, P., Wei, L., Qiuli, L., 2014.
1210 Middle Carboniferous intracontinental subduction in the Outer Zone of the Variscan Belt
1211 (Montagne Noire Axial Zone, French Massif Central): multimethod geochronological
1212 approach of polyphase metamorphism. *Geological Society, London, Special Publications*
1213 405(1), 289–311.
- 1214 Faure, M., Lardeaux, J. M., Ledru, P., 2009. A review of the pre-Permian geology of the Variscan
1215 French Massif Central. *Comptes Rendus Geoscience* 341, 202-213.
- 1216 Faure, M., Leloix, C., Roig, J.-Y., 1997. L'Evolution polycyclique de la chaîne hercynienne.
1217 *Bulletin de la Société Géologique de France* 168(6), 695-705.
- 1218 Faure, M., Prost, A. E., Lasne, E., 1990. Déformation ductile extensive d'âge namuro-westphalien
1219 dans le plateau d'Aigurande, Massif central français. *Bulletin de la Societe Geologique de*
1220 *France* 1(8), 189–197.
- 1221 Ferrando, S., Lombardo, B., Compagnoni, R., 2008. Metamorphic history of HP mafic granulites
1222 from the Gesso-Stura Terrain (Argentera Massif, Western Alps, Italy). *Eur. J. Mineral.* 20,
1223 777–790.
- 1224 Feybesse, J.-L., Lardeaux, J.-M., Johan, V., Tegye, M., Dufour, E., Lemièrre, B., Delfour, J., 1988.
1225 La série de la Brévenne (Massif central français): une unité dévonienne charriée sur le
1226 complexe métamorphique des Monts du Lyonnais à la fin de la collision varisque. *Compte*
1227 *Rendu Academie des Sciences de Paris* 307(2), 991–996.
- 1228 Feybesse, J.L., Lardeaux, J.M., Tegye, M., Gardien, V., Peterlongo, J.M., Kerrien, Y., Becq-
1229 Giraudon, J.F., 1996. Carte géologique de France (1/50,000), feuille St-Symphorien sur Coise
1230 (721). BRGM, Orléans.

- Journal Pre-proof
- 1231 Franke, W., 2000. The mid-European segment of the Variscides: tectonostratigraphic units, terrane
1232 boundaries and plate tectonic evolution. Geological Society, London, Special Publications
1233 179(1), 35-61.
- 1234 Franke, W., Cocks, L. R. M., Torsvik, T. H., 2017. The Palaeozoic Variscan oceans revisited.
1235 Gondwana Research 48, 257-284.
- 1236 Fréville, K., Trap, P., Faure, M., Melleton, J., Li, X.H., Lin, W., Blein, O., Bruguier, O., Poujol, M.,
1237 2018. Structural, metamorphic and geochronological insights on the Variscan evolution of the
1238 Alpine basement in the Belledonne Massif (France). Tectonophysics 726, 14-42.
- 1239 Fumasoli, M., 1974. Geologie des Gebietes nördlich und südlich der Jorio-Tonale-Linie im Westen
1240 von Gravedona (Como, Italia). Ph.D. Thesis, Zurich.
- 1241 Gardien, V., 1990. Reliques de grenat et de staurotide dans la série métamorphique de basse
1242 pression du mont Pilat (Massif Central français): témoins d'une évolution tectono-
1243 métamorphique polyphasée. Compte Rendu Academie des Sciences Paris 310(2), 233-240.
- 1244 Gardien, V., Lardeaux, J.-M., 1991. Découverte d'éclogites dans le synforme de Maclas: extension
1245 de l'Unité Supérieure des Gneiss à l'Est du Massif Central. Compte Rendu Academie des
1246 Sciences Paris 312, 61-68.
- 1247 Gardien, V., Lardeaux, J.M., Ledru, P., Allemand, P., Guillot, S., 1997. Metamorphism during late
1248 orogenic extension: insights from the French Variscan belt. Bull. Soc. Géol. France 168(3),
1249 271-286.
- 1250 Gardien, V., Reusser, E., Marquer, D., 1994. Pre-Alpine metamorphic evolution of the gneisses
1251 from the Valpelline series (Western Alps, Italy). Schweizerische Mineralogische Und
1252 Petrographische Mitteilungen 74, 489-502.
- 1253 Gardien, V., Lardeaux, J.-M., Misseri, M., 1988. Les péridotites des Monts du Lyonnais (Massif
1254 Central Français): témoins privilégiés d'une subduction de lithosphère océanique paléozoïque.
1255 Compte Rendu Academie des Sciences de Paris 307, 1967-1972.

- Journal Pre-proof
- 1256 Gasco, I., Borghi, A., Gattiglio, M., 2010. Metamorphic evolution of the Gran Paradiso Massif: A
1257 case study of an eclogitic metagabbro and a polymetamorphic glaucophane–garnet micaschist
1258 *Lithos* 115(1-4), 101–120.
- 1259 Gasco, I., Borghi, A., Gattiglio, M., 2011a. P–T Alpine metamorphic evolution of the Monte Rosa
1260 nappe along the Piedmont Zone boundary (Gressoney Valley, NW Italy). *Lithos* 127(1-2),
1261 336–353.
- 1262 Gay, M., Peterlongo, J.M., Caen-Vachette, M., 1981. Age radio-métrique des granites allongés et en
1263 feuillets minces syntectoniques dans les Monts du Lyonnais (Massif Central français).
1264 *Compte Rendu Academie des Sciences de Paris* 293(2), 993-996.
- 1265 Gébelin, A., Martelet, G., Brunel, M., Faure, M., Rossi, P., 2004. Late Hercynian leucogranites
1266 modelling as deduced from new gravity data: The example of the Millevaches massif (Massif
1267 Central, France). *Bulletin de la Societe Geologique de France* 175(3), 239–248.
- 1268 Gébelin, A., Roger, F., Brunel, M., 2009. Syntectonic crustal melting and high-grade
1269 metamorphism in a transpressional regime, Variscan Massif Central, France. *Tectonophysics*
1270 477(3-4), 229–243.
- 1271 Genier, F., Bussy, F., Epard, J.-L., Baumgartner, L., 2008. Water-assisted migmatization of
1272 metagraywackes in a Variscan shear zone, Aiguilles-Rouges massif, western Alps. *Lithos*
1273 102(3-4), 575–597.
- 1274 Gerya, T. V., Stöckhert, B., 2006. Two-dimensional numerical modeling of tectonic and
1275 metamorphic histories at active continental margins. *Int. J. Earth Sci. (Geol. Rundsch.)* 95(2),
1276 250–274.
- 1277 Gerya, T. V., Yuen, D. A., 2003. Rayleigh-Taylor instabilities from hydration and melting propel
1278 ‘cold plumes’ at subduction zones. *Earth planet. Sci. Lett.* 212, 47–62.
- 1279 Giacomini, F., Braga, R., Tiepolo, M., Tribuzio, R., 2007. New constraints on the origin and age of
1280 Variscan eclogitic rocks (Ligurian Alps, Italy). *Contributions to Mineralogy and Petrology*
1281 153(1), 29–53.

- Journal Pre-proof
- 1282 Giobbi, M. E., Boriani, A., Villa, I., 2003. Pre-Alpine ophiolites in the basement of Southern Alps:
1283 the presence of a bimodal association (LAG-Leptyno-Amphibolitic group) in the Serie dei
1284 Laghi (N-Italy, Ticino-CH). *Rendiconti Accademia Lincei* 9(14), 79–99.
- 1285 Giobbi, O. E., Gregnanin, A., 1983. The crystalline basement of the “Massiccio delle Tre Valli
1286 Bresciane”: new petrographic and chemical data. *Memorie della Società Geologica Italiana* 26,
1287 133–144.
- 1288 Giorgis, D., Thélin, P., Stampfli, G., Bussy, F., 1999. The Mont-Mort metapelites: Variscan
1289 metamorphism and geodynamic context (Briançonnais basement, Western Alps, Switzerland).
1290 *Schweizerische Mineralogische Und Petrographische Mitteilungen* 79(3), 381-398.
- 1291 Girardeau, J., Dubuisson, G., Mercier, J.-C. C., 1986. Cinématique de la mise en place des ophiolite
1292 et nappes cristallophylliennes du Limousin, Ouest du Massif central français. *Bull. Soc. Géol.*
1293 *France* 8, 849-860.
- 1294 Godard, G., 1990. Découverte d'éclogites, de péridotites à spinelle et d'amphibolites à corindon
1295 dans le Morvan. *Compte Rendu Academie des Sciences de Paris* 310, 227-232.
- 1296 Godard, G., Martin, S., Prosser, G., Kienast, J., Morten, L., 1996. Variscan migmatites, eclogites
1297 and garnet-peridotites of the Ulten zone, Eastern Austroalpine system. *Tectonophysics* 259,
1298 313–341.
- 1299 Gosso, G., Messiga, B., Spalla, M. I., 1995. Dumortierite-kyanite relics within the HT-LP country
1300 rocks of the Sondalo Gabbro: a record of extension related uplift of HP-rocks. *International*
1301 *Ophiolite Symposium, Abstract volume*, 55.
- 1302 Gosso, G., Lardeaux, J. M., Zanoni, D., Volante, S., Corsini, M., Bersezio, R., Mascle, J., Spaggiari,
1303 L., Spalla, M. I., Zucali, M., Giannerini, G., Caméra, L. Progressive versus finite geological
1304 mapping: a key for understanding the geodynamic evolution of the Maritime Alps. *Journal of*
1305 *Maps*, in press.
- 1306 Grandjean, V., Guillot, S., Pecher, A., 1996. Un nouveau témoin de l'évolution métamorphique BP-
1307 HT post-orogénique hercynienne: l'unité de Peyre-Arguet (Haut-Dauphiné): A new record of

Journal Pre-proof

1308 the LP-HT late-Variscan metamorphism: the Peyre-Arguet unit (Haut-Dauphiné). *Comptes*
1309 *Rendus de l'Academie de Sciences - Serie IIA: Sciences de la Terre et des Planetes* 322(3),
1310 189–195.

1311 Guillot, S., di Paola, S., Ménot, R.-P., Ledru, P., Spalla, M. I., Gosso, G., Schwartz, S., 2009.
1312 Suture zones and importance of strike-slip faulting for Variscan geodynamic reconstructions
1313 of the External Crystalline Massifs of the western Alps. *Bulletin de la Societe Geologique de*
1314 *France* 180(6), 483-500.

1315 Guillot, S., Ménot, R. P., 1999. Nappe stacking and first evidence of Late Variscan extension in
1316 the Belledonne Massif (External Crystalline Massifs, French Alps). *Geodinamica Acta* 12(2),
1317 97–111.

1318 Guillot, S., Ménot, R. P., 2009. Paleozoic evolution of the External Crystalline Massif of the
1319 Western Alps. *Tectonics* 34(1), 253-265.

1320 Guillot, S., Ménot, R. P., Fernandez, A., 1998. Paleozoic evolution of the external crystalline
1321 massifs along the Belledonne-Oisans transect (Western Alps). *Acta Universitatis Carolinae*
1322 *Geologica* 42, 257–258.

1323 Haenel, R., Rybach, L., Stegena, L., 1988. *Handbook of Terrestrial Heatflow Density*
1324 *Determination*. Kluwer Academic Publisher, Dordrecht, 486 pp.

1325 Hauzenberger, C. A., Holler, W., Hoinkes, G., 1996. Transition from eclogite to amphibolite-
1326 facies metamorphism in the Austroalpine Ulten Zone. *Mineralogy and Petrology* 58, 111–
1327 130.

1328 Hauzenberger, C. A., Höller, W., Hoinkes, G., Klözli, U., Thöni, M. 1993. Metamorphic
1329 evolution of the Austroalpine basement in Nonsberg area, Ultental (Val d'Ultimo), Southern
1330 Tyrol. *Terra Nova* 5, 13.

1331 Herzberg, C., Riccio, L., Chiesa, A., Fornoni, A., Gatto, G. O., Gregnanin, A., Piccirillo, E. M.,
1332 Scolari, A., 1977. Petrogenetic evolution of a spinelgarnet-lherzolite in the austridic

- Journal Pre-proof
- 1333 crystalline basement from Val Clapa (Alto Adige, northeastern Italy). *Memorie degli Istituti d*
1334 *Geologia e Mineralogia dell'Università di Padova* XXX, 6–23.
- 1335 Holt, A.F., Royden, L.H., Becker, T.W., 2017. The dynamics of double slab subduction.
1336 *Geophysical Journal International* 209, 250–265.
- 1337 Honda, S., Saito, M., 2003. Small-scale convection under the back-arc occurring in the low
1338 viscosity wedge. *Earth and Planetary Science Letters* 216, 703–715.
- 1339 Kirby, S. H., 1983. Rheology of the lithosphere. *Rev. Geophys.* 21(6), 1459-1487.
- 1340 Konopasek, J., Schulmann, K., 2005. Contrasting Early Carboniferous field geotherms: evidence for
1341 accretion of a thickened orogenic root and subducted Saxothuringian crust (Central European
1342 Variscides). *Journal of the Geological Society of London* 162, 463-470.
- 1343 Konzett, J., Miller, C., Armstrong, R., Thöni, M., 2005. Metamorphic evolution of iron-rich mafic
1344 cumulates from the Ötztal-Stubai crystalline complex, Eastern Alps, Austria. *Journal of*
1345 *Petrology* 46(4), 717–747.
- 1346 Lafon, J.-M., 1986. Géochronologie U-Pb appliquée à deux segments du Massif central français: Le
1347 Rouergue oriental et le Limousin central. Ph.D. thesis, Université Montpellier.
- 1348 Lardeaux, J.-M., 2014a. Deciphering orogeny: a metamorphic perspective. Examples from
1349 European Alpine and Variscan belts. Part II: Variscan metamorphism in the French Massif
1350 Central – A review. *Bull. Soc. géol. France* 185(5), 281-310.
- 1351 Lardeaux, J.-M., 2014b. Deciphering orogeny: a metamorphic perspective. Examples from
1352 European Alpine and Variscan belts. Part I: Alpine metamorphism in the western Alps – A
1353 review. *Bull. Soc. géol. France* 185(2), 93-114.
- 1354 Lardeaux, J.-M., Dufour, E., 1987. Champs de déformation superposés dans la chaîne varisque.
1355 Exemple de la zone nord des Monts du Lyonnais (Massif Central français). *Compte Rendu*
1356 *Academie des Sciences de Paris* 305(2), 61–64.

- Journal Pre-proof
- 1357 Lardeaux, J.-M., Ledru, P., Daniel, I., Duchene, S., 2001. The Variscan French Massif Central - a
1358 new addition to the ultra-high pressure metamorphic 'club': exhumation processes and
1359 geodynamic consequences. *Tectonophysics* 332, 143-167.
- 1360 Lardeaux, J.-M., Reynard, B., Dufour, E., 1989. Granulites à kornéropine et décompression post-
1361 orogénique des Monts du Lyonnais (M.C.F.). *Compte Rendu Academie des Sciences de Paris*
1362 308(2), 1443-1449.
- 1363 Lardeaux, J. M., Schulmann, K., Faure, M., Janousek, V., Lexa, O., Skrzypek, E., Edel, J. B.,
1364 Stipska, P., 2014. The Moldanubian Zone in the French Massif Central, Vosges/Schwarzwald
1365 and Bohemian Massif revisited: differences and similarities. *Geological Society of London*,
1366 *Special Publications* 405, 7-44.
- 1367 Latouche, L., Bogdanoff, S., 1987. Évolution précoce du massif de l'Argentera: apport des éclogites
1368 et des granulites. *Géologie alpine* 63, 151-164.
- 1369 Le Bayon, B., Pitra, P., Balleve, M., Bohn, M., 2006. Reconstructing P-T paths during continental
1370 collision using multi-stage garnet (Gran Paradiso nappe, Western Alps). *Journal of*
1371 *Metamorphic Geology* 24(6), 477-496.
- 1372 Le Fort, P., 1973. *Geologie du Haut-Dauphine cristallin (Alpes Francaise): Etudes petrologique et*
1373 *structurale de la partie occidentale*. Ph.D. thesis, Université Nancy.
- 1374 Ledru, P., Autran, A., Santallier, D. 1994. Lithostratigraphy of Variscan terranes in the French
1375 Massif Central. A basis for paleogeographical reconstruction. In: Chantraine, J., Rolet, J.,
1376 Santallier, D. S., Piqué, A., Keppie J.D. (eds.), *Pre-Mesozoic Geology in France and Related*
1377 *Areas., IGCP-Project 233 (Terranes In The Circum-Atlantic Paleozoic Orogens)*, Springer
1378 Verlag, Berlin, pp. 276-288.
- 1379 Ledru, P., Courrioux, G., Dallain, C., Lardeaux, J.-M., Montel, J. M., Vanderhaeghe, O., Vitel, G.,
1380 2001. The Velay dome (French Massif Central): Melt generation and granite emplacement
1381 during orogenic evolution. *Tectonophysics* 342(3-4), 207-237.

- Journal Pre-proof
- 1382 Ledru, P., Lardeaux, J.-M., Santallier, D., Autran, A., Quenardel, J.-M., Floch, J.-P., Lerouge, G.,
1383 Maillet, N., Marchand, J., Ploquin, A., 1989. Où sont les nappes dans le Massif central
1384 français? *Bulletin de la Societe Geologique de France* 8(3), 605-618.
- 1385 Liati, A., Gebauer, D., Fanning, M., 2009. Geochronological evolution of HP metamorphic rocks of
1386 the Adula nappe, Central Alps, in pre-Alpine and Alpine subduction cycles. *Journal of*
1387 *Geological Society* 166, 797-810.
- 1388 Liégeois, J. P., Duchesne, J. C., 1981. The Lac Cornu retrograded eclogites (Aiguilles Rouges
1389 massif, Western Alps, France): evidence of crustal origin and metasomatic alteration. *Lithos*
1390 14(1), 35–48.
- 1391 Lotout, C., Pitra, P., Poujol, M., Anczkiewicz, R., Van Den Driessche, J., 2018. Timing and
1392 duration of Variscan high-pressure metamorphism in the French Massif Central: A
1393 multimethod geochronological study from the Najac Massif. *Lithos* 308-309, 381-394.
- 1394 Lotout, C., Pitra, P., Poujol, M., Van Den Driessche, J., 2017. Ordovician magmatism in the
1395 Lévézou massif (French Massif Central): tectonic and geodynamic implications. *Int. Journal*
1396 *of Earth Science* 106, 501-515.
- 1397 Maillet, N. 1987. Dualité d'origine des massifs ultra-basiques limousins. Ph.D. Thesis, Université
1398 de Lyon I.
- 1399 Maino, M., Dallagiovanna, G., Gaggero, L., Seno, S., Tiepolo, M., 2012. U-Pb zircon
1400 geochronological and petrographic constraints on late to post-collisional Variscan magmatism
1401 and metamorphism in the Ligurian Alps, Italy. *Geological Journal* 47(6), 632–652.
- 1402 Malavieille, J., Guihot, P., Costa, S., Lardeaux, J.M., Gardien, V., 1990. Collapse of the thickened
1403 Variscan crust in the french Massif Central: Mont Pilat extensional shear zone and St Etienne
1404 late carboniferous basin. *Tectonophysics* 177, 139-149.
- 1405 Manzotti, P., Zucali, M., 2013. The pre-Alpine tectonic history of the Austroalpine continental
1406 basement in the Valpelline unit (Western Italian Alps). *Geological Magazine* 150(1), 153–172.

- Journal Pre-proof
- 1407 Marotta, A. M., Roda, M., Conte, K., Spalla, M. I., 2016. Thermo-mechanical numerical model of
1408 the transition from continental rifting to oceanic spreading: the case study of the Alpine
1409 Tethys. *Geological Magazine*, 1-30.
- 1410 Marotta, A. M., Spalla, M. I., 2007. Permian-Triassic high thermal regime in the Alps: Result of
1411 late Variscan collapse or continental rifting? Validation by numerical modeling. *Tectonics* 26,
1412 1–27.
- 1413 Marotta, A. M., Spelta, E., Rizzetto, C., 2006. Gravity signature of crustal subduction inferred from
1414 numerical modelling. *Geophys. J. Int.* 166, 923–938.
- 1415 Marotta, A.M., Splendore, R., Barzaghi, R., 2015. An application of model uncertainty statistical
1416 assessment: A case study of tectonic deformation in the Mediterranean. *Journal of*
1417 *Geodynamics* 85, 24-31.
- 1418 Marshall, D., Kirschner, D., Bussy, F., 1997. A Variscan pressure-temperature-time path for the N-
1419 E Mont Blanc massif. *Contributions to Mineralogy and Petrology* 126(4), 416–428.
- 1420 Matte, P., 1986. Tectonics and plate tectonics model for the Variscan belt of Europe.
1421 *Tectonophysics* 126, 329–374.
- 1422 Matte, P., 2001. The Variscan collage and orogeny (480-290 Ma) and the tectonic definition of the
1423 Armorica microplate: A review. *Terra Nova* 13(2), 122-128.
- 1424 Meda, M., Marotta, A. M., Spalla, M. I. 2010. The role of mantle hydration into continental crust
1425 recycling in the wedge region. In: Spalla, M. I., Marotta, A. M., Gosso, G. (eds.), *Advances in*
1426 *Interpretation of Geological Processes*. Geological Society, London, Special Publications, vol. 332,
1427 pp. 149-171.
- 1428 Melcher, F., Meisel, T., Puhl, J., Koller, F., 2002. Petrogenesis and geotectonic setting of
1429 ultramafic rocks in the Eastern Alps: constraints from geochemistry. *Lithos* 65(1-2), 69-112.
- 1430 Ménot, R.-P., Bonhommem, M., Vivier, G., 1987. Structuration tecto-métamorphique
1431 carbonifère dans le massif de Belledonne (Alpes occidentales françaises). *Apport de la*

- 1432 geochronologie K/Ar des amphiboles. Schweizerische mineralogische und petrographische
1433 Mitteilungen 67, 273–284.
- 1434 Mercier, L., Johan, V., Lardeaux, J.-M., Ledru, P., 1989. Découverte d'éclogites dans l'artense
1435 (M.C.F.) Implications pour la définition des nappes à l'Est du Sillon Houiller. Compte Rendu
1436 Academie des Sciences de Paris 308(2), 315–320.
- 1437 Mercier, L., Johan, V., Lardeaux, J.-M., Ledru, P., 1992. Evolutions tectono-métamorphiques
1438 des nappes de l'Aretense (Massif central français): nouveaux marqueurs de la collision dans la
1439 chaîne varisque. Bulletin de la Société Géologique de France 163(3), 293–308.
- 1440 Mercier, L., Lardeaux, J.-M., Davy, P., 1991. On the tectonic significance of retrograde P-T-t
1441 paths in eclogites of the French Massif Central. Tectonics 10(1), 131-140.
- 1442 Mercier, L., van Roermund, H. L. M., Lardeaux, J.-M., 1991a. Comparison of Ptt paths in
1443 allochthonous high pressure metamorphic terrains from the Scandinavian Caledonides and
1444 the French Massif Central: Contrasted thermal structures during uplift. Geologische Rundschau
1445 80(2), 333–348.
- 1446 Messiga, B., Tribuzio, R., Caucia, F., 1992. Amphibole evolution in Variscan eclogite-
1447 amphibolites from the Savona crystalline massif (Western Ligurian Alps, Italy): controls on
1448 the decompressional P-T-t path. Lithos 27, 215–230.
- 1449 Milano, P., Pennacchioni, G., Spalla, M. I., 1988. Alpine and pre-Alpine tectonics in the Central
1450 Orobic Alps (Southern Alps). Eclogae Geologicae Helvetiae 81, 273-293.
- 1451 Miller, C., Thöni, M., 1995. Origin of eclogites from the Austroalpine Ötztal basement (Tirol,
1452 Austria): geochemistry and Sm–Nd vs. Rb–Sr isotope systematics. Chemical Geology 122,
1453 199–225.
- 1454 Mishin, Y.A., Gerya, T.V., Burg, J.-P., Connolly, J.A.D., 2008. Dynamics of double subduction:
1455 Numerical modeling. Physics of the Earth and Planetary Interiors 171, 280–295.
- 1456 Monié, P., 1990. Preservation of Hercynian $^{40}\text{Ar}/^{39}\text{Ar}$ ages through high-pressure low-temperature
1457 Alpine metamorphism in the Western Alps. European Journal of Mineralogy 2(3), 343–361.

- Journal Pre-proof
- 1458 Morten, L., Nimis, P., Rampone, E., 2004. Records of mantle–crust exchange processes during
1459 continental subduction–exhumation in the Nonsberg-Ultental garnet peridotites (eastern Alps).
1460 A review. *Periodico di Mineralogia* 73, 119–129.
- 1461 Mottana, A., Nicoletti, M., Petrucciani, C., Liborio, G., De Capitani, L., Bocchio, R., 1985. Pre-
1462 alpine and alpine evolution of the South-alpine basement of the Orobic Alps. *Geologische*
1463 *Rundschau* 74(2), 353–366.
- 1464 Nussbaum, C., Marquer, D., Biino, G. G., 1998. Two subduction events in a polycyclic basement:
1465 Alpine and pre-Alpine high-pressure metamorphism in the Suretta nappe, Swiss Eastern
1466 Alps. *Journal of Metamorphic Geology* 16, 591-605.
- 1467 Paquette, J. L., Ballèvre, M., Peucat, J.-J., Cornen, G., 2017. From opening to subduction of an
1468 oceanic domain constrained by LA-ICP-MS U-Pb zircon dating (Variscan belt, Southern
1469 Armorican Massif, France). *Lithos* 294-295, 418-437.
- 1470 Paquette, J. L., Ménot, R. P., Peucat, J. J., 1989. REE, Sm-Nd and U-Pb zircon study of eclogites
1471 from the Alpine External Massifs (Western Alps): evidence for crustal contamination. *Earth*
1472 *and Planetary Science Letters* 96(1-2), 181–198.
- 1473 Paquette, J.-L., Monchoux, P., Couturier, M., 1995. Geochemical and isotopic study of a norite-
1474 eclogite transition in the European Variscan belt: Implications for U-Pb zircon systematics in
1475 metabasic rocks. *Geochimica et Cosmochimica Acta* 59(8), 1611–1622.
- 1476 Pickering, K. T., 1989. The destruction of Iapetus and Tornquist’s Oceans. *Geology Today* 5, 160-
1477 166.
- 1478 Pin, C., 1990. Variscan oceans: Ages, origins and geodynamic implications inferred from
1479 geochemical and radiometric data. *Tectonophysics* 17(1), 215-227.
- 1480 Pin, C., Lancelot, J., 1982. U-Pb dating of an early Paleozoic bimodal magmatism in the French
1481 Massif Central and of its further metamorphic evolution. *Contributions to Mineralogy and*
1482 *Petrology* 79(1), 1–12.

- Journal Pre-proof
- 1483 Pin, C., Paquette, J. L., 1997. A mantle-derived bimodal suite in the Hercynian Belt: Nd isotope
1484 and trace element evidence for a subduction-related rift origin of the Late Devonian Brévenne
1485 metavolcanics, Massif Central (France). *Contrib. Mineral. Petrol.* 129, 222-238.
- 1486 Pin, C., Paquette, J. L., 2002. Le magmatisme basique calcoalcalin d'âge dévono-dinantien du
1487 nord du Massif Central, témoin d'une marge active hercynienne: arguments géochimiques et
1488 isotopiques Sr/Nd. *Geodinamica Acta* 15:1, 63-77.
- 1489 Pin, C., Peucat, J.-J., 1986. Ages des épisodes de métamorphisme paléozoïque dans le Massif
1490 central et le massif armoricain. *Bulletin de la Société Géologique de France* 3, 461-169 (in
1491 French with English abstract).
- 1492 Platt, J.P., 1986). Dynamics of orogenic wedges and the uplift of high-pressure metamorphic
1493 rocks. *Geol. Soc. Am. Bull.* 97, 1037-1053.
- 1494 Polino, R., Dal Piaz, G. V., Gosso, G., 1990. Tectonic erosion at the Adria margin and
1495 accretionary processes for the Cretaceous orogeny of the Alps. *Mem. Soc. géol. Fr.* 156,
1496 345-367.
- 1497 Rampone, E.. 2002. Mantle dynamics during Permo-Mesozoic extension of the Europe-Adria
1498 lithosphere: insights from the Ligurian ophiolites. *Periodico di Mineralogia* 73, 215– 230.
- 1499 Ranalli, G., Murphy, D. C., 1987. Rheological stratification of the lithosphere. *Tectonophysics*
1500 132(4), 281–295.
- 1501 Rebay, G., Riccardi, M. P., Spalla, M. I., 2015. Fluid rock interactions as recorded by Cl-rich
1502 amphiboles from continental and oceanic crust of Italian orogenic belts. *Periodico di*
1503 *Mineralogia* 84(3B), 751-777.
- 1504 Regorda, A., Roda, M., Marotta, A. M., Spalla, M. I., 2017. 2-D numerical study of hydrated wedge
1505 dynamics from subduction to post-collisional phases. *Geophysical Journal International* 211,
1506 974–1000.
- 1507 Riklin, K., 1983. Kontaktmetamorphose permischer Sandsteine im Adamello-Massiv. Ph.D. thesis,
1508 ETH Zurich.

- Journal Pre-proof
- 1509 Roda, M., Marotta, A. M., Spalla, M. I., 2010. Numerical simulations of an ocean-continent
1510 convergent system: Influence of subduction geometry and mantle wedge hydration on crustal
1511 recycling. *Geochemistry, Geophysics, Geosystems* 11(5), 1-21.
- 1512 Roda, M., Marotta, A. M., Spalla, M. I., 2011. The effects of the overriding plate thermal state on
1513 the slab dip in an ocean–continent subduction system. *C. R. Acad. Sci. Paris* 343, 323–330.
- 1514 Roda, M., Spalla, M. I., Marotta, A. M., 2012. Integration of natural data within a numerical model
1515 of ablative subduction: a possible interpretation for the Alpine dynamics of the Austroalpine
1516 crust. *J. Metamorphic Geol.* 30(9), 973–996.
- 1517 Roda, M., Regorda, A., Spalla, M. I., Marotta, A. M., 2018a. What drives Alpine Tethys opening:
1518 clues from the review of geological data and model predictions. *Geological Journal*, 1-19.
- 1519 Roda, M., Zucali, M., Li, Z.-X., Spalla, M. I., Yao, W., 2018b. Pre-Alpine contrasting tectono-
1520 metamorphic evolutions within the Southern Steep Belt, Central Alps. *Lithos* 310-311, 31-49.
- 1521 Rode, S., Rosel, D., Schulz, B., 2012. Constraints on the Variscan P-T evolution by EMP Th-U-Pb
1522 monazite dating in the polymetamorphic Austroalpine Oetzal-Stubai basement (Eastern Alps).
1523 *Z. dt. Ges. Geowiss.* 163(1), 43–68.
- 1524 Rolland, Y., Rossi, M., Cox, S. F., Corsini, M., Mancktelow, N., Pennacchioni, G., Fornari, M.,
1525 Boullier, A. M., 2008. $^{40}\text{Ar}/^{39}\text{Ar}$ dating of synkinematic white mica: insights from fluid – rock
1526 reaction in low-grade shear zones (Mont Blanc Massif) and constraints on timing of
1527 deformation in the NW external Alps. In: Wibberley, C. A. J., Kurz, W., Imber, J.,
1528 Holdsworth, R. E., Collettini, C. (eds.), *The Internal Structure of Fault Zones: Implications*
1529 *for Mechanical and Fluid-Flow Properties*. The Geological Society, London, vol. 299, pp.
1530 293-315.
- 1531 Rosenbaum, G., Lister, G. S., 2005. The western Alps from the Jurassic to Oligocene: spatio-
1532 temporal constraints and evolutionary reconstructions. *Earth Sci. Rev.* 69, 281-306.

- Journal Pre-proof
- 1533 Rottura, A., Bargossi, G. M., Caggianelli, A., Del Moro, A., Visonà, D., Tranne, C. A., 1998.
1534 Origin and significance of the Permian high-K calc-alkaline magmatism in the central-eastern
1535 Southern Alps, Italy. *Lithos* 45, 329– 348.
- 1536 Rubatto, D., Ferrando, S., Compagnoni, R., Lombardo, B., 2010. Carboniferous high-pressure
1537 metamorphism of Ordovician protoliths in the Argentera Massif (Italy), Southern European
1538 Variscan belt. *Lithos* 116, 65-76.
- 1539 Sanchez, G., Rolland, Y., Schneider, J., Corsini, M., Oliot, E., Goncalves, P., Verati, C., Lardeaux,
1540 J. M., Marquer, D., 2011. Dating low-temperature deformation by $^{40}\text{Ar}/^{39}\text{Ar}$ on white mica,
1541 insights from the Argentera-Mercantour Massif (SW Alps). *Lithos* 125, 521– 536.
- 1542 Sassi, R., Mazzoli, C., Miller, C., Konzett, J., 2004. Geochemistry and metamorphic evolution of
1543 the Pohorje Mountain eclogites from the easternmost Austroalpine basement of the Eastern
1544 Alps (Northern Slovenia). *Lithos* 78, 235-261.
- 1545 Schmidt, M. W., Poli, S., 1998. Experimentally based water budgets for dehydrating slabs and
1546 consequences for arc magma generation. *Earth and Planetary Science Letters* 163, 361–379.
- 1547 Schmid, S. M., Fügenschuh, B., Kissling, E., Schuster, R., 2004. Tectonic map and overall
1548 architecture of the Alpine orogen. *Eclogae Geol. Helv.* 97, 93-117.
- 1549 Schulmann, K., Konopásek, J., Janoušek, V., Lexa, O., Lardeaux, J.-M., Edel, J. B., Štípská, P.,
1550 Ulrich, S., 2009. An Andean type Palaeozoic convergence in the Bohemian Massif. *Comptes*
1551 *Rendus Geoscience* 341(2-3), 266-286.
- 1552 Schulmann, K., Kroner, A., Hegner, E., Wendt, I., Konopasek, J., Lexa, O., Štípská, P., 2005.
1553 Chronological constraints on the Pre-Orogenic history, burial and exhumation of the
1554 Variscan orogen, Bohemian Massif, Czech Republic. *American Journal of Science* 305,
1555 407-448.
- 1556 Schulmann, K., Lexa, O., Janoušek, V., Lardeaux, J.-M., Edel, J. B., 2014. Anatomy of a diffuse
1557 cryptic suture zone: An example from the Bohemian Massif, European Variscides. *Geology*
1558 42(4), 275-278.

- Journal Pre-proof
- 1559 Schulz, B., von Raumer, J. F., 2011. Discovery of Ordovician-Silurian metamorphic monazite in
1560 garnet metapelites of the Alpine External Aiguilles Rouges Massif. *Swiss Journal of*
1561 *Geosciences* 104(1), 67–79.
- 1562 Schuster, R., Scharbert, S., Abart, R., Frank, W., 2001. Permo-Triassic extension and related
1563 HT/LP metamorphism in the Austroalpine-Southalpine realm. *Mitteilungen der Gesellschaft*
1564 *der Geologie und Bergbaustudenten in Österreich* 45, 111– 141.
- 1565 Schweinehage, R., Massonne, H., 1999. Geochemistry and metamorphic evolution of
1566 metabasites from the Silvretta nappe, Eastern Alps. *Memorie Scienze Geologiche* 51(1),
1567 191– 203.
- 1568 Siletto, G. B., Spalla, M. I., Tunesi, A., Lardeaux, J.-M., Colombo, A., 1993. Pre-Alpine
1569 Structural and Metamorphic Histories in the Orobic Southern Alps, Italy. In: von Raumer, J.
1570 F., Neubauer, F. (eds.), *Pre-Mesozoic Geology in the Alps*. Springer-Verlag, Heidelberg, pp.
1571 585-598.
- 1572 Skrzypek, E., Schulmann, K., Tabaud, A.-S., Edel, J. B., 2014. Palaeozoic evolution of the
1573 Variscan Vosges Mountains. In: Schulmann, K., Martinez Catalan, J. R., Lardeaux, J.-M.,
1574 Janoušek, V., Oggiano, G. (eds.), *The Variscan Orogeny: Extent, Timescale and the*
1575 *Formation of the European Crust*. Geological Society, London, vol. 405, pp. 45-75.
- 1576 Spalla, M. I., Lardeaux, J.-M., Dal Piaz, G. V., Gosso, G., Messiga B., 1996. Tectonic
1577 significance of the Alpine eclogites. *Journal of Geodynamics* 21, 257-285.
- 1578 Spalla, M. I., Carminati, E., Ceriani, S., Oliva, A., Battaglia, D., 1999. Influence of deformation
1579 partitioning and metamorphic re-equilibration on P-T path reconstruction in the pre-Alpine
1580 basement of central Southern Alps (Northern Italy). *Journal of Metamorphic Geology* 17(3),
1581 319–336.
- 1582 Spalla, M., Diella, V., Pigazzini, N., Siletto, G., Gosso, G., 2006. Significato tettonico della
1583 transizione Cld-And nelle metapeliti del Basamento Sudalpino (Alta Val Camonica).
1584 *Rendiconti della Società Geologica Italiana* 2, 182–183.

- 1585 Spalla, M. I., Gosso, G., 1999. Pre-Alpine tectonometamorphic units in the central southern Alps;
1586 structural and metamorphic memory. *Memorie di Scienze Geologiche Padova* 51(1), 221–
1587 229.
- 1588 Spalla, M. I., Marotta, A. M., 2007. P-T evolutions vs. numerical modelling: a key to unravel
1589 the Paleozoic to early-Mesozoic tectonic evolution of the Alpine area. *Periodico di*
1590 *Mineralogia* 76(2-3), 267-308.
- 1591 Spalla, M. I., Zanoni, D., Gosso, G., Zucali, M., 2009. Deciphering the geologic memory of a
1592 Permian conglomerate of the Southern Alps by pebble P-T estimates. *International Journal of*
1593 *Earth Sciences* 98(1), 203–226.
- 1594 Spalla, M. I., Zanoni, D., Marotta, A. M., Rebay, G., Roda, M., Zucali, M., Gosso, G., 2014.
1595 The transition from Variscan collision to continental break-up in the Alps: advice from the
1596 comparison between natural data and numerical model predictions. *Geological Society,*
1597 *London, Special Publications* 405(1), 363-400.
- 1598 Spiess, R., Cesare, B., Mazzoli, C., Sassi, R., Sassi, F. P., 2010. The crystalline basement of the
1599 Adria microplate in the eastern Alps: a review of the palaeo- structural evolution from the
1600 Neoproterozoic to the Cenozoic. *Rendiconti Lincei Scienze Fisiche Naturali* 21, 31-50.
- 1601 Splendore, R., Marotta, A.M., Barzaghi, R., 2015. Tectonic deformation in the Tyrrhenian: A novel
1602 statistical approach to infer the role of the Calabrian Arc complex. *JGR Solid Earth* 120(11), 1-
1603 20.
- 1604 Stähle, V., Frenzel, G., Hess, J. C., 2001. Permian metabasalt and Triassic alkaline dykes in the
1605 northern Ivrea zone: clues to the post-Variscan geodynamic evolution of the Southern Alps.
1606 *Schweizerische Mineralogische und Petrographische Mitteilungen* 81, 1– 21.
- 1607 Stampfli, G. M., von Raumer, G. M., Borel, G. D., 2002. Paleozoic evolution of pre-Variscan
1608 terranes: From Gondwana to the Variscan collision. In: Martínez Catalán, J.R., Hatcher, R. D.,
1609 Jr., Arenas, R., Díaz García, F. (eds.), *Variscan-Appalachian dynamics: The building of the late*
1610 *Paleozoic basement. Geol. Soc. of America Special Paper*, vol. 364, pp. 263-280.

- Journal Pre-proof
- 1611 Stöckhert, B., Gerya T. V., 2005. Pre-collisional high-pressure metamorphism and nappe tectonics
1612 at active continental margins: a numerical simulation. *Terra Nova* 17, 102-110.
- 1613 Tait, J.A., Bachtadse, V., Franke, W., Soffel, H.C., 1997. Geodynamic evolution of the European
1614 Variscan fold belt: palaeomagnetic and geological constraints. *Geol. Rundsch.* 86, 585-598.
- 1615 Thélin, P., Sartori, M., Burri, M., Gouffon, Y., Chessex, R., 1993. The pre-Alpine basement of
1616 the Briançonnais (Wallis, Switzerland). In: von Raumer, J. F., Neubauer, F. (eds.), *Pre-*
1617 *Mesozoic Geology in the Alps*, Springer-Verlag, Heidelberg, pp. 297–315.
- 1618 Thélin, P., Sartori, M., Lengeler, R., Schaerer, J.-P., 1990. Eclogites of Paleozoic or early Alpine
1619 age in the basement of the Penninic Siviez-Mischabel nappe, Wallis, Switzerland. *Lithos* 25,
1620 71-88.
- 1621 Thöni, M., 1981. Degree and evolution of the alpine metamorphism in the austroalpine unit west
1622 of the Hohe tauern in the light of K/Ar and Rb/Sr age determinations on micas. *Jahrbuch der*
1623 *Geologischen Bundesanstalt* 124, 111–174.
- 1624 Thöni, M., 2002. Sm–Nd isotope systematics in garnet from different lithologies (Eastern Alps):
1625 age results, and an evaluation of potential problems for garnet Sm–Nd chronometry.
1626 *Chemical Geology* 185, 255–281.
- 1627 Torsvik, T. H., 1998. Palaeozoic palaeogeography: A North Atlantic viewpoint. *GFF* 120, 109-118.
- 1628 Trench, A., Torsvik, T. H., 1991. A revised Palaeozoic apparent polar wander path for Southern
1629 Britain (Eastern Avalonia). *Geophysical Journal International* 104, 227-233.
- 1630 Tumiaty, S., Thöni, M., Nimis, P., Martin, S., Mair, V., 2003. Mantle-crust interactions during
1631 Variscan subduction in the Eastern Alps (Nonsberg-Ulten zone): Geochronology and new
1632 petrological constraints. *Earth and Planetary Science Letters* 210(3-4), 509–526.
- 1633 Turcotte, D. L., Schubert, G., 2002. *Geodynamics*. Second ed., Cambridge University Press, New
1634 York, 848 pp.
- 1635 Vivier, G., Ménot, R. P., Giraud, P., 1987. Magmatismes et structuration orogénique Paléozoïques
1636 de la chaîne de la Belledonne. *Géologie Alpine* 63, 25-53.

- 1637 von Quadt, A., Guenther, D., Frischknecht, R., Zimmermann, R., Franz, G., 1997. The evolution of
1638 pre-Variscan eclogites of the Tauern Window (Eastern Alps): a Sm/Nd, conventional and
1639 Laser ICP-MS zircon U-Pb study. *Schweizerische Mineralogische und Petrographische*
1640 *Mitteilungen* 77, 265–279.
- 1641 von Raumer, J. F., 1974. Zur Metamorphose amphibolitischer Gesteine im Altkristallin des Mont-
1642 Blanc- und Agulles-Rouges-Massivs. *Schweizerische Mineralogische und Petrographische*
1643 *Mitteilungen* 54, 471– 488.
- 1644 von Raumer, J. F., 1998. The Palaeozoic evolution in the Alps: from Gondwana to Pangea. *Geol.*
1645 *Rundsch.* 87, 407-435.
- 1646 von Raumer, J. F., Abrecht, J., Bussy, F., Lombardo, B., Ménot, R. P., Schaltegger, U., 1999. The
1647 Palaeozoic metamorphic evolution of the Alpine External Massifs. *Schweizerische*
1648 *Mineralogische und Petrographische Mitteilungen* 79(1), 5–22.
- 1649 von Raumer, J. F., Bussy, F., Schaltegger, U., Schulz, B., Stampfli, G. M., 2013. Pre-Mesozoic
1650 Alpine basements - Their place in the European Paleozoic framework. *GSA Bulletin* 125(1-2),
1651 89-108.
- 1652 von Raumer, J. F., Stampfli, G. M., Bussy, F., 2003. Gondwana-derived microcontinents — the
1653 constituents of the Variscan and Alpine collisional orogens. *Tectonophysics* 365, 7-22.
- 1654 Wessel, P., Smith, W. H. F., 1998. New, improved version of Generic Mapping Tools released.
1655 *EOS Trans. AGU* 79(47), 579.
- 1656 Whitney, D., Roger, F., Rey, P., Teyssier, C., 2015. Exhumation of high-pressure rocks in a
1657 Variscan migmatite dome (Montagne Noire, France). *Geophysical Research Abstracts* 17,
1658 EGU2015-3266.
- 1659 Will, T. M., Schmadicke, E., Ling, X.-X., Li, X.-H., Li, Q.-L., 2018. New evidence for an old
1660 idea: Geochronological constraints for a paired metamorphic belt in the central European
1661 Variscides. *Lithos* 302-303, 278-297.

- Journal Pre-proof
- 1662 Zanoni, D., Spalla, M. I., 2018. The Variscan evolution in basement cobbles of the Permian
1663 Ponteranica Formation by microstructural and petrologic analysis. *Ital. J. Geosci.* 137, 254-
1664 271.
- 1665 Zanoni, D., Spalla, M. I., Gosso, G., 2010. Vestiges of lost tectonic units in conglomerate
1666 pebbles? A test in Permian sequences of the Southalpine Orobic Alps. *Geological Magazine*
1667 147(1), 98–122.
- 1668 Zimmermann, V. R., Franz, G., 1989. Die Eklogite der Unteren Schieferhülle;
1669 Frosnitzal/Südvenediger (Tauern, Österreich). *Mitteilungen der Österreichischen*
1670 *Geologischen Gesellschaft* 81, 167–188.
- 1671 Zucali, M., 2001. La correlazione nei terreni metamorfici: due esempi dall'Austroalpino occidentale
1672 (Zona Sesia-Lanzo) e centrale (Falda Languard-Campo/ Serie del Tonale). Ph.D. thesis,
1673 Università degli Studi di Milano.
- 1674 Zucali, M., Spalla, M. I., 2011. Prograde lawsonite during the flow of continental crust in the
1675 Alpine subduction: Strain vs. metamorphism partitioning, a field-analysis approach to infer
1676 tectonometamorphic evolutions (Sesia-Lanzo Zone, Western Italian Alps). *Journal of*
1677 *Structural Geology* 33(3), 381–398.

1678 **APPENDIX A**

1679

1680 Table A1 Details of the Variscan metamorphism in the Alps.

1681

1682 Table A2 Details of the Variscan metamorphism in the FMC.

Journal Pre-proof

1683 **Tables**

1684

1685 Table 1 P_{\max} -T estimates recorded in the crustal and mantle rocks of the Alps.

1686 Helvetic domain (Hv): AR–Argentera; BD–Belledonne; P–Pelvoux; Ai–Aiguilles Rouges; MB–

1687 Mont Blanc. Penninic domain (Pv): LB–Ligurian Brianconnais; GP–Gran Paradiso; MR–Monte

1688 Rosa; GS–Grand ST. Bernardo; Ad–Adula; SU–Suretta; TW–Tauern window. Austroalpine domain

1689 (Av): SC–Speik Complex; Oe–Oetztal; TZ–Ulten Zone; Sil–Silvretta; LCN–Languard-Campo

1690 nappe; DB–Dent Blanche. Southalpine domain (Sv): DCZ–Domaso-Cortafò Zone; VVB–Val

1691 Vedello basement; NEOB–NE Orobic basement; TVB–Tre Valli Bresciane; Ei–Eisecktal.

1692

1693 Table 2 P_{\max} -T estimates recorded in the crustal and mantle rocks of the FMC. UGU–Upper

1694 Gneiss Unit; LGU–Lower Gneiss Unit; LAC–Leptyno-amphibolitic Complex; PAU–Para-

1695 autochthonous Unit; MN–Montagne Noire fold-and-thrust Belt; TPU–Thiviers-Payzac Unit.

1696

1697 Table 3 Material and rheological parameters used in the numerical modelling.

1698

1699 **Figure captions**

1700 Fig. 1 Simplified tectonic sketch of the Variscan belt (modified after Delleani et al., 2018 and
1701 references therein). Arm–Armorican Massif; BCBF–Bristol Channel-Bray Fault; BM–Bohemian
1702 Massif; Ca–Cantabrian terrane; Cib–Central Iberian; Co–Corsica; FMC–French Massif Central;
1703 MT–Maures-Tanneron Massif; OM–Ossa Morena; Py–Pyrenees; Sa–Sardinia; Si–Sicilian-Apulian
1704 basements; SP–South Portuguese Zone; WL–West Asturian-Leonese.

1705

1706 Fig. 2 Tectonic map of the Alps with the localisation of the data listed in Table 1. Red lines are
1707 major tectonic lineaments.

1708

1709 Fig. 3 Tectonic map of the French Massif Central with the localisation of the data in Table 2. Red
1710 areas represent the Upper Gneiss Unit, blue areas the Lower Gneiss Unit, light blue areas the Para-
1711 autochthonous Unit, green areas the Thiviers-Payzac Unit, yellow represent the Montagne Noire
1712 and brown represent the Fold-and-Thrust belt.

1713

1714 Fig. 4 Setup, boundary conditions, initial thermal configuration and acronyms of the numerical
1715 models. The distances are not to scale. UP–upper plate; LP–lower plate.

1716

1717 Fig. 5 Markers distribution, isotherms 800 and 1100 K (dashed black lines) and streamline
1718 patterns (solid black lines in the insets) in the surrounding of the wedge area for models DS.1 (a),
1719 DS.2.5 (b) and DS.5 (c) at 25.5 Myr of evolution of the phase 1. Streamlines are curves tangent at
1720 the velocity of the fluid. The difference $\Delta\Psi$ of values between two streamlines is equivalent to the
1721 flow capacity per unit of thickness across the two streamlines. Curves that differ from each other by
1722 the same amount of $\Delta\Psi$ gather in areas where the flow has a higher velocity.

1723

1724 Fig. 6 Large-scale temperature field (colours) and streamline patterns (black lines) predicted by the
1725 models DS. t_r indicates the time relative to the beginning of phase 3 and t_0 indicates the time from
1726 the beginning of the evolution. Streamlines are curves tangent at the velocity of the fluid. The
1727 difference $\Delta\Psi$ of values between two streamlines is equivalent to the flow capacity per unit of
1728 thickness across the two streamlines. Curves that differ from each other by the same amount of $\Delta\Psi$
1729 $\Delta\Psi$ gather in areas where the flow has a higher velocity.

1730

1731 Fig. 7 Comparison between the isotherms 800 (continuous lines) and 1100 K (dashed lines)
1732 predicted by model SS.5 during phases 1 and 2 (green lines) and by models DS.1, DS.2.5 and DS.5
1733 during phases 3 and 4 (black, red and blue lines, respectively). t_r indicates the time relative to the
1734 beginning of phase 2 for model SS.5 and of phase 4 for models DS; t indicates the time relative to
1735 the beginning of phase 1 for model SS.5 and of phase 3 for models DS.

1736

1737 Fig. 8 Markers distribution, isotherms 800 and 1100 K (dashed black lines) and streamline
1738 patterns (solid black lines in the insets) in the surrounding of the wedge area for models DS.1
1739 (panels a_i), DS.2.5 (panels b_i) and DS.5 (panels c_i) at different times of evolution the of phase 3. t_r
1740 indicates the time relative to the beginning of phase 3 and t_0 indicates the time from the beginning
1741 of the evolution. Streamlines are curves tangent at the velocity of the fluid. The difference $\Delta\Psi$ of
1742 values between two streamlines is equivalent to the flow capacity per unit of thickness across the
1743 two streamlines. Curves that differ from each other by the same amount of $\Delta\Psi$ gather in areas
1744 where the flow has a higher velocity.

1745

1746 Fig. 9 Large-scale temperature field (colours) and streamline patterns (black lines) predicted by the
1747 models DS at 10 Myr (panels a_i) and 42 Myr (panels b_i) after the beginning of phase 4. t_r indicates
1748 the time relative to the beginning of phase 4 and t_0 indicates the time from the beginning of the
1749 evolution. Streamlines are curves tangent at the velocity of the fluid. The difference $\Delta\Psi$ of values

1750 between two streamlines is equivalent to the flow capacity per unit of thickness across the two
1751 streamlines. Curves that differ from each other by the same amount of $\Delta\Psi$ gather in areas where the
1752 flow has a higher velocity.

1753

1754 Fig. 10 Comparison between the isotherms 800 (continuous lines) and 1100 K (dashed lines)
1755 predicted by model SS.5 (green lines) and by models DS.1, DS.2.5 and DS.5 (black, red and blue
1756 lines, respectively), at 72 Myr (a) and 130 Myr (b) from the beginning of the evolution.

1757

1758 Fig. 11 Fitting of natural P_{\max} -T estimates of the Alps (a) and of the FMC (b) with model DS.2.5.
1759 Black bars represent the age of natural P-T estimates, while colour bars represent the fitting with the
1760 markers of the model, with different colours indicating the number of the marker showing the
1761 agreement. Red vertical lines identify the beginning of phases 2 and 4, while blue vertical lines
1762 identify the beginning of phase 3. Keys are the same as listed in Tables 1 and 2. Red keys represent
1763 geological ages, black keys represent radiometric ages.

1764

1765 Fig. 12 P_{\max} -T estimates of data from the Helvetic domain (a), the Penninic domain (b), the
1766 Austroalpine domain (c), the Southalpine domain (d) and from the FMC (e). Different colours of
1767 the data indicate different lithological affinities as described in the legend. Dot lines represent very
1768 low subduction-zone geothermal gradient (5 °C/km).

1769

1770 Fig. 13 Comparison between model DS.2.5 and P_{\max} -T estimates from the Alps for different times
1771 during phases 1 (a–d) and 2 (e). In agreement with notation in Fig. 2, red dots indicate fitting with
1772 data from the Helvetic domain, light blue dots fitting with data from the Penninic domain, yellow
1773 dots fitting with data from Austroalpine domain and blue dots indicate fitting with Southalpine
1774 domain. t_a indicates the absolute time relative to and t_0 indicates the time from the beginning of the
1775 evolution.

1776

1777 Fig. 14 Comparison between model DS.2.5 and P_{\max} -T estimates from the FMC for different
1778 times during phases 1 (a–d) and 2 (e). In agreement with notations in Fig. 3, red dots indicate fitting
1779 with data from the UGU, blue dots indicate fitting with data from the LGU and light blue dots
1780 indicate fitting with data from the PAU t_a indicates the absolute time relative to and t_0 indicates the
1781 time from the beginning of the evolution.

1782

1783 Fig. 15 Comparison between model DS.2.5 and P_{\max} -T estimates from the Alps for different times
1784 during phases 3 (a–c) and 4 (d and e). In agreement with notation in Fig. 2, red dots indicate fitting
1785 with data from the Helvetic domain, light blue dots fitting with data from the Penninic domain,
1786 yellow dots fitting with data from Austroalpine domain and blue dots indicate fitting with
1787 Southalpine domain. t_a indicates the absolute time relative to and t_0 indicates the time from the
1788 beginning of the evolution.

1789

1790 Fig. 16 Comparison between model DS.2.5 and P_{\max} -T estimates from the FMC for different
1791 times during phases 1 (a–c) and 2 (d and e). In agreement with notations in Fig. 3, red dots indicate
1792 fitting with data from the UGU, blue dots indicate fitting with data from the LGU and light blue
1793 dots indicate fitting with data from the PAU, green dots indicate fitting with data from the TPU and
1794 yellow dots indicate fitting with data from MN. t_a indicates the absolute time relative to and t_0
1795 indicates the time from the beginning of the evolution.

1796

1797 Fig. 17 Fitting of natural P_{\max} -T estimates of the Alps (a) and of the FMC (b) with model SS.5.
1798 Black bars represent the age of natural P-T estimates, while colour bars represent the fitting with the
1799 markers of the model, with different colours indicating the number of the marker showing the
1800 agreement. Red vertical lines identify the beginning of phase 2. Keys are the same as listed in
1801 Tables 1 and 2. Red keys represent geological ages, black keys represent radiometric ages.

1802

1803 Fig. 18 Simplified tectonic sketch of the Variscan belt with the evolution for the FMC and the
1804 Alps as suggested by the fitting between natural P-T estimates and P-T predicted by the double
1805 subduction model (DS.2.5). Arm–Armorican Massif; FMC–French Massif Central; MT–Maures-
1806 Tanneron Massif.

Journal Pre-proof

Key	Location	Lithology	Paragenesis	T (°C)	P (GPa)	Age (Ma)	References
Hv1	AR: Tinèe; Gesso-Stura-Vésubie	Metabasite	Grt + Hbl + Cpx + Pl + Qtz	710–760	1.2–1.4	420–428 (U/Pb)	Latouche and Bogdanoff, 1987; Paquette et al., 1989
Hv2	AR: Frisson	Eclogite gneiss	Grt + Hbl + Cpx + Pl + Qtz + Ru/Ilm	720–750	1.33–1.43	336–344 (U/Pb)	Ferrando et al., 2008; Rubatto et al., 2010
Hv3	BD: Allemont	Metapelite	Grt + St + Ky + Bt + Ms + Pl + Qtz + Rt/Ilm + Sil + Crd	500–600	0.9–1.1	Devonian (350–420)	Guillot and Ménot, 1999; Guillot et al., 2009
Hv3b	BD: Allemont	Metapelite	Grt + Bt + Ms + Pl + Qtz + Sil	660–680	0.68–0.87	330–344 (U/Pb)	Fréville et al., 2018
Hv4	BD: Livet	Metapelite	Grt + St + Bt + Pl + Qtz + Ilm + Mu	530–650	0.6–1.0	297–407 (K/Ar)	Ménot et al., 1987; Guillot and Ménot, 1999; Guillot et al.
Hv4b	BD: Riouperoux-Livet	Metapelite	Grt + Bt + Ms + Ky + Ab + Pl + Qtz	400–430	0.6–0.78	330–344 (U/Pb)	Fréville et al., 2018
Hv4c	BD: Riouperoux-Livet	Metapelite	Grt + St + Bt + Ms + Qtz	590–620	0.52–0.66	330–344 (U/Pb)	Fréville et al., 2018
Hv5	P: Romanche valley	Metabasite	Amph + Pl + Qtz + Ilm + Bt	650–785	0.45–0.7	311–335 (Ar/Ar)	di Paola, 2001
Hv6	P: Oisan	Metabasite	Amph + Pl + Opx + Cpx + Grt + Qtz + Ru/Ilm	775–994	0.9–1.7	Variscan (295–425)	di Paola, 2001
Hv7	P: La Lavey	Metabasite	Amph + Pl + Cpx + Grt	800–900	1.3–1.5	Early Variscan (375–425)	Le Fort, 1973; Guillot et al., 1998
Hv8	P: Peyre Arguet	Metabasite	Amph + Pl + Grt + Opx	750–850	0.3–0.7	Variscan (295–425)	Le Fort, 1973; Grandjean et al., 1996; Guillot et al., 1998
Hv9	BD: Lac de la Croix; Beaufortin	Metabasite	Grt + Cpx + Pl + Qtz + Ru + Zr Grt + Hbl + Cpx + Qtz + Ru + Zo	610–670	1.1–1.3	382–398 (U/Pb)	Paquette et al., 1989; Guillot et al., 1998
Hv10	Ai: Lac Cornu	Metabasite	Grt + Cpx + Hbl + Qtz + Ru	725–750	1.5–1.6	387–403 (U/Pb)	Liégeois and Duchesne, 1981; Paquette et al., 1989; von
Hv11	Ai: Lac Cornu; Col de Bérard	Metapelite	Grt + Bt + Ms + Sil + Pl + Qtz	625–675	1.2–1.4	> 330	Schulz and von Raumer, 2011
Hv12	Ai: Emosson lake	Metapelite	Grt + Bt + Ms + Sil + Pl + Qtz	525–575	0.8–1.0	> 320	Genier et al., 2008
Hv13	MB: Mont Blanc	Amphibolite Skarn	Amph + Grt + Qtz + Pl Grt + Cpx + Amph + Ep + Ap + Zr	499–590	0.61–0.76	307–335 (Ar/Ar)	Marshall et al., 1997
Pv1	LB: Savona Massif	Eclogite	Grt + Omp + Zo + Ru + Ky + Qtz + Phe + Pl + Cpx + Ol?	650–750	> 1.7	374–392 (U/Pb)	Messiga et al., 1992; Giacomini et al., 2007; Maino
Pv2	GP: Gran Paradiso	Metapelite	Grt + St + Ilm + Qtz	600–650	0.5–0.7	Variscan (295–425)	Le Bayon et al., 2006
Pv3	GP: Orco valley	Metapelite	Bt + Chl + Pl + Grt + Qtz + Pg	610–630	0.8–0.9	Variscan (295–425)	Gasco et al., 2010
Pv4	MR: Monte Rosa	Metapelite	Bt + Chl + Grt + Pl + Ms + Qtz + Pg + St	550–575	0.4–0.6	Variscan (295–425)	Gasco et al., 2011a
Pv5	GS: Ambin nappe (Clarea complex)	Metapelite	Grt + Ms + Bt + Qtz + Ru + Ky + St	550–650	0.8–1.1	340–360 (Ar/Ar)	Monié, 1990; Borghi et al., 1999
Pv6	GS: Mont Mort	Metapelite	Grt + Bt + Sil/And	550–600	0.5–0.8	328–332 (U/Pb)	Bussy et al., 1996; Giorgis et al., 1999
Pv7	GS: Siviez-Mischabel	Metabasite	Hbl + Pl + Qtz	550–650	0.5–0.6	Variscan (295–425)	Thélin et al., 1993
Pv8	Ad: Central part	Metabasite	Grt + Omp + Ky + Ms + Amph + Qtz + Dol + Ru Qtz + Ms + Pl + Bt + Grt + Ru	675–825	1.95–2.45	346–402 (U/Pb)	Dale and Holland, 2003; Liati et al., 2009
Pv9	Ad: Northern part	Metabasite	Grt + Omp + Ky + Ru + Ms + Ep + Pl + Qtz Pl + Qtz + Grt + Ms + Amph + Ep + Bt	565–715	1.45–1.95	304–354 (U/Pb)	Dale and Holland, 2003; Liati et al., 2009
Pv10	Su: Suretta	Metabasite	Grt + Hbl + Ep + Qtz + Cpx	617–750	> 2.0	Variscan (295–425)	Nussbaum et al., 1998
Pv11	TW: Frosnitzal	Metabasite	Grt + Omp + Qtz	400–500	0.8–1.2	400–437 (U/Pb)	Zimmermann and Franz, 1989; von Quadt et al., 1997; von Quadt et al., 1997; Droop, 1983
Pv12	TW: Doesenertal	Metabasite	Grt + Omp + Qtz	520–720	> 1.2	400–437 (U/Pb)	Faryad et al., 2002; Melcher et al., 2002
Av1	SC: Hochgrossen Massif	Metabasite	Amph + Cpx + Ab + Zo	650–750	2.0–2.2	389–405 (Ar/Ar)	Müller and Thöni, 1995; Thöni, 2002; Konzett et al.
Av2	Oe: Central Oetzal Stubai	Metabasite	Grt + Omp	700–800	2.5–2.9	340/370 (Rb/Sr)	Rode et al., 2012
Av3	Oe: Oetzal Stubai	Metapelite	Grt + Qtz + Ky + Sil + St + Ms + Bt + Pl	550–650	1.1–1.3	350–360	Godard et al., 1996; Hauzenberger et al., 1996
Av4	TZ: Ultental	Metapelite	Grt + Bt + Pl + Kfs + Ky + Ms + Ru	650–750	1.0–2.0	365 (Pb/Pb)	Herzberg et al., 1977; Tumiati et al., 2003; Morten et al.
Av5	TZ: Ultental	Metabasite	Grt + Omp + Qtz	640–700	1.2–1.6	360 (Ar/Ar)	Schweinhage and Massonne, 1999
Av6	TZ: Ultental	Ultramafite	Grt-bearing ultramafics	770–810	2.2–2.8	326–334 (Sm/Nd)	Schweinhage and Massonne, 1999
Av7	Sil: Ischgl	Metabasite	Grt + Omp + Qtz + Ru + Phe	620–670	2.3–2.9	> 387	Schweinhage and Massonne, 1999
Av8	Sil: Val Puntota	Metabasite	Grt + Omp + Qtz + Ru + Phe	400–500	2.5–2.7	> 387	Gosso et al., 1995
Av9	LCN: Mortirolo	Metapelite	Dum + Qtz	750–850	> 2.0	Early Variscan (375–425)	Thöni, 1981; Zucali, 2001
Av10	LCN: Mortirolo	Metabasite	Di + Grt + Scp + Pl + Qtz	750–950	0.65–0.9	314–370	Zucali and Spalla, 2011;
Av11	DB: Valpelline	Metapelite	Bt + Qtz + Pl + Kfs + Grt + Zm + Mnz + Ry + Ap + Sil	661–745	0.45–0.65	< 320	Manzotti and Zucali, 2013; Gardien et al., 1994; Manzotti and Zucali, 2013
Av12	DB: Valpelline	Metabasite	Bt + Qtz + Pl + Kfs + Grt + Zm + Mnz + Ry + Ap + Sil	700–750	0.9–1.0	< 320	Boriani and Villa, 1997; Giobbi et al., 2003
Sv1	Strona Ceneri Zone	Metapelite	Hbl + Pl + Bt + Chl	590–690	0.6–0.8	307–359 (Ar/Ar)	Fumasoni, 1974; Mottana et al., 1985; di Paola and Spalla
Sv2	DCZ: Upper Como lake	Metapelite	Grt + Bt + Ms + Qtz + Pl + St + Ky	560–650	0.7–1.1	300–400 (K/Ar)	Mottana et al., 1985; Bertotti et al., 1993; Siletto et al., 1993
Sv3	Monte Muggio Zone	Metapelite	Grt + Bt + Ms + Ky + St	560–580	0.7–0.9	320–340 (K/Ar)	Diella et al., 1992; Zanoni et al., 2010
Sv4	VVB: Dervio Olgiasca	Metapelite	Grt + Bt + Ms + Pl + Qtz + Ky + St	550–630	0.7–0.9	320–340	Zanoni et al., 2010
Sv5	Val Vedello	Metapelite	Bt + Grt + St	590–668	0.7–1.1	320–340	Zanoni et al., 2010
Sv6	Val Vedello	Metapelite	Grt + Chl	470–550	0.35–0.75	< 320	Zanoni et al., 2010
Sv7	Valtellina NEOB Type A	Metapelite	Grt + St + Bt + Ms + Plg + Qtz + Cld	570–660	0.85–1.15	320–340	Spalla et al., 1999
Sv8	Valtellina NEOB Type B	Metapelite	Qtz + Ms + Chl + Ab + Grt + Bt	440–550	0.35–0.75	320–340	Spalla and Gosso, 1999; Zanoni et al., 2010
Sv9	Val Camonica NEOB Type A	Metapelite	Grt + St + Bt + Ms + Pl + Qtz + Cld	550–630	0.8–1.1	320–340	Spalla et al., 2006
Sv10	TVB: Val Trompia	Metapelite	Grt + Cld + Bt + Ms + Pl + Qtz	500–550	0.9–1.3	349–379 (Rb/Sr)	Giobbi and Gregnani, 1983; Riklin, 1983; Spalla et al.
Sv11	Ei: Eisecktal	Paragneiss	Crd + Sil + Bt	600–650	0.2–0.3	Devonian (350–420)	Benciolini et al., 2006
Sv12	Ei: Eisecktal	Metapelite	Qtz + Chl + Grt + Bt + Kfs + Ol	450–550	0.5–0.65	Devonian (350–420)	Benciolini et al., 2006

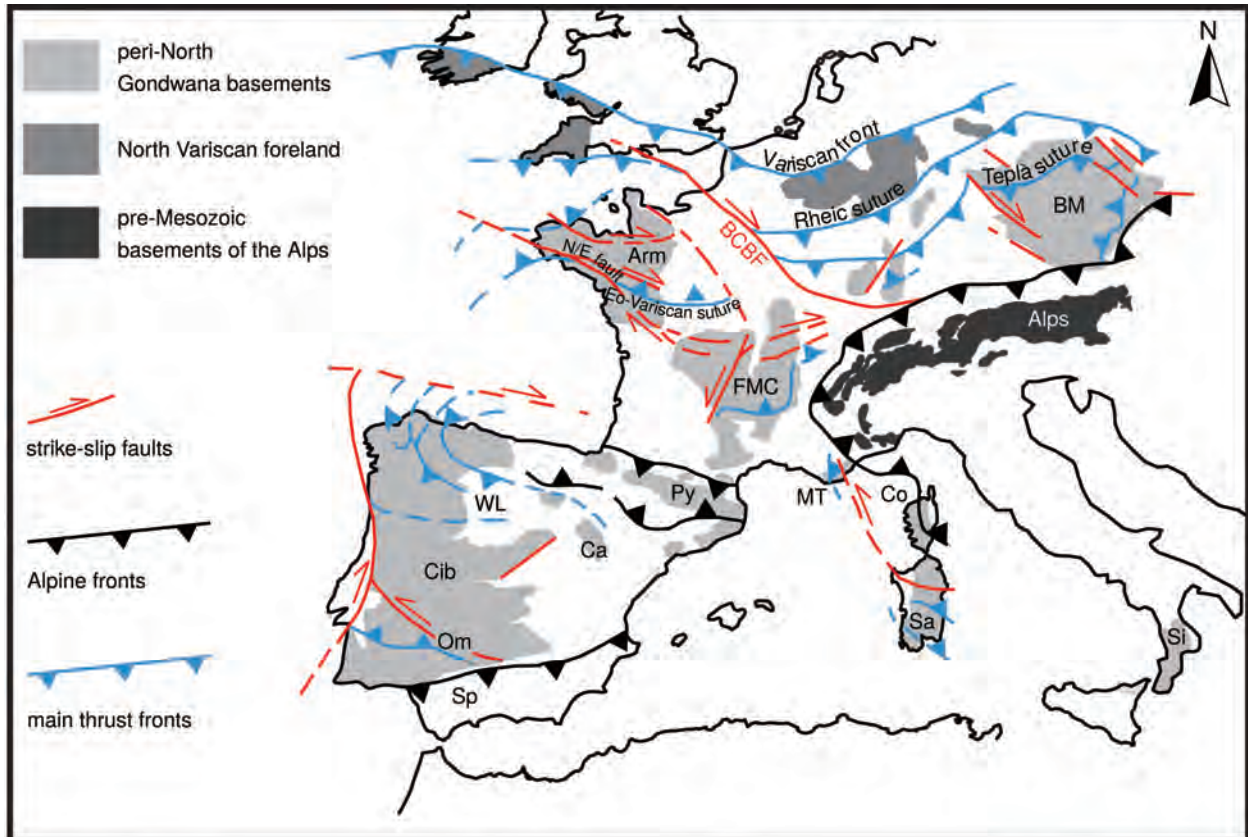
Key	Location	Lithology	Paragenesis	T (°C)	P (GPa)	Age (Ma)	References
HA1	Haut Allier	Eclogite (UGU)	Grt + Omp + Ky + Qtz + Ru + Zo	750–850	1.8–2.2	Middle to lower Devonian (380–416)	Ducrot et al., 1983; Ledru et al., 1989; Faure et al., 2005; Faure et al., 2008; Lardeaux, 2014; Paquette et al., 2017; Lotout et al., 2018
Ma1	Marvejols	Eclogite (UGU)	Grt + Omp + Ky + Qtz + Ru + Zo	800–850	1.8–2.0	Middle to lower Devonian (380–416)	Pin and Lancelot, 1982; Ledru et al., 1989; Mercier et al., 1991a; Faure et al., 2005; Faure et al., 2008; Lardeaux, 2014; Paquette et al., 2017; Lotout et al., 2018
Li1	Limousin	Migmatite (LGU)	Qtz + Pl + Kfs + Grt + Ky/Sil	600–700	0.8–1.1	370–385 (U/Th/Pb)	Faure et al., 2008; Faure et al., 2009
Li2	Limousin	Metapelite (UGU)	Ky + Bt + Ms + Pl + Grt	830	1.6–1.9	390–430	Bellot and Roig, 2007
Li3	Limousin	Migmatite (LGU)	Kfs + Sil + Grt + Pl + Qtz	760–780	0.5–0.6	349–359 (U/Th/Pb)	Gébelin et al., 2004, 2009
Li4	Limousin	Eclogite (LGU)	Zo + Grt + Omp + Ky + Ru	580–730	2.5–3.5	406–418 (U/Pb)	Berger et al., 2010
Li5	Limousin	Migmatite (UGU)	Qtz + Pl + Kfs + Grt + Ky/Sil	650–750	0.7–0.8	377–387 (U/Pb)	Lafon, 1986; Faure et al., 2005, 2008
LB1	La Bessenois	Eclogite (UGU)	Grt + Qtz + Ru + Zo + Ap	600–710	1.6–1.9	401–415 (Sm/Nd)	Paquette et al., 1995; Faure et al., 2008; Lardeaux, 2014; Paquette et al., 2017
ML1	Mont du Lyonnais	Peridotite (UGU)	Spi-bearing lherzolite	880–950	< 2.0	Variscan (295–425)	Gardien et al., 1988
ML2	Mont du Lyonnais	Eclogite (UGU)	Grt + Omp + Qtz + Zo + Ky + Ph + Ru	730–780	1.5	Middle to lower Devonian (380–416)	Dufour et al., 1985; Feybesse et al., 1988; Lardeaux et al., 1989, 2001; Mercier et al., 1991a
ML3	Mont du Lyonnais	Metapelite (UGU)	Qtz + Pl + Kfs + Grt + Ky/Sil + Bt	600–750	0.6–1.0	350–360 (Ar/Ar)	Lardeaux and Dufour, 1987; Costa et al., 1993; Faure et al., 2005, 2008, 2009
ML4	Mont du Lyonnais	Migmatite (UGU)	Qtz + Pl + Kfs + Sil + Bt	650–750	0.7–1.2	368–400 (Rb/Sr)	Dufour, 1982; Duthou et al., 1994
Ro1	Lévézou	Eclogite (UGU)	Grt + Omp + Ky + Qtz + Ru + Zo	680–800	2.1–2.3	344–370	Burg et al., 1989; Mercier et al., 1991a; Lotout, 2017
Ro2	Najac	Eclogite (UGU)	Grt + Omp + Ky + Qtz + Zo	560–630	1.5–2.0	376–385	Burg et al., 1989; Mercier et al., 1991a; Lotout et al., 2018
Ro3	Le Vibal	Eclogite (UGU)	Grt + Ky + Qtz + Omp	740–860	1.0–1.4	Variscan (295–425)	Burg et al., 1989;
Ar1	Artense	Eclogite (UGU)	Grt + Cpx + Qtz + Ru + Zo	700–750	1.4–1.6	Variscan (295–425)	Mercier et al., 1989, 1991a
Ar2	Artense	Paragneiss (LGU)	Qtz + Pl + Bt + Sil + Grt	670–750	0.6–0.82	Variscan (295–425)	Mercier et al., 1992
PA1	Plateau d'Aigurande	Metapelite (UGU)	Grt + Ky + Qtz	650–750	1.0–1.2	376–397 (Ar/Ar)	Faure et al., 1990, 2008; Boutin and Montigny, 1993
PA2	Plateau d'Aigurande	Micaschist (PAU)	Ms + Chl + Grt + Qtz	550–650	0.6–0.8	350–380 (Ar/Ar)	Faure et al., 1990
Mc1	Maclas	Eclogite (UGU)	Grt + Cpx + Qtz + Ru + Zo	700–770	1.4–1.6	Variscan (295–425)	Gardien and Lardeaux, 1991; Ledru et al., 2001
VD1	Velay Dome	Migmatite (LGU)	Kfs + Bt + Sil ± Co	675–725	0.4–0.5	309–319 (U/Pb)	Ledru et al., 2001; Barbey et al., 2015

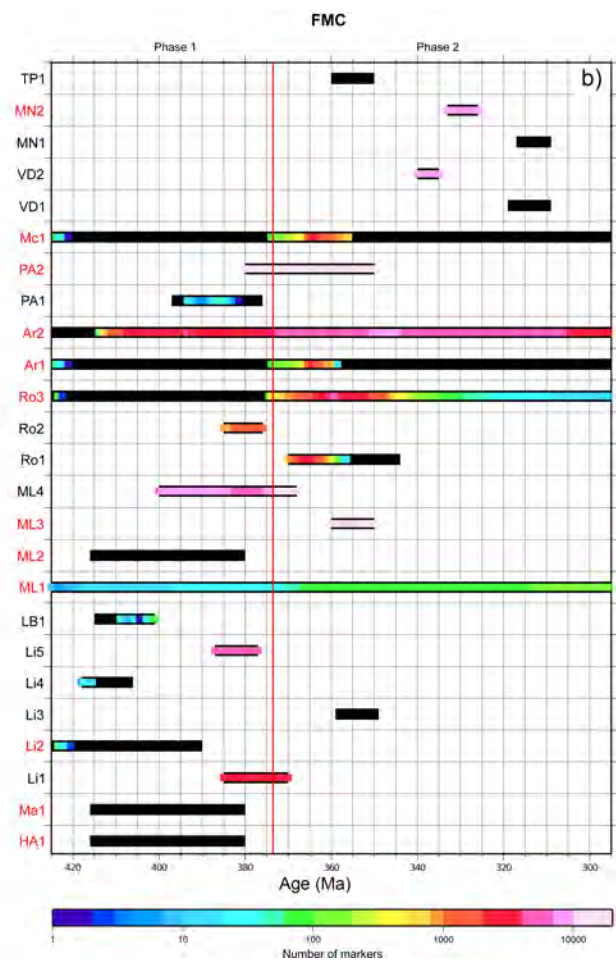
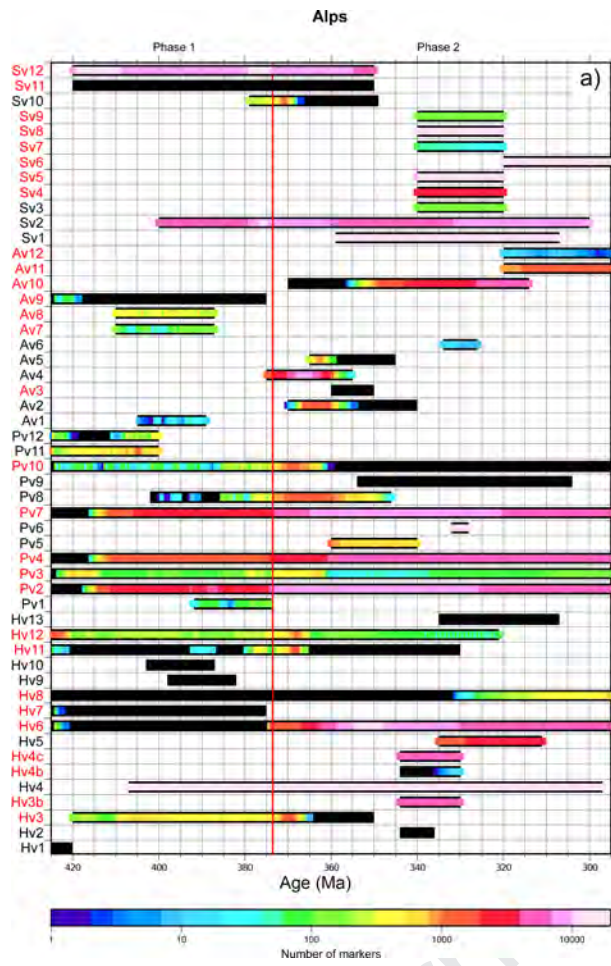
VD2	Velay Dome (Cévennes)	Micaschist (PAU)	Ms + Chl + Grt + Qtz	475–525	FMC 0.4–0.6	335–340 (Ar/Ar)	Ledru et al., 2001
MN1	Montagne Noire	Eclogite (MN)	Grt + Omp + Rt + Qtz	700–800	2.1	309–317 (U/Th/Pb)	Demange, 1985; Faure et al., 2014; Whitney et al., 2015
MN2	Montagne Noire	Metabasite (MN)	Spi-bearing ultramafite	800–900	0.5–1.0	326–333	Demange, 1985
TP1	Quercy	Metapelite (TPU)	Qtz + Pl + Ms + Bt + Grt + Rt + Ap + Mo	400–500	0.4–0.6	350–360 (Ar/Ar)	Duguet et al., 2007; Faure et al., 2009

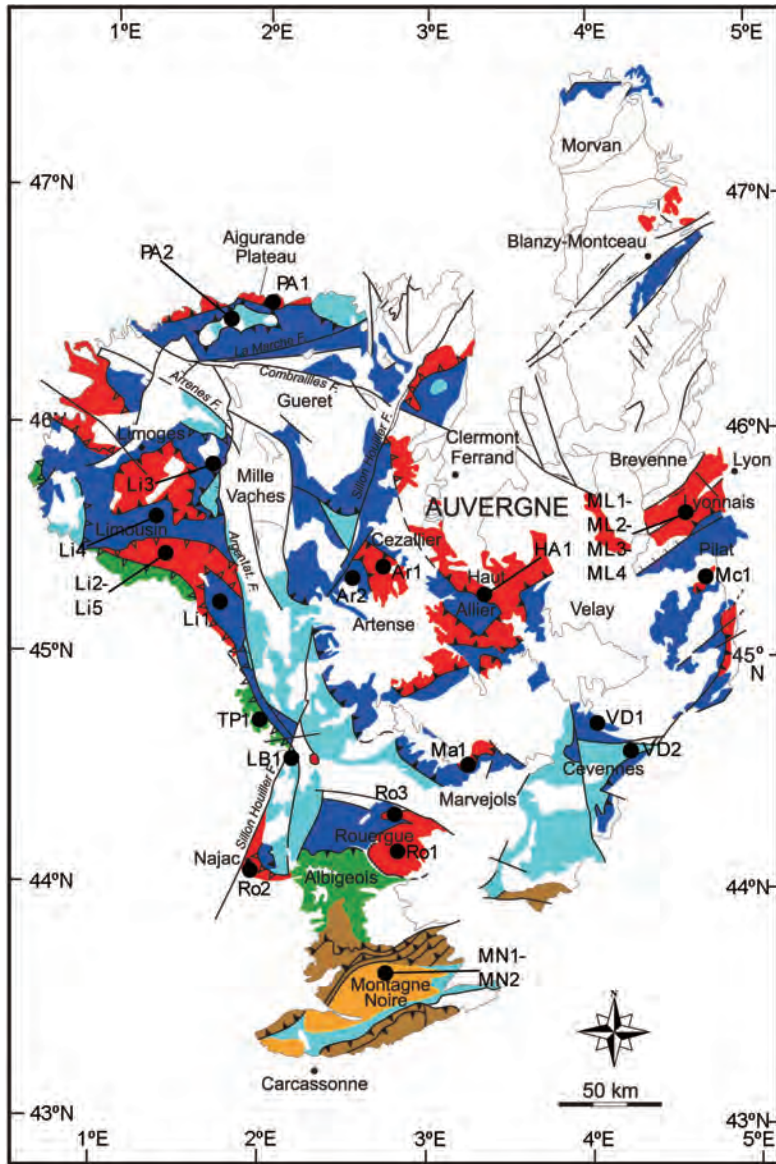
Journal Pre-proof

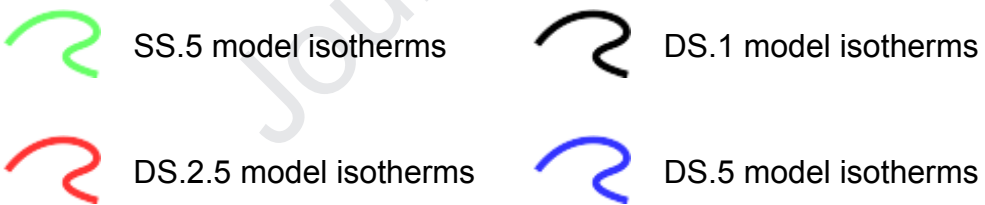
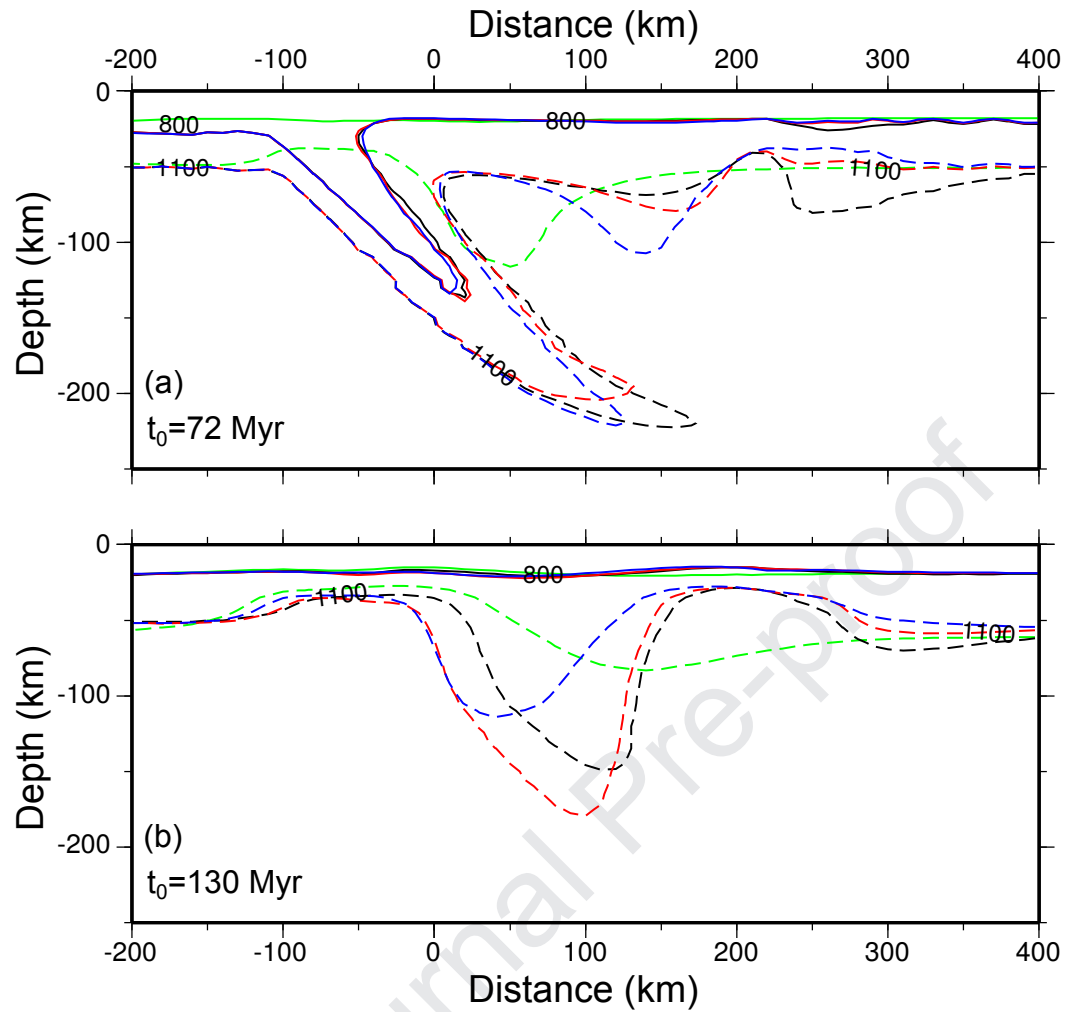
	Rheology	E (kJ/mol)	n	μ_0 (Pa·s)	ρ_0 (kg/m ³)	K (W/(m·K))	H _c (μW/m ³)	References
Continental Crust	Dry Granite	123	3.2	3.47×10^{21}	2640	3.03	2.5	Ranalli and Murphy, 1987; Haenel et al., 1988; Dubois and Diament, 1997; Best and Christiansen, 2001
Upper Oceanic Crust	-	-	-	10^{19}	2961	2.10	0.4	Dubois and Diament, 1997; Best and Christiansen, 2001; Gerya and Yuen, 2003; Afonso and Ranalli, 2004; Gerya and Stockhert, 2006; Roda et al., 2012; Kirby, 1983; Ranalli and Murphy, 1987; Dubois and Diament, 1997; Best and Christiansen, 2001; Afonso and Ranalli, 2004
Lower Oceanic Crust	Diabase	260	2.4	1.61×10^{22}	2961	2.10	0.4	Chopra and Peterson, 1981; Kirby, 1983; Haenel et al., 1988; Dubois and Diament, 1997; Best and Christiansen, 2001; Roda et al., 2012
Mantle	Dry Dunite	444	3.41	5.01×10^{20}	3200	4.15	0.002	Haenel et al., 1988; Dubois and Diament, 1997; Schmidt and Poli, 1998; Best and Christiansen, 2001; Roda et al., 2011; Gerya and Stockhert, 2006
Serpentine	-	-	-	10^{19}	3000	4.15	0.002	

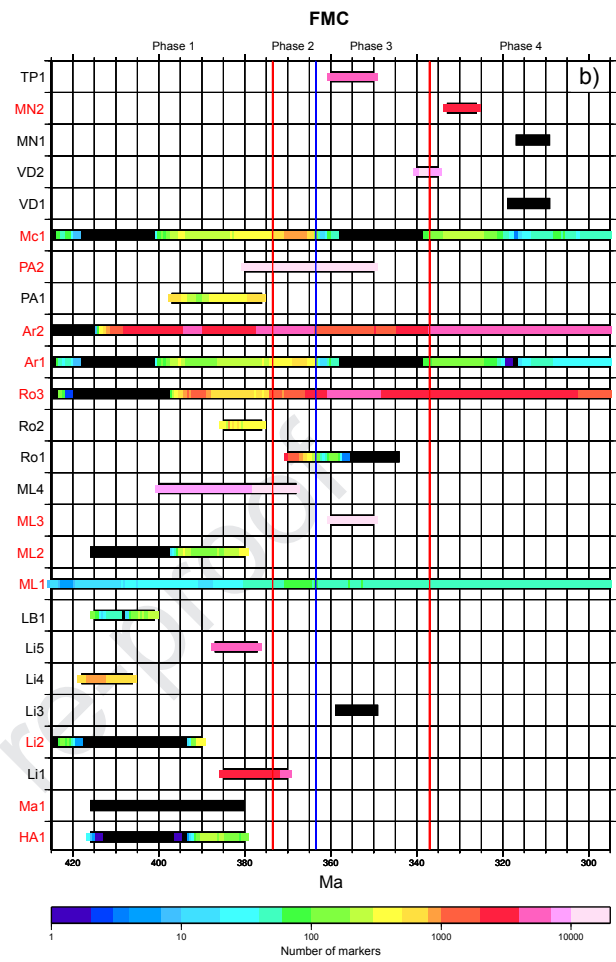
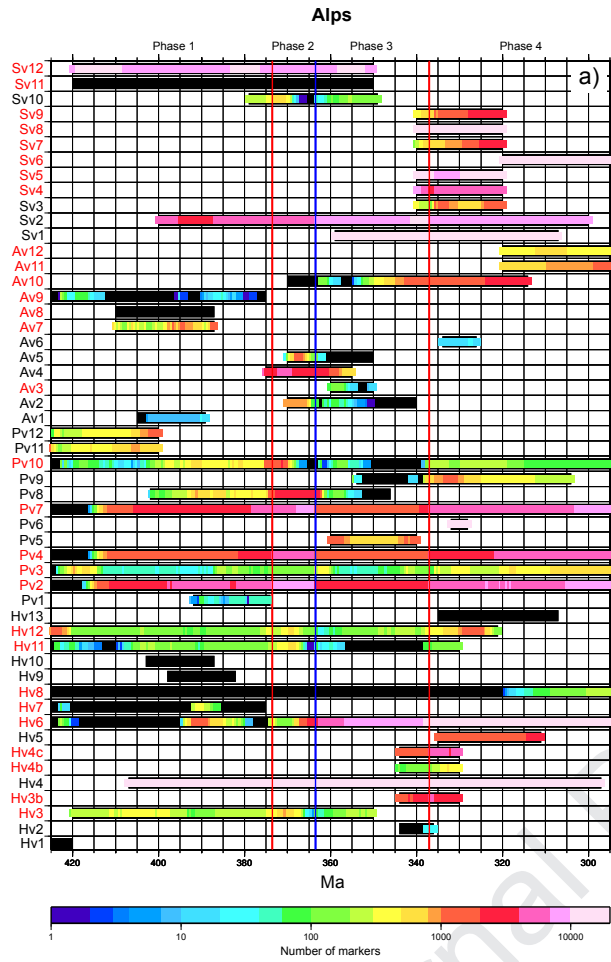
Journal Pre-proof

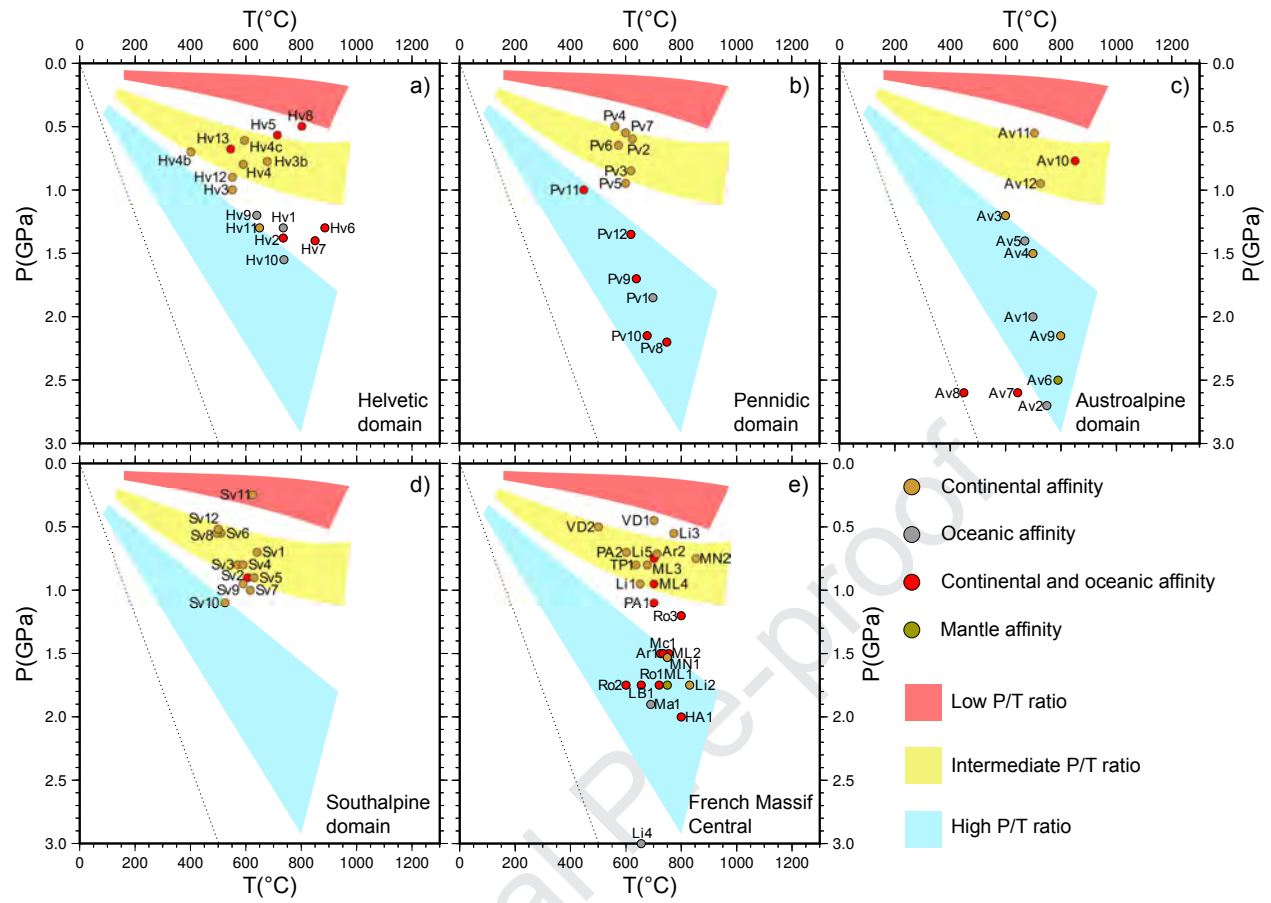


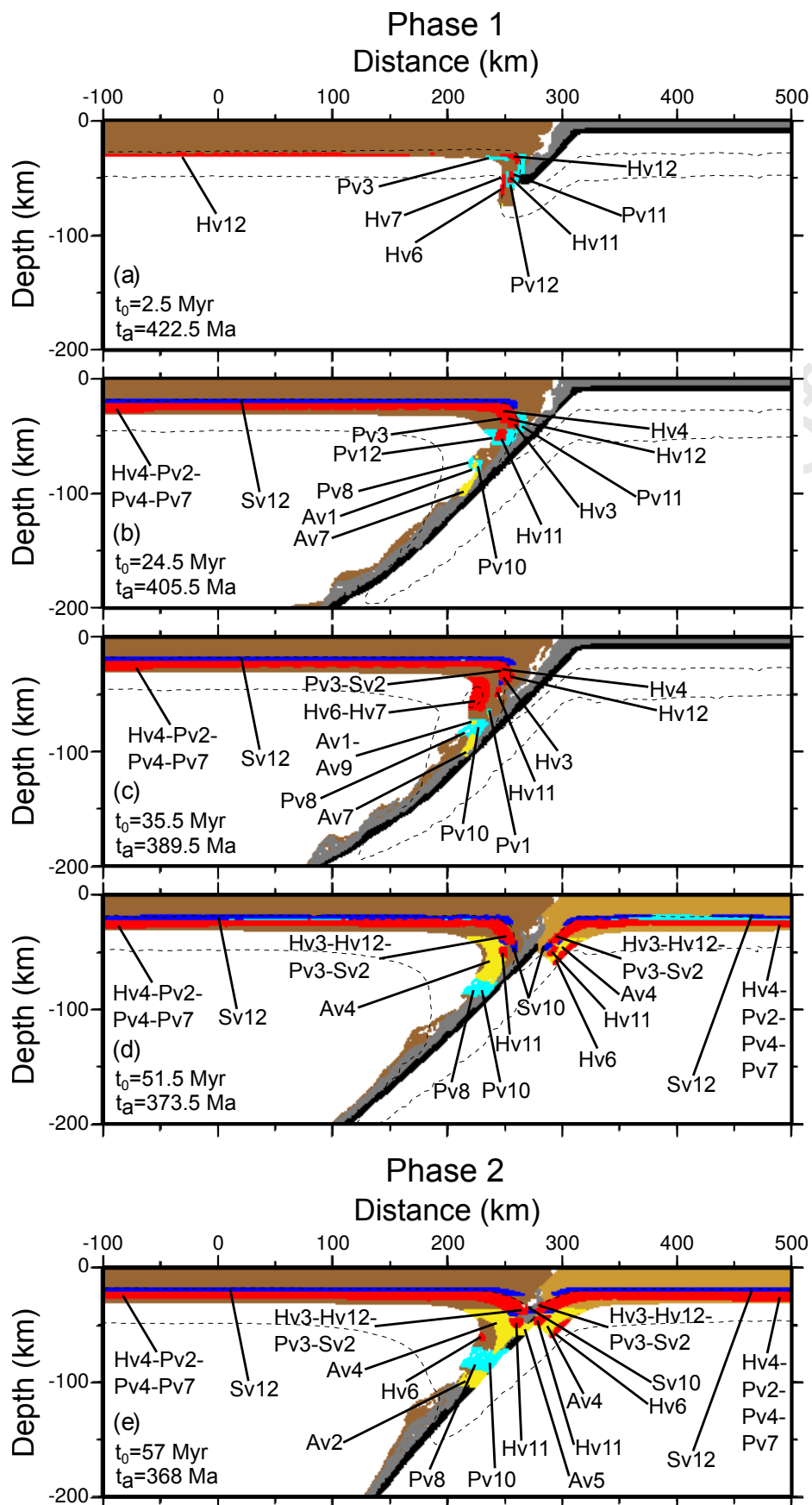


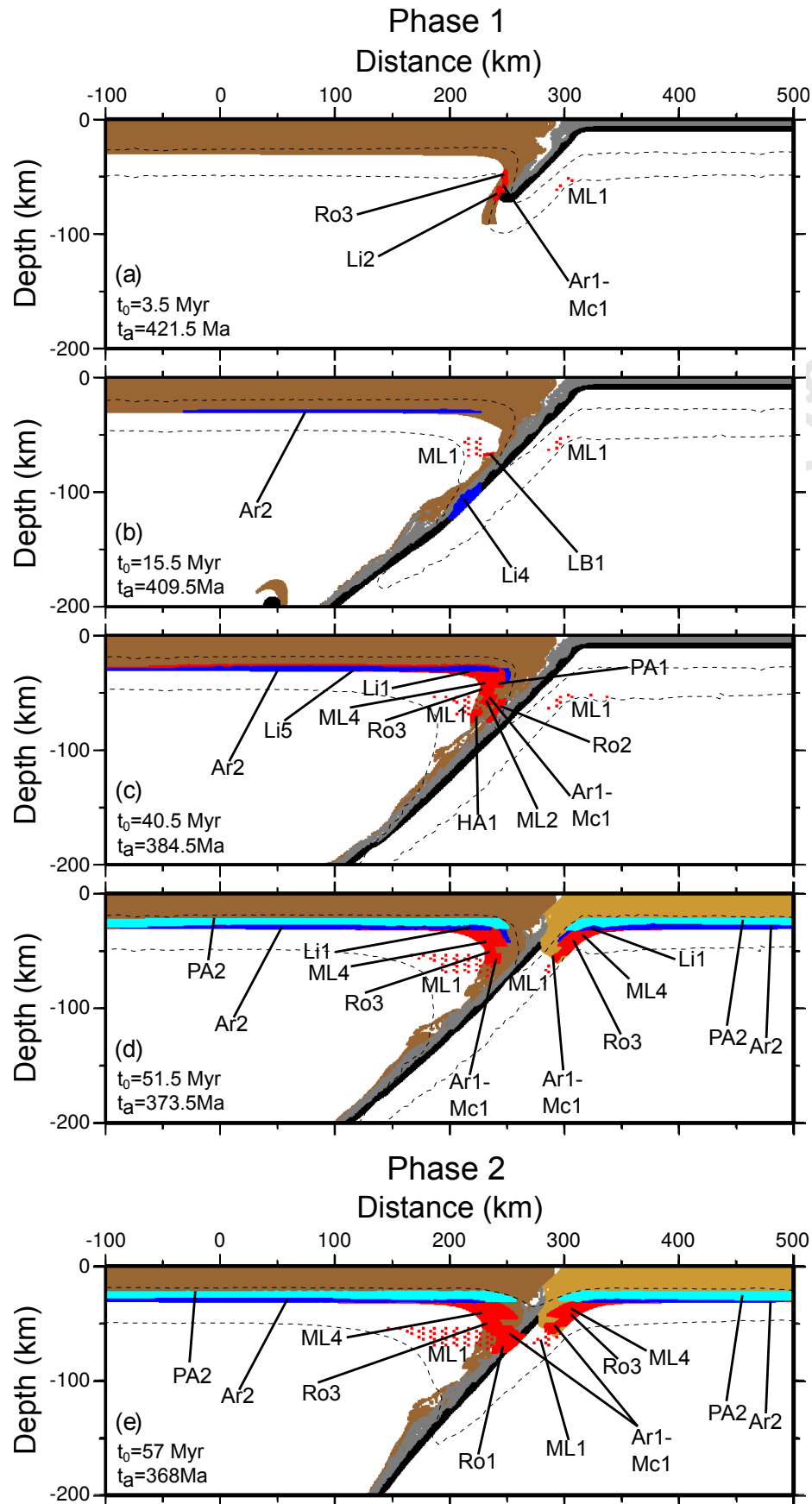


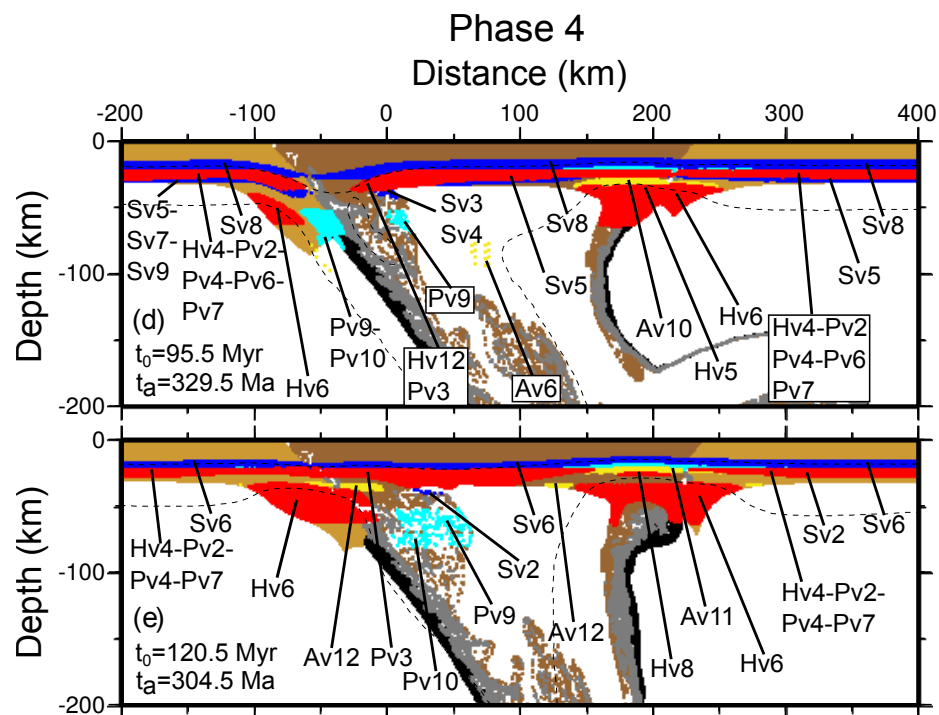
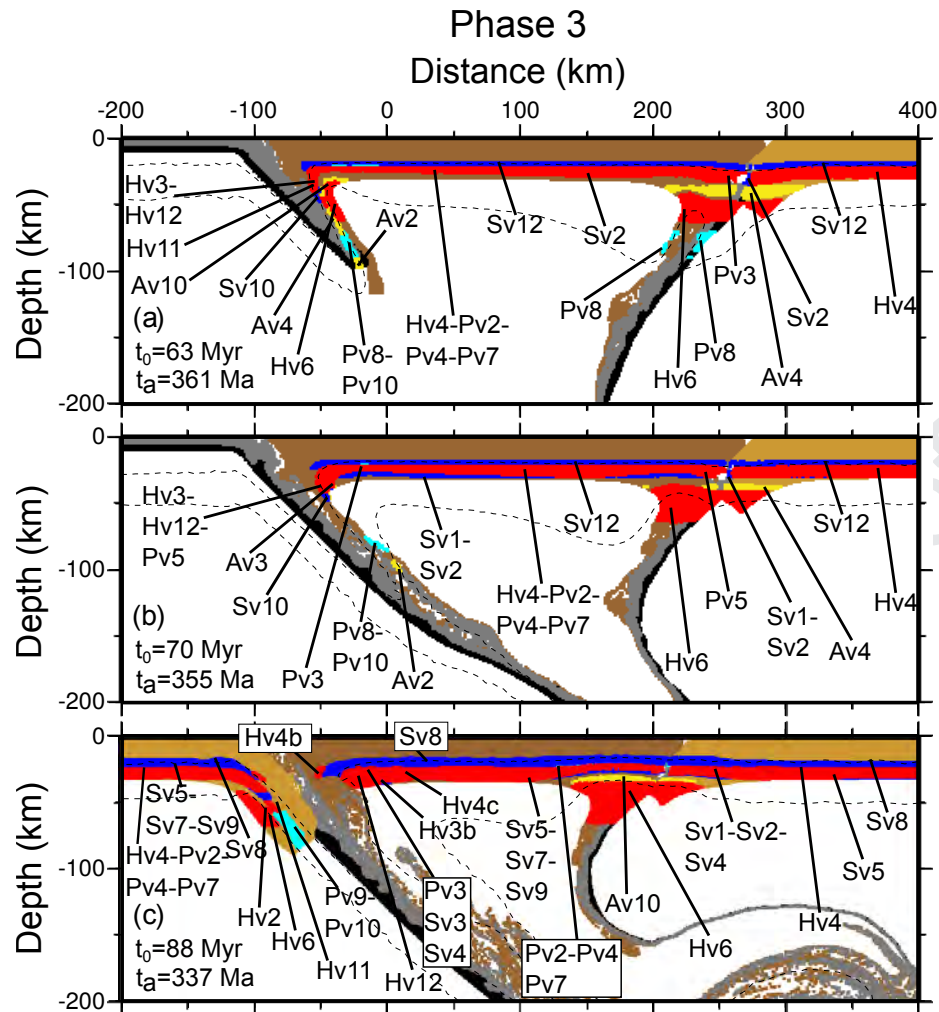


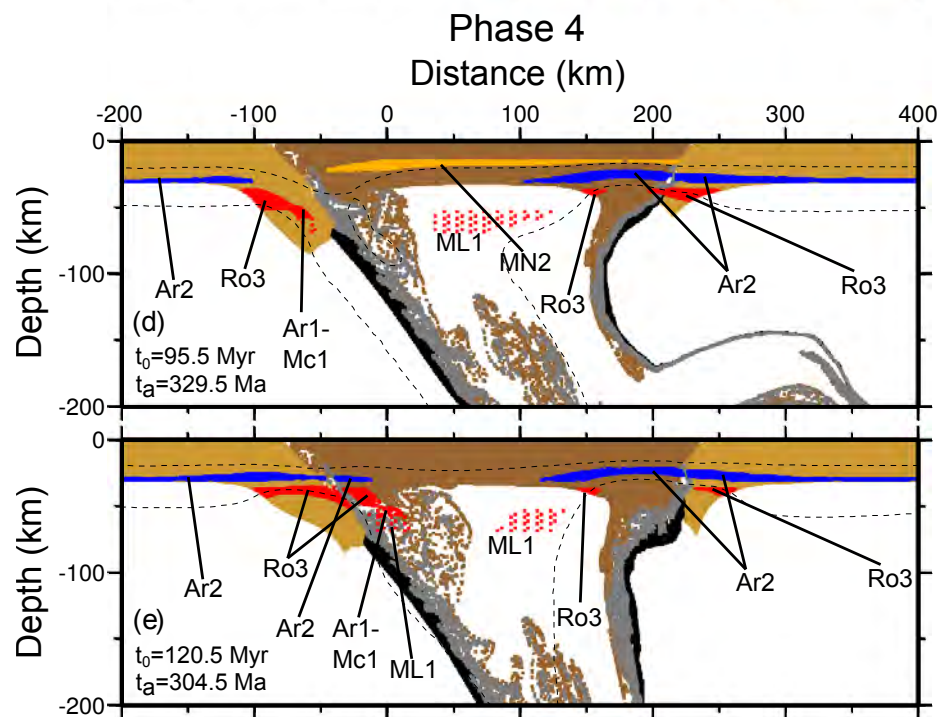
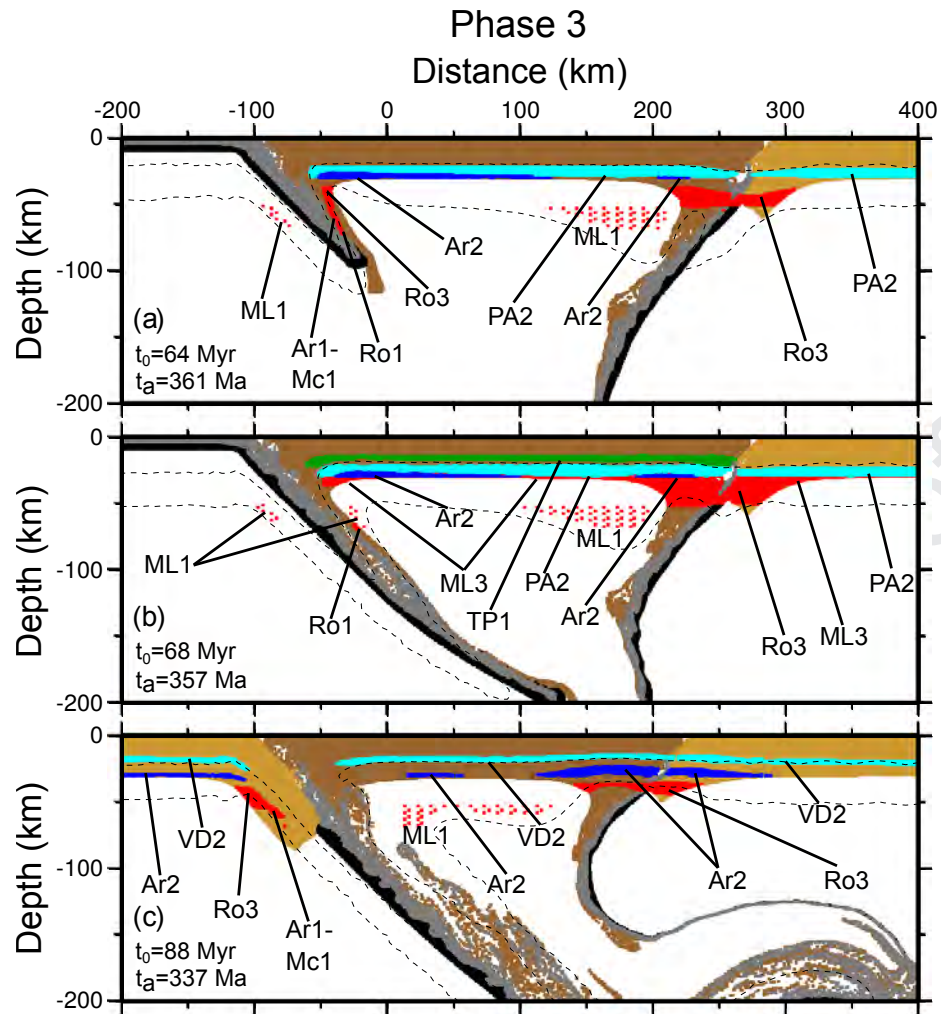


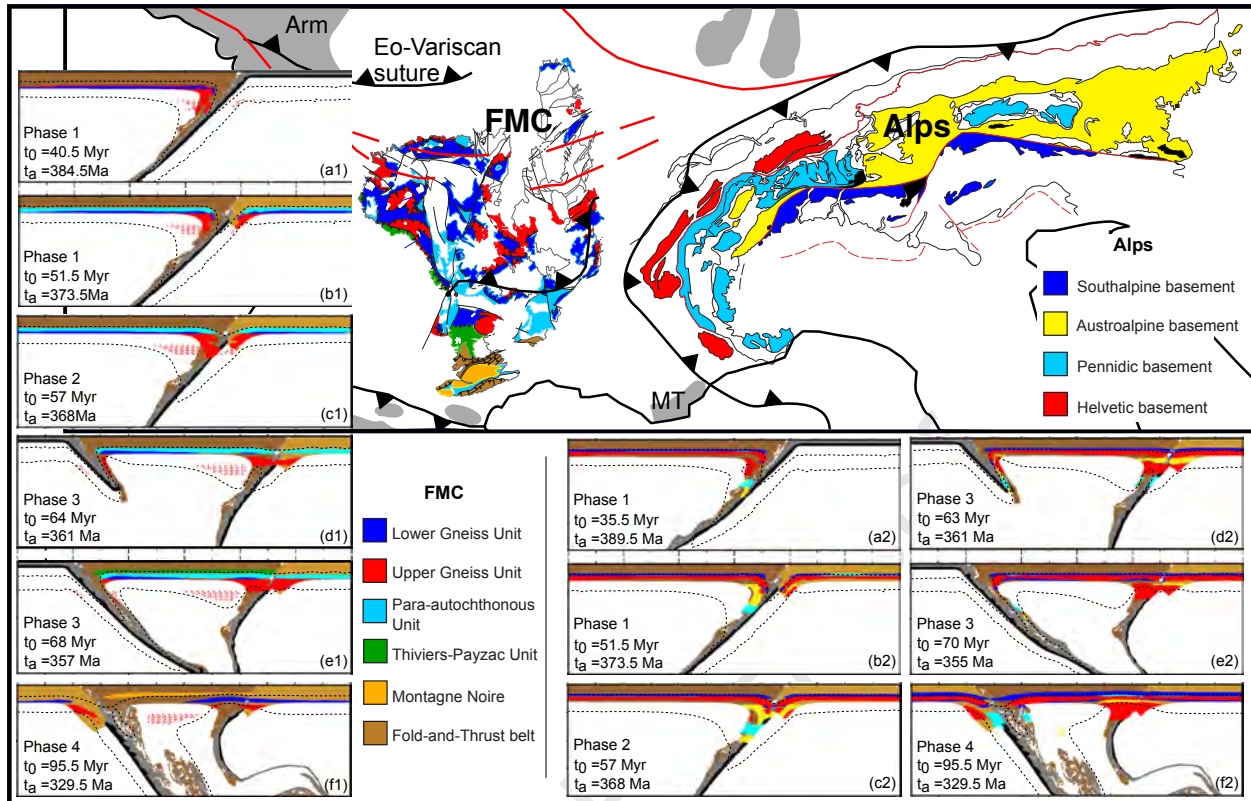


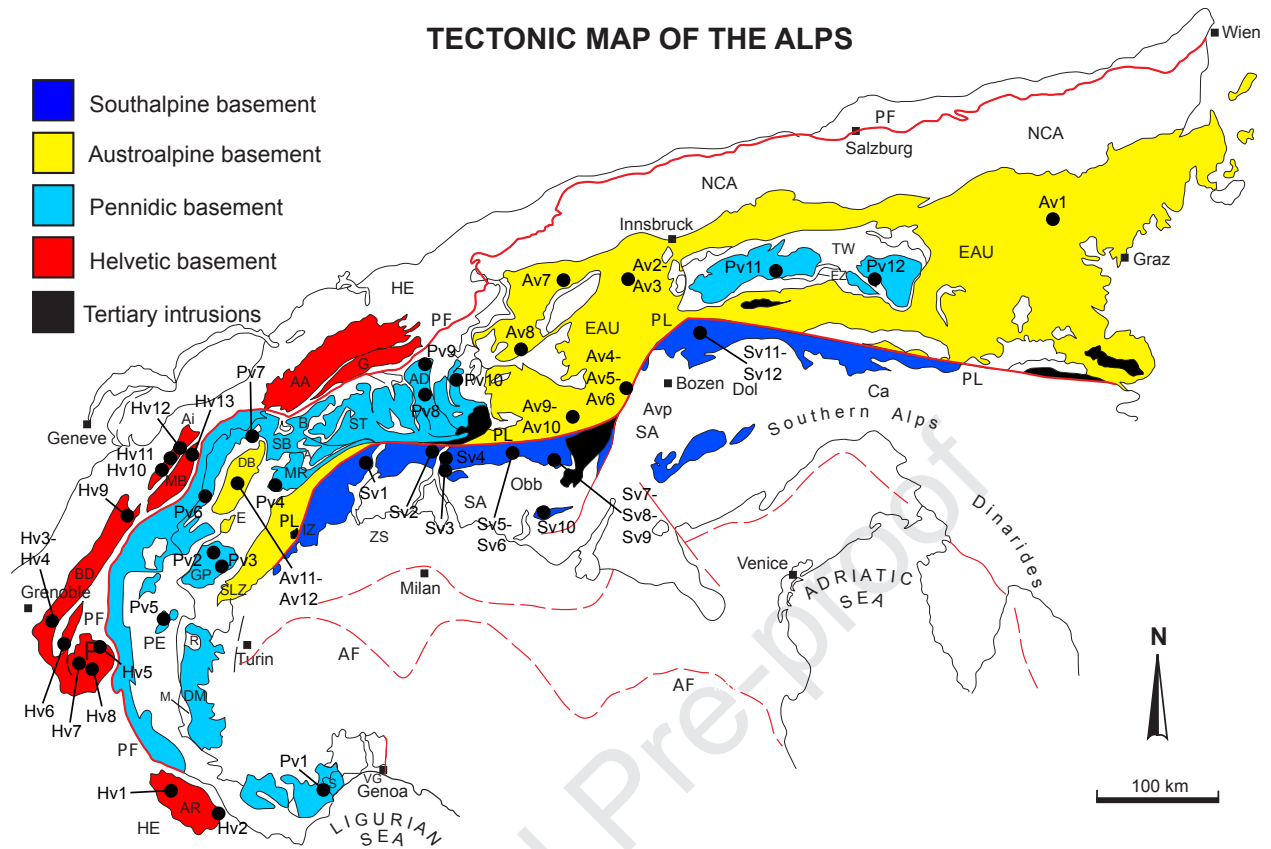


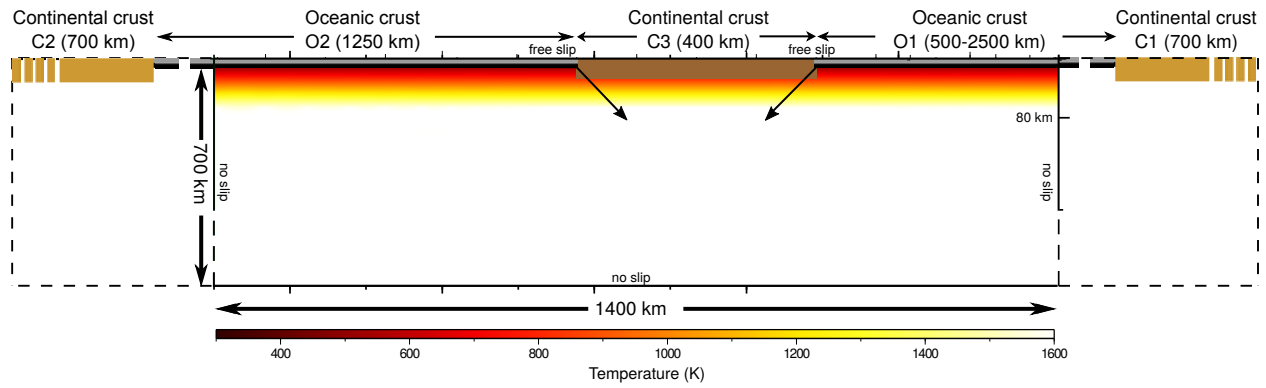






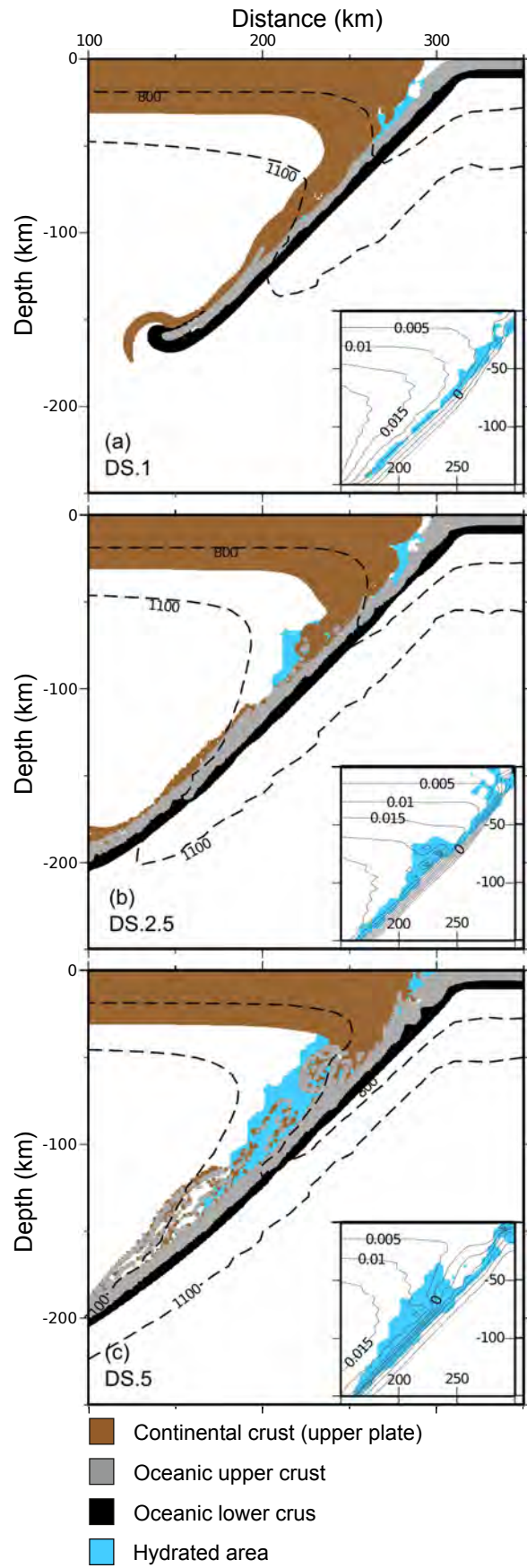


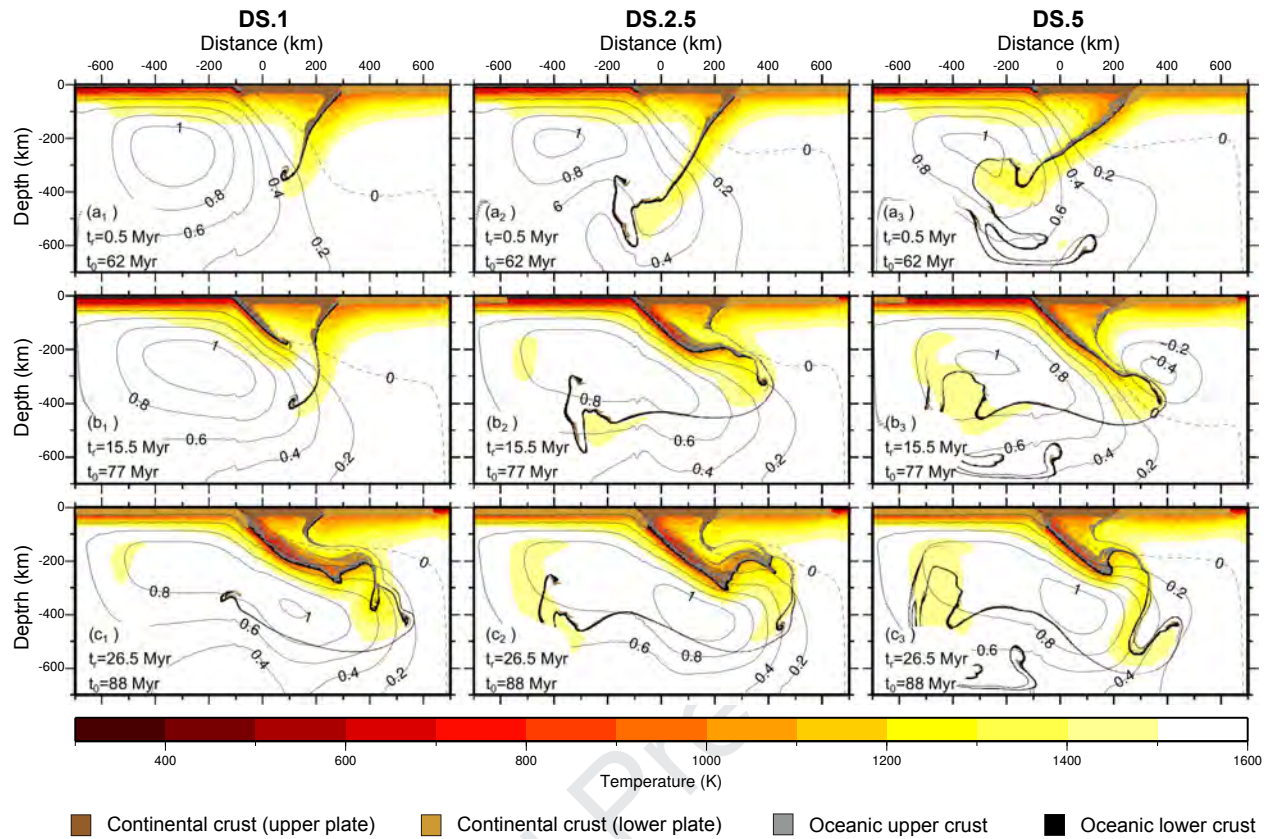


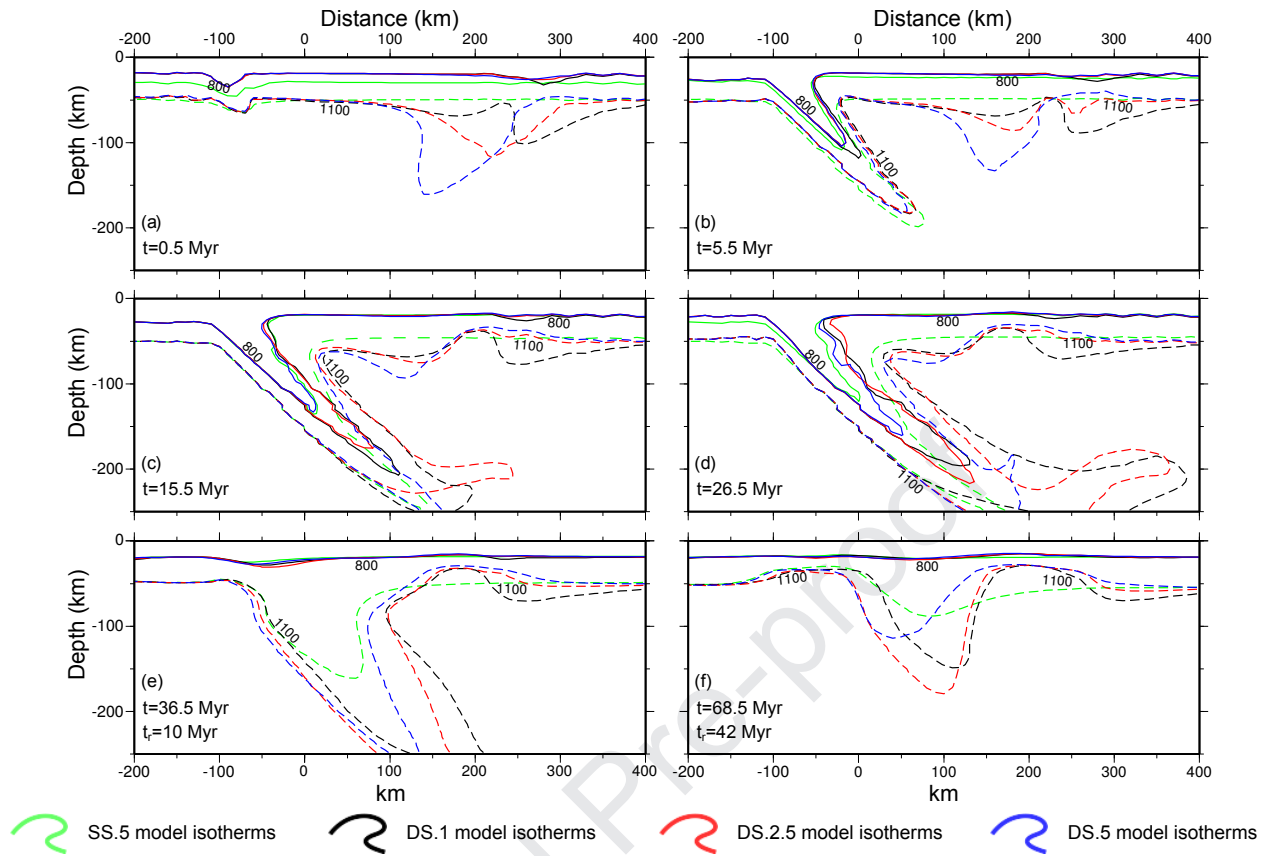


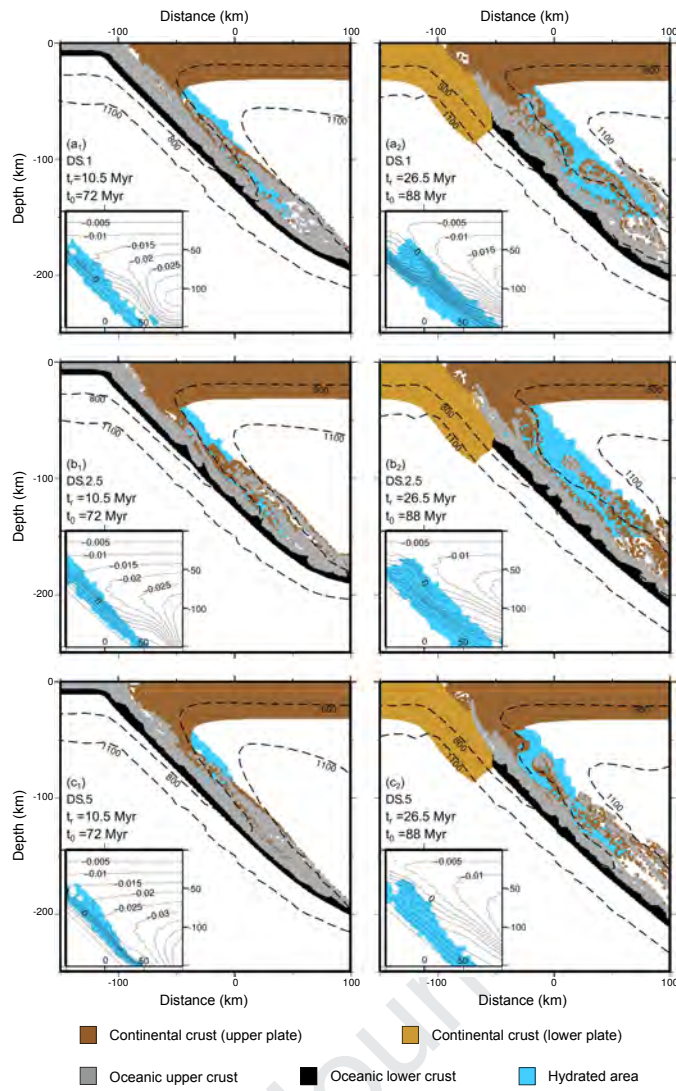
Continental crust (UP)
 Continental crust (LP)
 Oceanic upper crust
 Oceanic lower crust

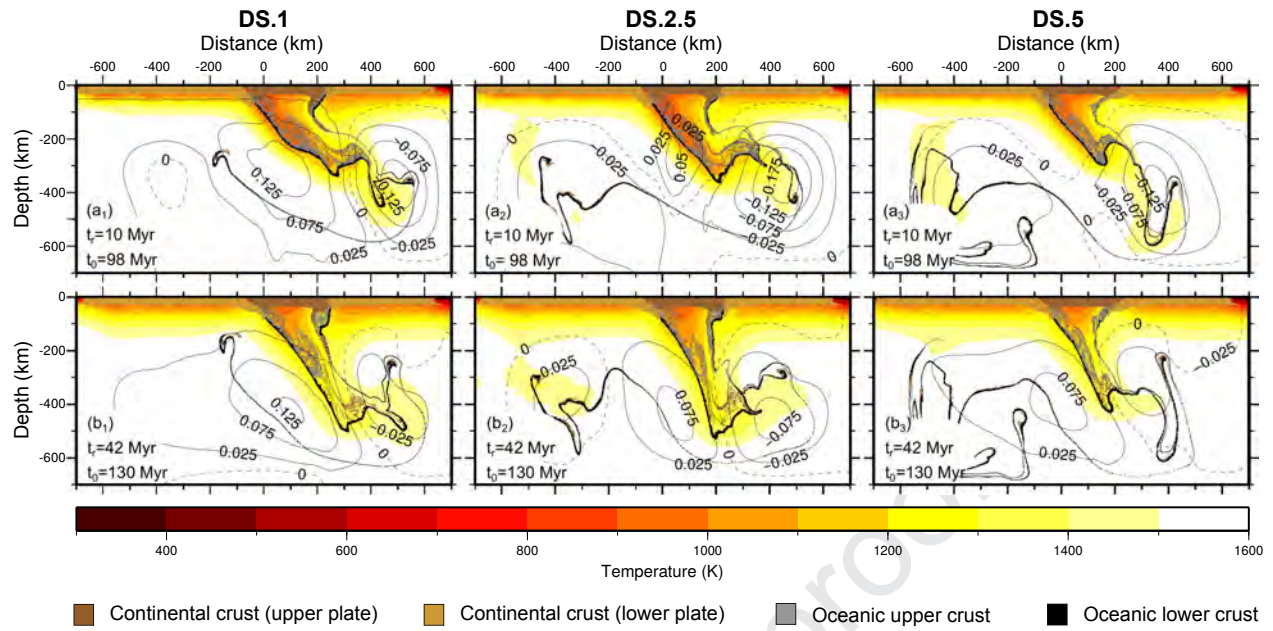
Model	DS.1	DS.2.5	DS.5	SS.5
Velocity - phase 1 (cm/yr)	1	2.5	5	5
Dimension of the ocean - phase 1 (km)	500	1250	2500	2500
Velocity - phase 3 (cm/yr)	5	5	5	-
Dimension of the ocean - phase 3 (km)	1250	1250	1250	-











- In a double subduction complex, the second subduction is colder than the first
- Data from the Alps with high P/T ratios fit well with both hot and cold subductions
- Data from the French Massif Central have a better compatibility with hot subductions
- Polycyclic models better fit with Variscan data from the Alps
- Rocks from Upper Gneiss Unit could derive from the ablative erosion of the upper plate